Paper-based Microfluidics for Electrochemical Applications

Dissertation

Liuliu Shen

Department of Chemistry

TECHNISCHE
UNIVERSITÄT
DARMSTADT

Paper-based Microfluidics for Electrochemical Applications

vom Fachbereich Chemie
der Technischen Universität Darmstadt

zur Erlangung des Grades

Doctor rerum naturalium
(Dr. rer. nat.)

Dissertation

von Liuliu Shen
aus Shijiazhuang, Hebei, China

Erstgutachter: Prof. Dr.-Ing. Bastian J. M. Etzold

Zweitgutachter: Prof. Dr. Markus Biesalski

Darmstadt 2020

Tag der Einreichung: 28. November 2019

Tag der mündlichen Prüfung: 03. Februar 2020

Liuliu Shen: Paper-based Microfluidics for Electrochemical Applications
Darmstadt, Technische Universität Darmstadt
Year thesis published in TUprints 2020
URN: urn:nbn:de:tuda-tuprints-117737
Date of the viva voce 03.02.2020

Declaration

M.Sc. Liuliu Shen
Alarich-Weiss-Straße 8
64287 Darmstadt

This work described in this thesis was carried out at the Department of Chemistry, Technische Universität Darmstadt from December 2015 to August 2019. This thesis represents the author's original work, except where otherwise stated, and no part of it has been submitted for a degree at any other university. Prior to the submission of this thesis, some work has been published as described in the relevant chapters herein.

Eidesstattliche Erklärung

Hiermit erkläre ich an Eides statt, dass ich die vorliegende Dissertation selbstständig und nur mit den angegebenen Hilfsmitteln angefertigt habe. Von mir wurde weder an der Technischen Universität Darmstadt noch einer anderen Hochschule ein Promotionsversuch unternommen.

Darmstadt, den 31. August 2019

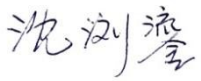

Liuliu Shen

The presented cumulative dissertation summarizes the essential scientific findings, which were reported to the scientific community in the following peer-reviewed journals. Chapters 2, 4, 5 and 6 are based on the following four publications:

[1] Liu-Liu Shen, Gui-Rong Zhang, Bastian J. M. Etzold. Paper-based microfluidics for electrochemical applications. *ChemElectroChem* DOI: 10.1002/celc.201901495.

[2] Liu-Liu Shen, Gui-Rong Zhang, Wei Li, Markus. Biesalski, Bastian J. M. Etzold. Modifier-free microfluidic electrochemical sensor for heavy-metal detection. *ACS Omega* 2 (2017) 4593-4603.

[3] Liu-Liu Shen, Gui-Rong Zhang, Tizian Venter, Markus. Biesalski, Bastian J. M. Etzold. Towards best practices for improving paper-based microfluidic fuel cells. *Electrochimica Acta* 298 (2019) 389-399.

[4] Liu-Liu Shen, Gui-Rong Zhang, Markus. Biesalski, Bastian J. M. Etzold. Paper-based microfluidic aluminum-air batteries: toward next-generation miniaturized power supply. *Lab on a Chip* 19 (2019) 3438-3447.

Abstract

Paper-based microfluidic platforms enable miniaturization and integration of various reaction processes and technologies into on-chip devices, aiming at fabricating a broad range of low cost custom products of our daily life. This dissertation focuses on applying the paper-based microfluidic concept to construct portable and disposable electrochemical devices with simple structure and affordable price. For three examples, their structural features, working principles and electrochemical performance are systematically investigated and discussed. The examples are:

- a paper-based microfluidic electrochemical sensor for detection of heavy metal ions,
- a paper-based microfluidic formate fuel cell,
- a paper-based microfluidic high-performing aluminum-air battery.

The microfluidic electrochemical sensor is based on a microfluidic paper channel combined with a three-dimensional (3D) configuration, and the three electrodes are all pristine graphite foil without any modifier or catalyst. This low-cost, simple and portable sensor exhibits a high sensitivity toward trace detection of heavy metal ions in aqueous solution with detection limits down to 1.2 µg/L for Cd^{2+} and 1.8 µg/L for Pb^{2+}. Detections of Cd^{2+} and Pb^{2+} in more sophisticated environments (e.g., mineral water or solution containing interfering ions) are also carried. The 3D configuration is found to be the key factor for achieving high detection performance. The paper-based microfluidic sensor is highly robust and the measurements on a single device result to be highly reproducible.

The paper-based microfluidic formate fuel cell is designed as a single-use and environmentally friendly power source for portable and disposable electronics, such as sensing devices. The key structural parameters that impact the overall performance of the fuel cell were systematically studied, including the fuel crossover, cell resistance, concentration of the redox reactants, catalyst loading, and the microfluidic paper channel properties. After optimization, an open circuit voltage of 0.86 V and a maximum power density of 7.1 mW/cm^2 can be achieved on a single cell. By correlating the cell performance with the electrolyte flow rate within different paper channels, for the first time it is unraveled that the textual properties of the paper largely influence the cell performance through mass transfer and depletion effect.

To achieve a higher energy and power density on miniaturized power device, paper-based microfluidic concept is further introduced to fabricate high-performing aluminum-air batteries. The unique microfluidic configuration reduces or even eliminates the major drawbacks of conventional aluminum-air batteries including battery self-discharge, product-induced electrode passivation, expensive air electrode and auxiliary fluid control system. The paper-based microfluidic Al-air battery exhibits impressive electrochemical performance in specific capacity (2750 Ah/kg) and energy density (2900 Wh/kg), both of which are superior among the reported miniaturized power sources. The paper-based microfluidic Al-air battery can be assembled into a user-friendly pouch cell configuration by simple lamination process, showing great potential toward real application.

This dissertation shows that paper-based microfluidics is an attractive concept to build low-cost, green, portable and user-friendly electrochemical devices with various functionalities. Aside from designing and fabricating high-performing paper-based microfluidic electrochemical devices, systematical investigations are also made to understand how the device structure (e.g., electrode modification and arrangement) and microfluidic flow behavior (e.g., flow rate and diffusion rate) influence the overall performance, which might have implications for the construction of other paper-based microfluidic electrochemical devices.

Zusammenfassung

Auf Papier basierende Mikrofluidikplattformen ermöglichen die Miniaturisierung und Integration verschiedener Reaktionsprozesse und -technologien in On-Chip-Geräte, um eine breite Palette kostengünstiger kundenspezifischer Produkte unseres täglichen Lebens herzustellen. Diese Dissertation konzentriert sich auf die Anwendung des Mikrofluidikkonzepts auf Papierbasis, um tragbare und wegwerfbare elektrochemische Geräte mit einfacher Struktur und erschwinglichem Preis zu konstruieren. An drei Beispielen werden ihre strukturellen Merkmale, Arbeitsprinzipien und elektrochemischen Eigenschaften systematisch untersucht und diskutiert. Die Beispiele sind:

- ein mikrofluidischer elektrochemischer Sensor auf Papierbasis zum Nachweis von Schwermetallionen,
- eine mikrofluidische Formiat-Brennstoffzelle auf Papierbasis,
- eine mikrofluidische Hochleistungs-Aluminium-Luft-Batterie auf Papierbasis.

Der mikrofluidische elektrochemische Sensor basiert auf einem mikrofluidischen Papierkanal in Kombination mit einer dreidimensionalen (3D) Konfiguration. Alle drei Elektroden bestehen aus makelloser Graphitfolie ohne Modifikator oder Katalysator. Dieser kostengünstige, einfache und tragbare Sensor zeigt eine hohe Empfindlichkeit gegenüber dem Nachweis von Schwermetallionen in wässriger Lösung mit Nachweisgrenzen von bis zu 1,2 µg / L für Cd^{2+} und 1,8 µg / L für Pb^{2+}. Der Nachweis von Cd^{2+} und Pb^{2+} in anspruchsvolleren Umgebungen (z. B. Mineralwasser oder Lösungen, die störende Ionen enthalten) ist ebenfalls möglich. Die 3D-Konfiguration ist der Schlüsselfaktor für eine hohe Sensitivität. Der Mikrofluidsensor auf Papierbasis ist äußerst robust und die Messungen an einem einzelnen Gerät sind sehr gut reproduzierbar.

Die mikrofluidische Formiat-Brennstoffzelle auf Papierbasis wurde als umweltfreundliche Einweg-Stromquelle für tragbare und wegwerfbare Elektronikgeräte wie Sensorgeräte entwickelt. Die wichtigsten Strukturparameter, die sich auf die Gesamtleistung der Brennstoffzelle auswirken, wurden systematisch untersucht, einschließlich des Brennstoff-Crossovers, des Zellwiderstands, der Konzentration der Redox-Reaktanten, der Katalysatorbeladung und der Eigenschaften des mikrofluidischen Papierkanals. Nach der Optimierung kann auf einer einzelnen Zelle eine Leerlaufspannung von 0,86 V und eine maximale Leistungsdichte von 7,1 mW/cm^2 erreicht werden. Durch die Korrelation der

Zellleistung mit der Elektrolytflussrate in verschiedenen Papierkanälen wird erstmals deutlich, dass die textuellen Eigenschaften des Papiers die Zellleistung durch Stoffübergang und Verarmungseffekt stark beeinflussen.

Um eine höhere Energie- und Leistungsdichte bei miniaturisierten Leistungsbauelementen zu erzielen, wird ein Mikrofluidikkonzept auf Papierbasis eingeführt, um leistungsstarke Aluminium-Luft-Batterien herzustellen. Die einzigartige mikrofluidische Konfiguration verringert oder beseitigt die Hauptnachteile herkömmlicher Aluminium-Luft-Batterien, einschließlich Batterie-Selbstentladung, produktinduzierter Elektrodenpassivierung, teurer Luftelektrode und Hilfsflüssigkeitskontrollsystem. Die mikrofluidische Al-Luft-Batterie auf Papierbasis weist eine beeindruckende elektrochemische Leistung bei einer spezifischen Kapazität (2750 Ah/kg) und einer Energiedichte (2900 Wh/kg) auf, die beide unter den angegebenen miniaturisierten Energiequellen überlegen sind. Die mikrofluidische Al-Luft-Batterie auf Papierbasis kann durch einen einfachen Laminierungsprozess zu einer benutzerfreundlichen Taschenzellenkonfiguration zusammengebaut werden, die ein großes Potenzial für die reale Anwendung aufweist.

Diese Arbeit zeigt, dass Mikrofluidik auf Papierbasis ein attraktives Konzept für den Bau kostengünstiger, umweltfreundlicher, tragbarer und benutzerfreundlicher elektrochemischer Geräte mit verschiedenen Funktionen ist. Neben der Entwicklung und Herstellung leistungsfähiger mikrofluidischer elektrochemischer Systeme auf Papierbasis werden systematische Untersuchungen durchgeführt, um zu verstehen, wie die Systemkomponenten (z. B. Elektrodenmodifikation und -anordnung) und das mikrofluidische Strömungsverhalten (z. B. Strömungsrate und Diffusionsrate) die Anwendungseigenschaften beeinflussen. Die Erkenntnisse haben generelle Aussagekraft auch für das Design weiterer mikrofluidischer elektrochemischer Systeme auf Papierbasis.

Contents

1 Introduction and motivation

Microfluidics can be regarded both as a science of the flow behavior at micro-level and as a technology of design microfluidic devices with patterned micro channels/chambers/networks. The concept of microfluidics was firstly invented by the semiconductor industry and later expanded in the microelectromechanical system field, which enabled the miniaturization and integration of electronic circuits on a chip [1]. This integrated microfluidic approach, or known as lab-on-chip technology, provides a platform for many applications, especially for some chemical or biochemical processes in the field of analysis and energy conversion and storage [1-6]. For example, the first integrated microfluidic device for analysis was reported in 1979, when a miniature gas chromatograph consist of a capillary column, a sample injection system and a thermal conductivity detector was realized on a 5-cm-diameter silicon wafer [7]. Compared with conventional sized reaction systems, integrated microfluidic devices offer several benefits. First, the reaction processes on integrated microfluidic devices are less complex due to the absence of turbulent mixing. Second, microfluidics allows lower sample and chemical consumption with shorter reaction/separation time. Thus the device is capable to provide a rapid response that can be used to make an informed decision when a small amount of sample is introduced to the device [8]. Third, multiplexed and parallel assays can be realized with careful design of the microfluidic channels. Last but not least, the devices are small in size and light weighted, making it applicable for some portable uses, such as point-of-care diagnosis and in-field environmental analysis.

However, integrated microfluidic sensing devices can face limitations in real application. Traditional microfluidic devices are designed and constructed by molding, cutting, photolithography or etching glass, silicon or polymer substrate to produce microfluidic channels [7, 9-13]. These substrates are still considered to be expensive in the market, especially for the single-use devices. Auxiliary equipment, e.g., micropump, is usually needed to control the flow in the microfluidic channels, which increases the total cost of the system and at the same time makes it difficult to miniaturize the whole device [14-16]. Therefore, with a rapid growth of the market for disposable on-chip diagnostic and sensing devices, there is an increasing demand to replace the current substrates with low-cost, lightweight and green materials. Moreover, the auxiliary pressure control equipment should be eliminated to further reduce the total cost as well as the size of the devices.

Paper, made from natural cellulose, is the most widely used, cheapest and environmentally friendly substrate in everyday life. The microstructure of paper is randomly interconnected cellulose fiber, providing abundant pores and channels in micro/nanoscale [17, 18]. Fluids within paper substrate are driven by capillarity force and no external equipment, e.g., pump, is needed to control the microfluidics, making it possible to reduce the size and cost of the device to meet the real application. Moreover, various fabrication techniques have been developed to construct microfluidic paper channel, mainly including wax-printing (e.g., screen-printing, wax-dipping/impregnation), 2D shaping/cutting (e.g., knife plotter, CO_2 laser cutting), and 3D packaging/stacking (e.g., origami). These 2D or 3D methods are supposed to enable efficient transport of fluidics in both horizontal and/or vertical dimensions [19]. Whiteside and coworkers reported the first microfluidic paper-based analytical device (μPAD) for simultaneous detection of glucose and protein in 5 μL artificial urine [20]. This inexpensive, low-volume, portable microfluidic bioassays is fabricated on a patterned paper, where hydrophilic channels are created by building hydrophobic "walls" through photolithography of photoresist. When the liquid sample is added to the device, it will be directed by the microfluidic channels to respective reaction zones for glucose and protein test, where colour changes can be clearly observed as an indicator. Ever since then, μPADs have gained significant attention in the field of point-of-care diagnosis and in-field environmental analysis, due to their low price, flexibility, biocompatibility and renewability.

Early reported μPADs are based on colorimetric detection method, some of which are coupled with a camera phone or handheld optical colorimeter to quantify the concentration of the analytes [21-26]. Later on, electrochemical analysis is introduced to the microfluidic paper-based devices, which is supposed to be a more sensitive and quantitative detection method [27, 28]. Microfluidic paper-based electrochemical device (μPED) can be fabricated by design and arrangement of electrodes on the paper substrate. The analysis process is carried out by attaching the device to a handheld potentiostat together with a reading device (e.g., laptop or smart phone) [29-32]. The first μPED was demonstrated by Dungchai and coworkers in 2009 for simultaneous detection of glucose, lactate and uric acid in biological samples [8]. Over the past decade, these μPEDs for analysis have been widely developed in various field, e.g., medical diagnostic, environmental sensing and food safety assurance with low detection limits, showing great potential in on-site analysis, especially in some remote or developing areas.

Here in this thesis, the paper-based microfluidic concept is introduced to construct electrochemical sensing device for detection of heavy metal ions, which shows great potential in the field of fast and low-cost environmental analysis.

External power sources are usually required in the sensing systems to display and transmit data, or to carry out the sensing process. The most widely used power supplies for the miniaturized diagnostic and sensing devices are button cells, especially the lithium-based batteries [33]. However, for some single-use devices, such as a pregnancy test, the battery is thrown away together with the whole device after short time use, which often causes energy waste as well as environment pollution [34-36]. Therefore, there is an increasing demand for the miniaturized power sources, which can not only be integrated into the on-chip devices, but also have minimum impact on environment and human health. Microfluidics enables fabrication of miniaturized batteries/cells in a simpler way than their macro counterparts. For example, in a polymer electrolyte membrane fuel cell, proton exchange membrane is needed to separate the anode and cathode reaction. While in a microfluidic fuel cell system designed by Whitesides and coworkers, membrane can be omitted based on the parallel bilaminar flow of the anolyte and catholyte [37]. Moreover, microfluidic batteries/cells are compatible with microfluidic systems used for other purpose, such as the above discussed diagnostic and sensing devices, showing great potential in fabricating the self-powered microfluidic systems. Like microfluidic sensing systems, limitations of the conventional microfluidic power sources come from the expensive microfluidic substrates and the pressure control systems. With the development of paper-based microfluidics, the microfluidic power sources are able to meet the demand for the real applications. These paper-based microfluidic energy sources feature low-cost, lightweight and environmental benign nature, making them ideal substitution of button cells.

Here in this thesis, two typical electrical energy sources, formate fuel cell and aluminum-air battery, are designed and fabricated combining with paper-based microfluidics. Investigations are carried to optimize their performance, and to understand the key factors that influence the cell/battery performance.

2 Fundamentals

In this chapter, the fundamentals and principles underlying the researches in this thesis are introduced, along with the latest development in the field of paper-based microfluidic electrochemical devices. Part of the fundamentals were also published with in the review article ***ChemElectroChem DOI: 10.1002/celc.201901495.***

2.1 Basics of paper-based microfluidics

2.1.1 Paper chemistry

Paper is one of the mostly widely used substrate for information display and storage through history. Nowadays, paper materials have penetrated into many aspects in daily life, such as cleaning and packaging, due to their low price, biocompatibility, renewability and environmental benign nature. Paper is made from natural cellulose, an important component of the plant cell wall, which is considered as the most abundant biopolymer on earth [38]. The modern paper manufacturing process evolves dewatering, pressing and heating of wood cellulose pulp suspension, and the speed of paper production through the roll-to-roll (R2R) manufacture sometimes exceeds 100 km/h [17, 39].

Paper presents a hierarchic structure, as shown in **Figure 2.1**. From the molecular scale, the basic component of cellulose fiber is polysaccharide, which consists of a linear chain of glucose unites linked through β-1,4-glycosidic bonds [39]. The polysaccharide chains are bonded together via van der Waals force and hydrogen bond to form basic units known as elementary fibrils, with both crystalline and amorphous regions [18, 40]. Elementary fibrils grow together to form microfibrils, and thousands of the microfibrils are bonded together to form the cellulose fiber. The cellulose fibers are randomly interconnected by hydrogen bonding between the hydroxyl groups during the paper manufacturing process, resulting in the hierarchical porous structure of paper [39]. The longer cellulose fibers provide strength, while the shorter ones reduce pore size and provide opacity [18]. The properties of paper, such as weight, thickness, porosity and surface chemistry can be varied to a large extend during the paper manufacture or through paper functionalization.

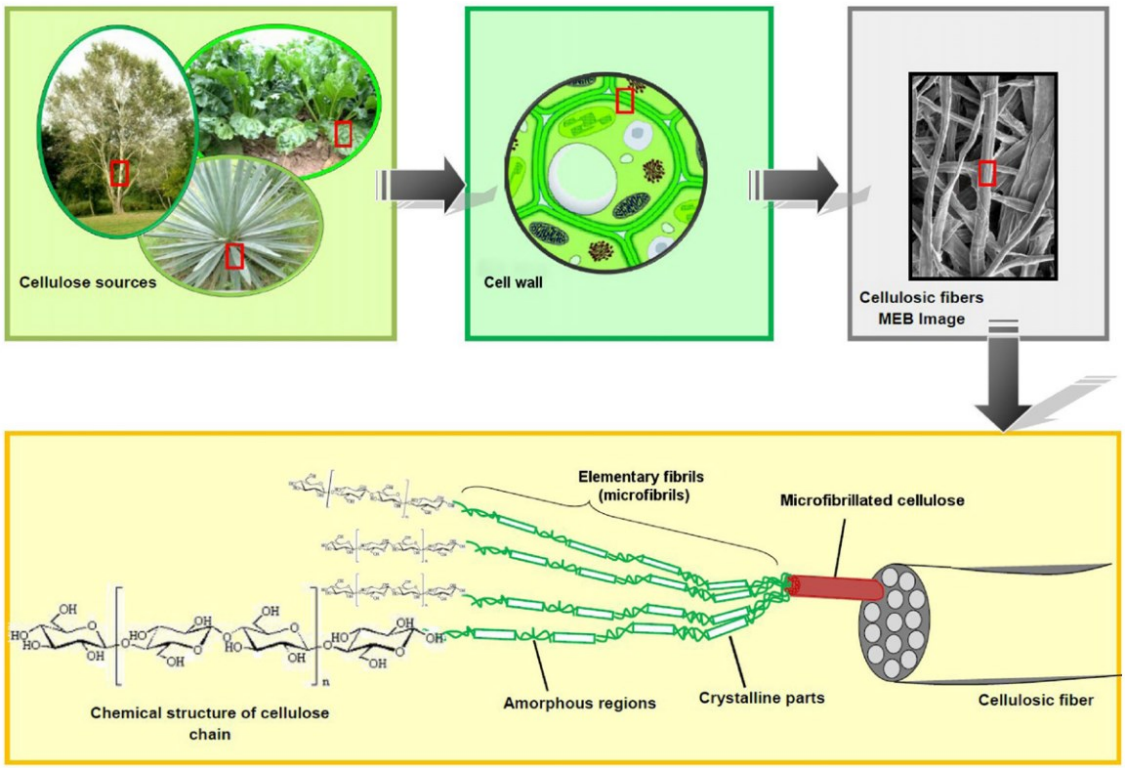

Figure 2.1 Schematic to show the hierarchical structure of cellulose fibers from cellulose source to cellulose molecules. Reprinted with permission [41]. Copyright 2012 Elsevier.

2.1.2 Microfluidics on paper

Microfluidics is a science and technology that fluid flow is manipulated in submillimeter level (1-1000 μm). The fluid flow in the microfluidic system is controlled at a low Reynold's number i.e. laminar flow, which means turbulent mixing is minimized and the only mechanism for mixing is diffusion [42]. Conventional microfluidics employs channels with dimensions of tens and hundreds micrometers, and the pressure-driven of flow in the microfluidic channels is usually operated by a syringe pump. In contrast, paper materials, made of cellulose fiber with abundant channels at micro level, provide a low-cost and pump-less alternative, as the fluid flow is generated through capillarity. The Reynold's number of fluid within paper matrix is at the order of 10^{-3} [43, 44].

The single-phase flow of a Newtonian liquid in an isotropic and rigid porous medium is governed by Darcy's law:

$$v = \frac{k}{\eta}\frac{\Delta P}{\Delta x} \tag{2.1}$$

where v is the flow velocity (m/s), k is the permeability (m^2), η is the viscosity (Pa·s), $\Delta P/\Delta x$ represents the pressure change per unit length (Pa/m). In the case of imbibition-driven flow in paper, the pressure is the capillarity suction given by the equation:

$$\Delta P = \frac{2\sigma cos\theta}{r} \tag{2.2}$$

where σ is the liquid-air surface tension (N/m), θ is the liquid-fiber contact angle, r is the average pore radius of the paper (m). With the increase of distance moved by the fluid on paper, the $\Delta P/\Delta x$ reduces as a function of time. Therefore, the flow rate of the fluid front within paper is usually in an unsteady pattern. Substituting the **Equation 2.1** into **Equation 2.2** gives:

$$x(t) = 2\sqrt{\frac{k\sigma t cos\theta}{\eta r}} \tag{2.3}$$

where x is the distance moved by the fluid front (m) under capillary pressure, σ is the liquid-air surface tension (N/m), t is the time (s), r is the average pore radius of the paper (m), θ is the liquid-fiber contact angle, and η is the viscosity (Pa·s). This result is the well-known Lucas-Washburn equation. Considering that permeability can be defined in terms of the product of the square of the effective pore diameter and a dimensionless constant which represents the shape and structure of the flow paths [45], the Lucas-Washburn equation are generally expressed as [46]:

$$x(t) = \sqrt{\frac{\sigma t r cos\theta}{2\eta}} \tag{2.4}$$

The key assumption for the Lucas-Washburn equation is that a homogenous perfectly wetting liquid flows in a homogenous isotropic porous medium in one dimension, and the cross sectional area of the porous media should stay constant [47]. According to the Lucas-Washburn equation, in a rectangular paper strip the flow velocity of the liquid front diminishes with the increase of time.

The imbibition behavior of fluid on porous substrate deviates from the classic Lucas-Washburn law ($v \propto t^{-1/2}$, **Figure 2.2a**) when the geometry of the substrate deviates from a rectangular shape [47, 48]. Mendez et al. investigated the imbibition behavior of lateral flow

on rectangular membrane appended to circular sectors, and quasi-stationary flow ($v \propto t^0$, **Figure 2.2b**) was found in the rectangular element, which is caused by the continuous increase of unwetted pore volume in the circular part [47]. A constant flow rate can also be observed in the hemispherical imbibition process from a point source into a homogenous semi-infinite porous medium (**Figure 2.2c**) [48]. A stationary flow is usually more preferable in the construction of microfluidic electrochemical devices, since electrochemical responses might be sensitive toward the flow rate of the analyte or electrolyte.

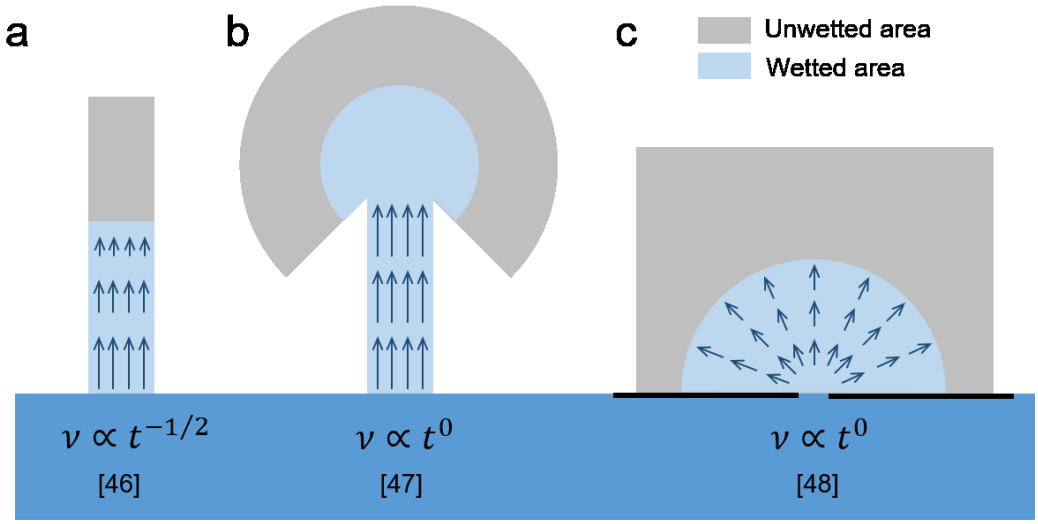

Figure 2.2 The imbibition behavior of fluid on porous substrate with different geometry [46-48].

The unique properties of laminar flow enable researchers to build up multiplexing on paper toward various applications. Yager et al. comprehensively studied the two-dimensional paper networks (2DPNs) with multi inlets, where multi fluidic flow can be precisely controlled on paper-based microfluidic channels [43, 49-51]. As shown in **Figure 2.3a**, dye solutions flow in parallel on a multi-inlet paper channel by capillarity force, and a clear boundary can be observed between the adjacent laminar flows. The outlet width radio of the fluidic flows can be controlled by adjusting the inlet length ratio. More complex 3D paper-based microfluidic system can be achieved by stacking or folding (origami technique) paper substrates, which enable the paper device to realize more functions, such as sample mixing or dilution (**Figure 2.3b-c**) [43, 52]. Besides flow rate control and multi flow construction, programming and timing of microfluidics can also be achieved on paper without using any external equipment or power [53]. For example, reagents can be delivered sequentially to the "detection region"

on 2DPNs consisting of three staggered inlets connected to the main channel (**Figure 2.3d**) [50]. Tunable-delay shunts for paper microfluidic devices can be created by placing a dissolvable barrier or a adsorbent pad on the channel (**Figure 2.3e-f**) [50, 54].

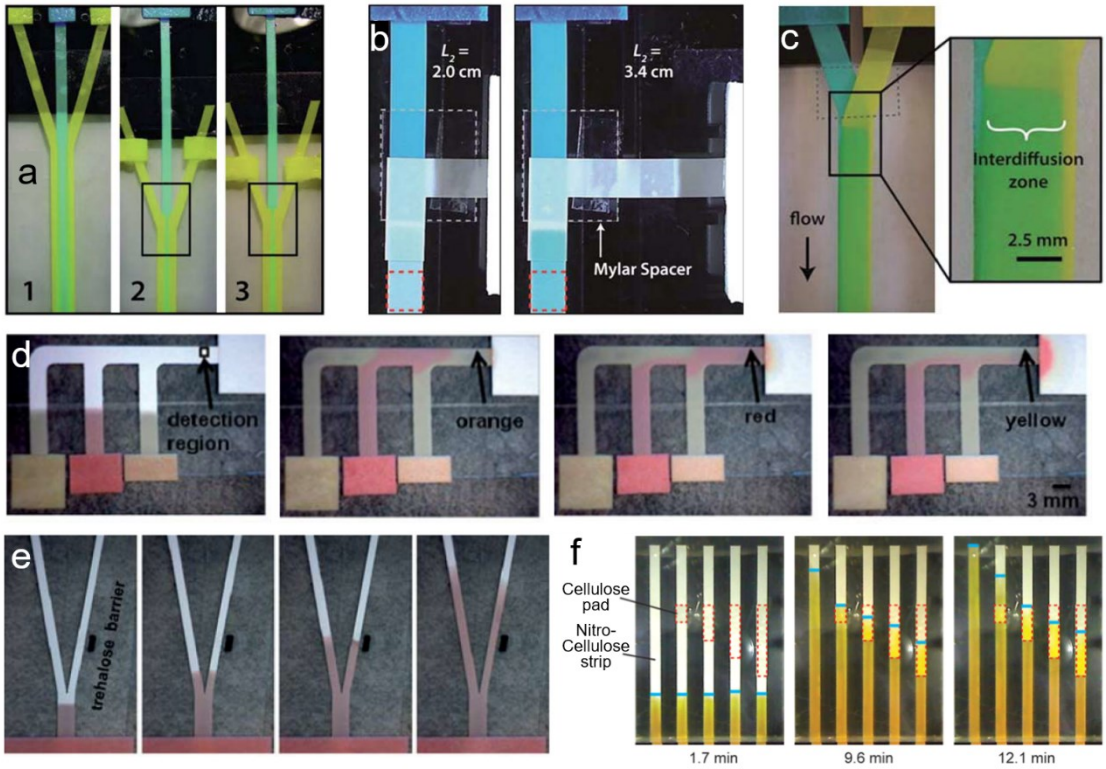

Figure 2.3 (a) Demonstration of flow control by varying inlet arm lengths in a three channel paper Y device. (b) Image of a paper dilutor. The top inlet stream contains erioglaucine, while the right inlet acts as the diluent (H_2O). Two different diluent arm lengths (left image: 2.0 cm, right image: 3.4 cm) result in different final concentration of the dye solution in the outlets. (c) Image of mixing process in a 3D flat Y-mixer. Inlets contain erioglaucine (left) and tartrazine (right). The interdiffusion of the two dyes results in the green color. Reprinted with permission [43]. Copyright 2010 Royal Society of Chemistry. (d) Demonstration of the programmed fluid delivery using a simple 2D paper network. (e) A dissolvable barrier on the right folk can be used to create a delay in the transport time of fluid. Reprinted with permission [50]. Copyright 2010 Royal Society of Chemistry. (f) Time-lapse images of the flow through nitrocellulose strips in the absence of and in contact with 7.6, 15.2, 22.9 and 30.5 mm shunts of cellulose placed on the nitrocellulose strip. Longer shuts produce longer delays. Reprinted with permission [54]. Copyright 2013 American Chemistry Society.

To sum up, precise control of microfluidic flow on paper, including flow rate, flow mixing, flow concentration, and flow time, can be realized on paper through careful design of paper geometry and construction of multi-channel 2D/3D configuration without expensive external control system and power supply. Thus, the paper-based microfluidics provides a feasible platform to fabricate low-cost, portable and disposable electrochemical devices.

2.2 Paper-based microfluidic electrochemical devices

2.2.1 Environmental sensing

Environmental pollution is one of the major problems that effects ecosystem and human health worldwide. The use of natural resources at a rate higher than natural's capacity to restore itself can result in pollution in air, water and land [55]. Among various pollutants, heavy metal ions pose severe threat to ecosystem and human health [56-59]. Unlike organic contaminants that would undergo microbial degradation process, heavy metal ions are non-biodegradable. Once migrate to human body, heavy metal ions could accumulate to hazardous levels and result in various diseases. For example, high blood lead levels can cause neurological damage, high blood pressure, kidney injury and anemia [58, 60-62]. Increase of cadmium level in human body may cause lung cancer, osteomalacia and proteinuria [58, 63-65]. Conventional laboratory techniques for elemental analysis, such as atomic absorption spectroscopy, X-ray fluorescence spectroscopy and inductively coupled plasma mass spectroscopy have been broadly used in heavy metal detection, presenting low detection limit and high sensitivity. However, the above-mentioned techniques are fixed-site laboratory analysis which relay on expensive equipment sets, tedious sample preparation and high skilled technicians, limiting their application in fast in-field analysis, especially in some developing areas with insufficient infrastructures [40, 66-68].

In comparison, electrochemical analysis is characterized as a low cost and flexible method for heavy metal detection with high sensitivity and selectivity [69]. Typical electrochemical detection of heavy metal detection includes two steps: 1) Deposition of heavy metal at a negative potential; 2) Oxidation of heavy metal through anodic stripping voltammetry (e.g., differential pulse voltammetry, square wave voltammetry) to generate an oxidation signal [70-72]. The position and the intensity of the oxidation peaks represent the type and concentration of the heavy metal ions, respectively. Thus, sufficient accumulation of heavy metals on the

working electrode during deposition is of significant importance. Conventional electrochemical detection of heavy metal ions is carried in an electrochemical cell, where working, counter and reference electrodes are immersed in the sample solution, and stirring is usually involved to increase the mass transfer during ion deposition [72-76]. This approach has several drawbacks. First, it is difficult to minimize the whole setup, making it not practical for in-field measurements [77]. Second, the electrodes, e.g., glass carbon electrode as working electrode, Pt wire as counter electrode, Ag/AgCl as reference electrode, are expensive. Repeated use of these electrodes needs careful cleaning before each measurement to avoid contamination [68]. To eliminate the use of electrochemical cell and expensive electrodes, a three-electrode system was fabricated by screen printing electrodes onto a substrate, and the measurement was carried out by placing a drop of sample on the three-electrode strip [78-80]. However, this approach shows limited sensitivity, because the deposition of the heavy metal is limited by the diffusion in the stagnant sample drop [58, 77].

To overcome this drawback, Nie et al. proposed a paper-based microfluidic electrochemical device, which comprised microfluidic channels patterned by photolithography, and screen-printed electrodes (carbon as both working and counter electrodes, Ag/AgCl as pseudo-reference electrode), as shown in **Figure 2.4a** [77]. The paper-based microfluidic electrochemical device was used to selectively detect Pd^{2+} in the mixture solution of Pd^{2+} and Zn^{2+}. Compared with stagnant sample, sample solution continuously flowing through the paper channel across the electrodes enhances the efficiency of the deposition of metal, and improves the detection limit (1.0 ppb), as shown in **Figure 2.4b**. Medina-Sanchez et al. also proposed a disposable electrochemical lateral flow paper-based sensing device for heavy metal detection (**Figure 2.4c**) [59]. The quantification of Pd^{2+} and Cd^{2+} in aqueous solution is demonstrated in a range from 10 to 100 ppb with a limit of detection of 7 and 11 ppb, respectively. The device is also able to detect Pd^{2+} and Cd^{2+} in mud-spiked sample, since the paper channel is able to efficiently filter the sample (**Figure 2.4d**).

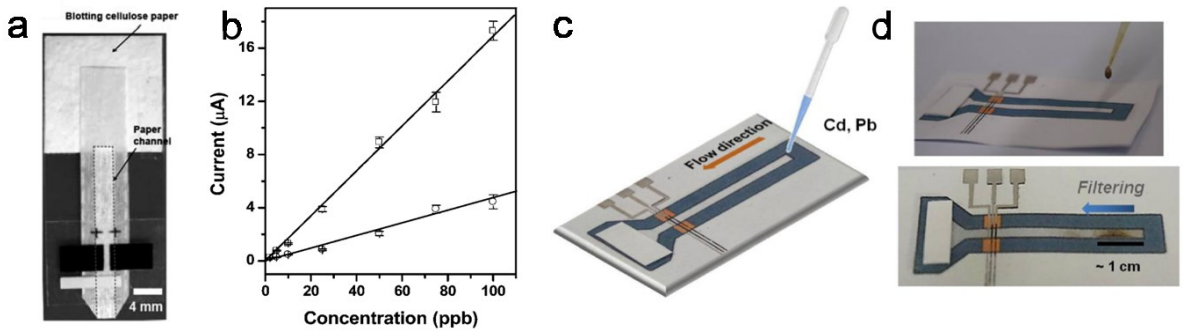

Figure 2.4 (a) A photograph of a hydrodynamic paper-based electrochemical sensing device for the measurement of heavy metal ions. (b) Calibration plots for the analysis of trace Pb^{2+}: a 100 μL solution of analytes placed in the electrodes (circle), and a solution of analytes continuously wicking along the paper channel in the μPEDs (square). Reprinted with permission [77]. Copyright 2010 Royal Society of Chemistry. (c) Picture of the lateral flow paper-based sensing device for heavy metal detection. (d) Photographs during the sampling (up) and measuring steps (bottom) of the mud sample by using the sensor. Reprinted with permission [59]. Copyright 2015 Springer.

For the detection of the trace amount of heavy metals, modification of the working electrode with electrocatalysts is usually needed to enhance the electro-deposition efficiency of the heavy metal ions. This electrode modification is supposed be especially important for heavy metal detection on miniaturized devices, because of the small amount of analyte evolved in the analysis process. In the early stage of electrochemical detection of heavy metal ions, mercury drop electrodes and mercury film modified electrodes are used to enhance the metal deposition by forming amalgam [70, 71, 81]. However, the notable toxicity of mercury limits the development of mercury sensor. Later on, less-toxic bismuth is introduced as an alternative electrode modifier for the electro-deposition of heavy metal ions, since it is able to promote the deposition efficiency by forming "fuse alloys" with various heavy metals that is analogous to the amalgam mercury forms [82-84]. There are general three methods to modify the electrode surface with bismuth. First method include pre-plating or *ex situ* plating through electro-depositing bismuth film onto the working electrode before transferring the electrode into heavy metal ions solution for analysis [74, 85]. Second is directly using a bulk bismuth electrode, or a bismuth modified electrode [58, 86-88]. Third is the most widely used *in situ* plating method by simultaneous deposition of bismuth ions and heavy metal ions in the same solution, in which carbon-based materials, such as glass carbon, carbon nanofibers/nanotubes,

graphite, graphene and carbon paste are commonly used as electrode substrate [57, 72, 85, 89-94]. However, the preparation of bismuth film electrode or bismuth modified electrode evolves tedious procedures, and the *in situ* method is not applicable for some online trance metal detection in natural or bio-environment. Besides, bismuth ions are easy to hydrolyze to form insoluble compound, thus pH of the sample solution should be controlled under 5, which makes it unpractical in biological and clinical analysis [58, 82]. Therefore, how to achieve a high detection sensitivity and low detection limit without use of modifier still remains challenging.

2.2.2 Fuel cells

A fuel cell is an environmentally friendly energy conversion system with high energy density, high efficiency and good reliability, which shows great prospects in construction of miniaturized power sources [33]. In a conventional polymer electrolyte membrane fuel cell (PEMEC), the energy source (fuel and oxidant) has to be transferred to the energy converter (catalyst and electrodes) continuously to sustain the chemical reaction. The two half cells are separated by a physical membrane, and H^+ (OH^-) is transferred from the anode (cathode) to the cathode (anode) part. The slow kinetics of oxygen reduction reaction (ORR) at the cathode is considered as one of the limitations in PEMEC [95-98]. Even though ORR has a faster kinetics in alkaline than in acidic electrolyte, the main challenge for alkaline fuel cells is the development of anion exchange membrane [99-101]. Nevertheless, membranes can be omitted in fuel cell system by employing microfluidic techniques with a non-strongly mixing laminar flow. Whitesides et al. proposed the first membraneless microfluidic fuel cell concept in 2002. In their work, the anolyte and catholyte flow parallel to one other in one microfluidic without membrane separation, and only diffusive exchange occurs across the interface between the two streams. An open circuit of 1.52 V is obtained at a flow rate of 25 µL/s based on vanadium redox couple [37]. Since then, the membraneless microfluidic fuel cells have been demonstrated by using different electrode catalysts, as well as different fuels and oxidants in both acid and alkaline solutions [102-113]. However, the main issue that limits the real application of membraneless microfluidic fuel cell lies in the use of external fluid control equipment, e.g., pump, which makes it challenging to miniaturize the device for portable applications.

A solution was proposed by Esquivel et al. in 2014 by presenting the first paper-based self-pumping microfluidic fuel cell [34]. Paper-based fuel cells benefit from the capillary-driven parallel laminar flows on paper, which enable the separation of anolyte and catholyte without using exchange membrane, and efficient mass transfer of fuel and oxidant without using pumps. As shown in **Figure 2.5a**, the anode (1 mg/cm^2 PtRu/C on Au/COP) is placed under the paper strip, while the cathode (1 mg/cm^2 Pt/C on carbon paper) is attached on top to facilitate oxygen access from the atmosphere. The fuel cell operates on the simultaneous addition of anolyte (methanol and KOH) and catholyte (KOH) in each inlet sample pads. An open circuit potential of 0.55 V and a maximum power density of 4.4 mW/cm^2 can be achieved on the paper-based microfluidic fuel cell (**Figure 2.5b**).

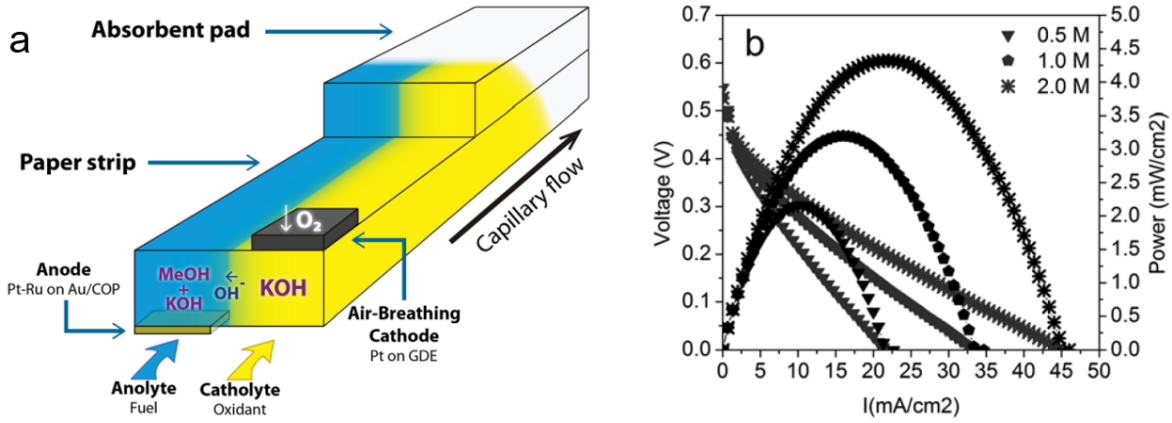

Figure 2.5 (a) Schematic of a paper-based microfluidic fuel cell design. (b) Polarization curves obtained at different KOH concentration using 4.0 M methanol. Reprinted with permission [34]. Creative Commons license 3.0.

Ever since then, many investigations have been carried out by varying electrocatalysts, electrolyte, electrochemical redox pair and cell configuration, in order to improve the performance, reduce the device cost, as well as simplify the operation process [114-120]. Arun et al. reported a self-pumping paper-based membraneless formic acid fuel cell by incorporating Hb-pencil stroked graphite as both anode and cathode electrodes on Y shaped paper channel [114]. This simple fuel cell with a pencil-on-paper configuration generates a constant open circuit voltage of 0.27 V for up to 1000 min, and a maximum power density of 32 mW/cm^2. Paper-based microfluidic direct formate fuel cells are reported by using formate and hydrogen peroxide as the anode fuel and cathode oxidant, respectively [115, 116]. Compared with methanol fuel cell and formic acid fuel cell, a much higher open circuit

voltage of 1.1 V can be achieved on the formate fuel cell operated in alkaline electrolyte with palladium as catalysts [116]. The paper-based microfluidic concept is also introduced to the field of biofuel cell, which is designed to produce electrical energy from physiological fluids. Gonzalez-Guerrero et al. presented an enzymatic paper-based glucose-oxygen microfluidic fuel cell with an open circuit voltage of 0.6 V and a maximum power density of 45 $\mu W/cm^2$ [117]. In order to meet the requirement of easy operation, some paper-based microfluidic fuel cells are designed on an I-shaped paper channel, and thus the cell is able to operate with a single-stream [34, 117, 118]. For example, Yan et al. developed a single-stream paper-based microfluidic fuel cell by using hydrogen peroxide (H_2O_2) as both fuel and oxidant [118]. The fuel cell is simply fabricated by placing the two electrodes symmetrically on a rectangular paper strip. The dual role of H_2O_2 is realized by selecting sliver nanowires and carbon nanotube-supported Prussian Blue as oxidation and reduction catalysts, respectively. The cell performance is recorded by using 2.0 M H_2O_2 in 1.5 M H_2SO_4 solution as both fuel and oxidant, and the open circuit voltage and peak power density reach 0.58 V and 0.88 mW/cm^2, respectively.

In a paper-based microfluidic fuel cell, the electrolyte flow behavior is also supposed to play a key role in determining the cell performance. The microfluidic behavior is effected by various factors, such as the intrinsic properties of the liquid (e.g., surface tension, density and viscosity), properties of the paper channel (e.g., fiber origin, pore size, porosity and geometry), as well as surrounding conditions (e.g., temperature and humidity) [44, 121-123]. For a paper-based microfluidic fuel cell operated with fixed redox pair and electrolyte under room temperature, the paper properties play an important role in the electrolyte flow control. However, the systematical study of the influence of paper properties on the electrolyte flow behavior and microfluidic fuel cell performance is still lacking.

2.2.3 Batteries

In the early design of paper-based batteries, paper takes function as electrode separator, electrolyte/redox species reservoir, or electrodes (e.g., electric conductive paper). For example, Lee developed a series biofluid/water-activated batteries using magnesium foil as anode, copper chloride loaded filter paper as cathode and paper tissue as electrolyte carrier [124, 125]. The battery can be activate by wetting the paper tissue with biofluid or tap water, and deliver a maximum voltage of 1.56 V a maximum power of 15.6 mW [125]. However,

the power output of the paper-based batteries decays fast probably due to their non-fluidic configuration.

Based on the wax printing and origami techniques, microfluidic channels can be precisely created on paper in a 2D or 3D configuration, proving a wide platform for design and fabrication of paper-based battery (stack) [126-131]. Thom et al. developed fluidic batteries which could be integrated in a paper-based analytical device [126]. As shown in **Figure 2.6a**, the fluidic batteries present a stacked 3D configuration, with the electrodes (Ag, Al), electrolyte ($AgNO_3$, $AlCl_3$) and salt bridge ($NaNO_3$) preloaded into the specific paper layers in dry state. The batteries can be directly activated by adding analyte to the sample input, powering a LED for fluorescence detection. Zhang et al. reported a 3D origami microfluidic paper-based battery based on a noble metal-free galvanic cell (C|$FeCl_3$|NaCl|$AlCl_3$|Al). The battery can provide a stable power output for 12 h [128]. Esquivel et al. developed a metal-free single-use primary battery PowerPAD (Power: Portable and Disposable) [35]. A pair of commercial available quinone compounds, p-benzoquinone and hydroquinone sulfonic acid potassium salt, were chosen as redox species [132]. As shown in **Figure 2.6b**, the battery is designed as a vertical capillary flow cell, composed of several patterned cellulose layers stacked together. The battery can be activated by adding water to the top inlet pad. When water flows through each half cell, the redox species are released and flow through the carbon electrodes toward the absorbent pad. Once the anolyte and catholyte contact with each other in the absorbent pad, the battery starts to generate power. The co-laminar flow in the paper matrix avoids turbulent mixing of the reactants, and only diffusion takes place at the flow interface, which enables the battery operate for up to 100 min. An open circuit voltage of 0.75 V and maximum power density of 6.8 mW/cm^2 can be achieved on a single battery. The output voltage of the battery can be scaled to 1.5-3.0 V to meet the demand of various electronics. The increasing disposal of single-used batteries such as lithium-ion batteries and metal-containing primary batteries, as well as insufficient battery cycling infrastructure cause severe environmental issues. Thus there is an increasing demand for environmentally friendly and disposable power sources. Choi group developed a series of origami paper-based bacteria batteries toward low-cost and biocompatible applications [130, 131]. The paper-based bacteria batteries are able to be activate by bacterial-containing liquid derived from renewable and sustainable water and wastewater sources. The paper-based bacteria batteries are able to connect in series by simply folding, in order to meet various power needs. As shown in

Figure 2.6c, upon adding one drop of bacteria-containing liquid derived from renewable and sustainable water and wastewater sources, the liquid flows through the microfluidic pathways and reaches each battery and generates power. An open circuit voltage of 0.93 V and a maximum output power of 48 nW (9.3 $\mu W/m^2$) can be obtained on four battery stack. However, the power output of these bacteria batteries is at nanowatt/microwatt-level, which is several magnitudes lower power density than the conventional galvanic cell batteries.

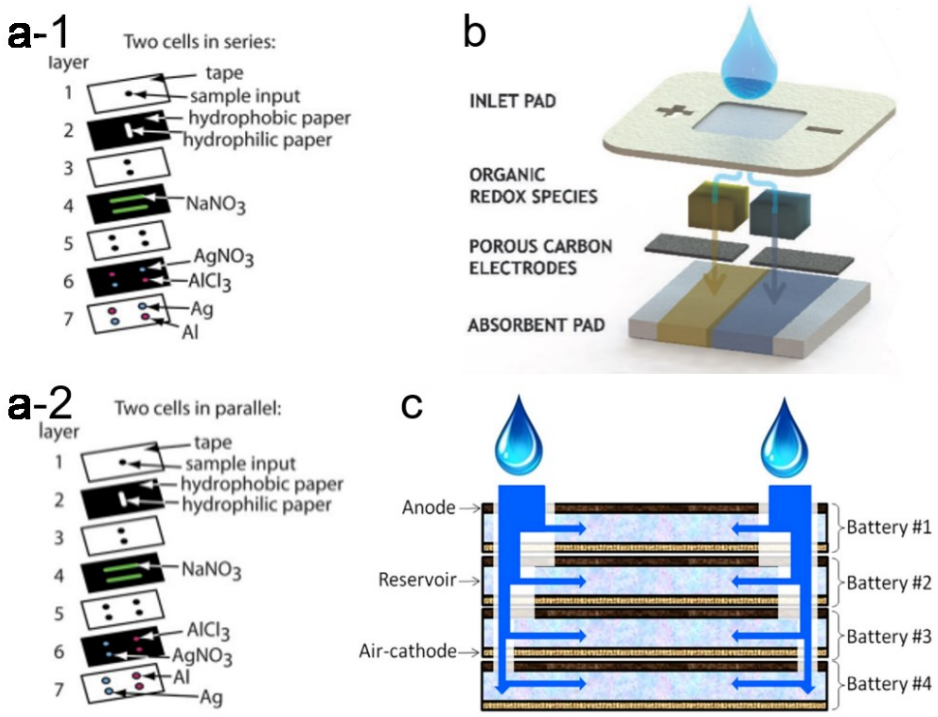

Figure 2.6 (a) The design of paper-based fluidic battery based on ($Ag|AgNO_3|NaNO_3|AlCl_3|Al$) galvanic cells. The number of galvanic cells can be varied, and can be connected in (a-1) series or (a-2) parallel. Reprinted with permission [126]. Copyright 2012 Royal Society of Chemistry. (b) Schematic diagram and working principle of the PowerPAD. Reprinted with permission [35]. Creative Commons license 4.0 (CC BY-NC 4.0). (c) Schematic diagram of the cross section of the bacteria battery stack. Reprinted with permission.[130] Copyright 2015 Elsevier.

Compared with ubiquitous primary batteries (e.g., Zn-MnO_2 battery), rechargeable batteries (e.g., lead-acid, nickel-metal hydride and lithium-ion battery), metal-air batteries have a notably higher theoretical energy density (**Figure 2.7**) [133, 134]. Metal-air batteries generate

electricity through redox reaction between the metal and oxygen from air. This feature makes them akin to a fuel cell, with the "fuel" being a metal [133]. Compared with fuel cells, the battery configuration, especially the anode design is less complicated in metal-air batteries [133]. The metal-air batteries hold great promise in the field of portable power devices. A good example is the commercialized zinc-air battery used in hearing aid. Among various metal anodes, aluminum has attracted increasing attentions due to its abundance, low price, non-toxicity and environmentally friendly nature [135-140]. Al-air battery own high theoretical energy density (8.1 kWh/kg) and high theoretical voltage (2.7 V). Therefore, Al-air battery is an attractive candidate to construct portable and disposable power sources, especially the ones require high energy density and power output as well as long running time.

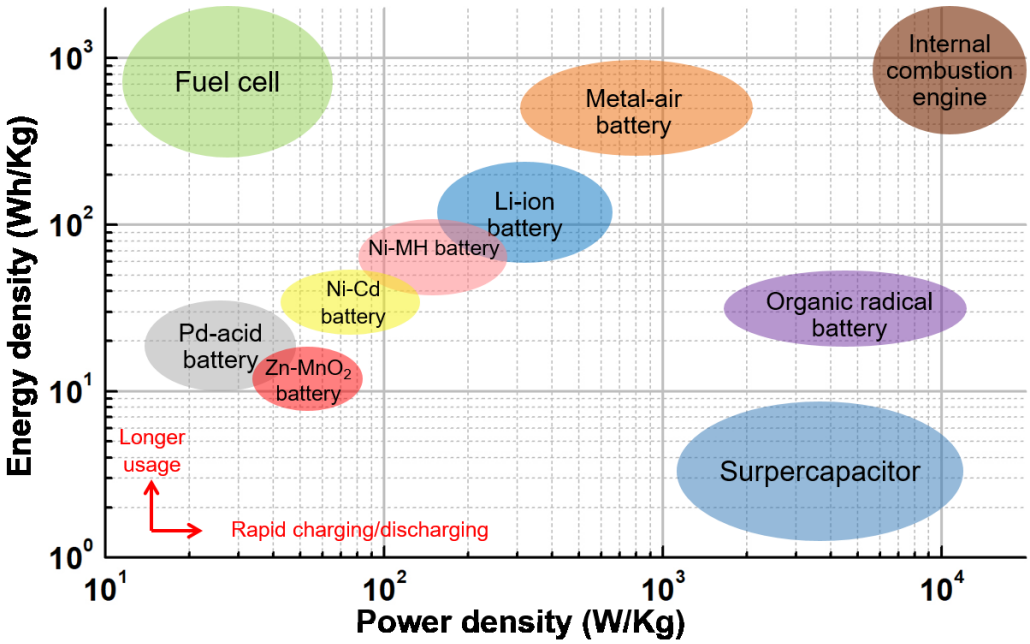

Figure 2.7 Ragone plot of different power sources.

However, several scientific and technical issues need to be tackled before their commercial-scale implementation. From anode side, the open-circuit corrosion reaction causes self-discharge and shortens the battery shelf-life [134, 136, 141]. During discharge, the formation of gel-like aluminum hydroxide and/or hydrated alumina results in anode surface passivation and prevents further discharging [139, 142]. From cathode side, high efficient oxygen reduction reaction (ORR) catalyst has to be developed to accelerate the slow kinetics of ORR, and a gas diffusion layer (GDL) has to be designed to facilitate the mass transfer of oxygen from ambient air to the catalyst layer reduction kinetics of oxygen [133-137, 143]. Since the

Al-air batteries are open systems using GDL, the alkaline electrolyte can react with atmospheric CO_2 to for carbonate precipitation, which reduces electrolyte conductivity, clogs the electrode pores, blocks the electrolyte channels and results in battery failure [133, 144, 145]. Therefore, the air electrode with active catalyst, gas diffusion layer, a selective membrane to block CO_2 and current collector appears to the most expensive and complex component of an Al-air battery. A lot of researches have been done to solve these problems. For example, modification of aluminum with other metals to form alloy and using non-aqueous electrolyte are both found to be effective to reduce the corrosion and passivation [146-154]. Besides, a lot of efforts have been made to explore novel electrocatalysts and develop sophisticated air electrodes to enhance ORR activity and increase the oxygen mass transfer rate [155-169]. However, these advancements inevitably lead to increased system costs, complicated battery construction and costly procedures for battery component recycling. Therefore, an affordable and easy method is high desired to solve the above mentioned issues to make portable Al-air battery applicable in the market.

References

[1] E.K. Sackmann, A.L. Fulton, D.J. Beebe, Nature 507 (2014) 181.

[2] D. Erickson, D. Li, Anal Chim. Acta 507 (2004) 11-26.

[3] S. Haeberle, R. Zengerle, Lab Chip 7 (2007) 1094-1110.

[4] M. Safdar, J. Jänis, S. Sanchez, Lab Chip 16 (2016) 2754-2758.

[5] G.M. Whitesides, Nature 442 (2006) 368.

[6] N.-T. Nguyen, S.T. Wereley, S.A.M. Shaegh, Fundamentals and applications of microfluidics, Artech house, 2019.

[7] S.C. Terry, J.H. Jerman, J.B. Angell, IEEE Trans. Electron Devices 26 (1979) 1880-1886.

[8] W. Dungchai, O. Chailapakul, C.S. Henry, Anal. Chem. 81 (2009) 5821-5826.

[9] E.T. Lagally, P.C. Simpson, R.A. Mathies, Sens. Actuators B 63 (2000) 138-146.

[10] R.M. Guijt, E. Baltussen, G. van der Steen, H. Frank, H. Billiet, T. Schalkhammer, F. Laugere, M. Vellekoop, A. Berthold, L. Sarro, Electrophoresis 22 (2001) 2537-2541.

[11] Y. Kikutani, A. Hibara, K. Uchiyama, H. Hisamoto, M. Tokeshi, T. Kitamori, Lab Chip 2 (2002) 193-196.

[12] Y. Kikutani, T. Horiuchi, K. Uchiyama, H. Hisamoto, M. Tokeshi, T. Kitamori, Lab Chip 2 (2002) 188-192.

[13] A. Li, S.H. Chan, N.-T. Nguyen, J. Micromech. Microeng. 17 (2007) 1107.

[14] R.F. Ismagilov, A.D. Stroock, P.J. Kenis, G. Whitesides, H.A. Stone, Appl. Phys. Lett. 76 (2000) 2376-2378.

[15] T.M. Squires, S.R. Quake, Rev. Mod. Phys. 77 (2005) 977.

[16] S.K. Yoon, G.W. Fichtl, P.J. Kenis, Lab Chip 6 (2006) 1516-1524.

[17] B. Yao, J. Zhang, T. Kou, Y. Song, T. Liu, Y. Li, Adv. Sci. 4 (2017) 1700107.

[18] Y. Zhang, L. Zhang, K. Cui, S. Ge, X. Cheng, M. Yan, J. Yu, H. Liu, Adv. Mater. 30 (2018) 1801588.

[19] A.K. Yetisen, M.S. Akram, C.R. Lowe, Lab Chip 13 (2013) 2210-2251.

[20] A.W. Martinez, S.T. Phillips, M.J. Butte, G.M. Whitesides, Angew. Chem. Int. Ed. 46 (2007) 1318-1320.

[21] A.W. Martinez, S.T. Phillips, E. Carrilho, S.W. Thomas III, H. Sindi, G.M. Whitesides, Anal. Chem. 80 (2008) 3699-3707.

[22] A.W. Martinez, S.T. Phillips, G.M. Whitesides, PNAS 105 (2008) 19606-19611.

[23] A.K. Ellerbee, S.T. Phillips, A.C. Siegel, K.A. Mirica, A.W. Martinez, P. Striehl, N. Jain, M. Prentiss, G.M. Whitesides, Anal. Chem. 81 (2009) 8447-8452.

[24] Y. Lu, W. Shi, L. Jiang, J. Qin, B. Lin, Electrophoresis 30 (2009) 1497-1500.

[25] Y. Lu, W. Shi, J. Qin, B. Lin, Anal. Chem. 82 (2009) 329-335.

[26] A.W. Martinez, S.T. Phillips, Z. Nie, C.-M. Cheng, E. Carrilho, B.J. Wiley, G.M. Whitesides, Lab Chip 10 (2010) 2499-2504.

[27] J. Mettakoonpitak, K. Boehle, S. Nantaphol, P. Teengam, J.A. Adkins, M. Srisa-Art, C.S. Henry, Electroanalysis 28 (2016) 1420-1436.

[28] K. Yamada, H. Shibata, K. Suzuki, D. Citterio, Lab Chip 17 (2017) 1206-1249.

[29] A. Pal, H.E. Cuellar, R. Kuang, H.F. Caurin, D. Goswami, R.V. Martinez, Adv. Mater. Technol. 2 (2017) 1700130.

[30] C. Zhao, M.M. Thuo, X. Liu, Sci. Technol. Adv. Mater. 14 (2013) 054402.

[31] Z.-X. Zou, J. Wang, H. Wang, Y.-Q. Li, Y. Lin, Talanta 94 (2012) 58-64.

[32] P.B. Lillehoj, M.-C. Huang, N. Truong, C.-M. Ho, Lab Chip 13 (2013) 2950-2955.

[33] C.K. Dyer, J. Power Sources 106 (2002) 31-34.

[34] J. Esquivel, F. Del Campo, J.G. de la Fuente, S. Rojas, N. Sabate, Energ. Environ. Sci. 7 (2014) 1744-1749.

[35] J.P. Esquivel, P. Alday, O.A. Ibrahim, B. Fernández, E. Kjeang, N. Sabaté, Adv. Energy Mater. 7 (2017) 1700275.

[36] L.-L. Shen, G.-R. Zhang, T. Venter, M. Biesalski, B.J. Etzold, Electrochim. Acta 298 (2019) 389-399.

[37] R. Ferrigno, A.D. Stroock, T.D. Clark, M. Mayer, G.M. Whitesides, J. Am. Chem. Soc. 124 (2002) 12930-12931.

[38] A.T. Vicente, A. Araújo, M.J. Mendes, D. Nunes, M.J. Oliveira, O. Sanchez-Sobrado, M.P. Ferreira, H. Águas, E. Fortunato, R. Martins, J. Mater. Chem. C 6 (2018) 3143-3181.

[39] D. Tobjörk, R. Österbacka, Adv. Mater. 23 (2011) 1935-1961.

[40] H. Hou, K.M. Zeinu, S. Gao, B. Liu, J. Yang, J. Hu, Energy Environ. Mater. 1 (2018) 113-131.

[41] N. Lavoine, I. Desloges, A. Dufresne, J. Bras, Carbohydr. Polym. 90 (2012) 735-764.

[42] M. Safdar, J. Janis, S. Sanchez, Lab Chip 16 (2016) 2754-2758.

[43] J.L. Osborn, B. Lutz, E. Fu, P. Kauffman, D.Y. Stevens, P. Yager, Lab Chip 10 (2010) 2659-2665.

[44] A. Böhm, F. Carstens, C. Trieb, S. Schabel, M. Biesalski, Microfluid. Nanofluid. 16 (2014) 789-799.

[45] J. Pappenheimer, E. Renkin, L. Borrero, Am. J. Physiol. Legacy Content 167 (1951) 13-46.

[46] E.W. Washburn, Phys. Rev. 17 (1921) 273.

[47] S. Mendez, E.M. Fenton, G.R. Gallegos, D.N. Petsev, S.S. Sibbett, H.A. Stone, Y. Zhang, G.P. López, Langmuir 26 (2009) 1380-1385.

[48] J. Xiao, H.A. Stone, D. Attinger, Langmuir 28 (2012) 4208-4212.

[49] E. Fu, P. Kauffman, B. Lutz, P. Yager, Sens. Actuators B 149 (2010) 325-328.

[50] E. Fu, B. Lutz, P. Kauffman, P. Yager, Lab Chip 10 (2010) 918-920.

[51] P. Kauffman, E. Fu, B. Lutz, P. Yager, Lab Chip 10 (2010) 2614-2617.

[52] J.R. Buser, S.A. Byrnes, C.E. Anderson, A.J. Howell, P.C. Kauffman, J.D. Bishop, M.H. Wheeler, S. Kumar, P. Yager, Anal. Methods 11 (2019) 336-345.

[53] D.M. Cate, J.A. Adkins, J. Mettakoonpitak, C.S. Henry, Anal. Chem. 87 (2014) 19-41.

[54] B.J. Toley, B. McKenzie, T. Liang, J.R. Buser, P. Yager, E. Fu, Anal. Chem. 85 (2013) 11545-11552.

[55] I.M. Krishna, V. Manickam, A. Shah, N. Davergave, Environmental management: science and engineering for industry, Butterworth-Heinemann, 2017.

[56] P. Apostoli, J. Chromatogr.B 778 (2002) 63-97.

[57] R.T. Kachoosangi, C.E. Banks, X. Ji, R.G. Compton, Anal. Sci. 23 (2007) 283-289.

[58] Z. Zou, A. Jang, E. MacKnight, P.-M. Wu, J. Do, P.L. Bishop, C.H. Ahn, Sens. Actuators B 134 (2008) 18-24.

[59] M. Medina-Sánchez, M. Cadevall, J. Ros, A. Merkoçi, Anal. Bioanal. Chem. 407 (2015) 8445-8449.

[60] D. Gidlow, Occup. Med. 54 (2004) 76-81.

[61] M.F.M. Noh, I.E. Tothill, Anal. Bioanal. Chem. 386 (2006) 2095-2106.

[62] W. Lo, H. Chua, K.-H. Lam, S.-P. Bi, Chemosphere 39 (1999) 2723-2736.

[63] T.O. Llewellyn, Cadmium (materials flow), United States. Department of the Interior. Bureau of Mines, 1994.

[64] D.G. Bostwick, H.B. Burke, D. Djakiew, S. Euling, S.m. Ho, J. Landolph, H. Morrison, B. Sonawane, T. Shifflett, D.J. Waters, Cancer 101 (2004) 2371-2490.

[65] E.L. Silva, P. dos Santos Roldan, J. Hazard. Mater. 161 (2009) 142-147.

[66] N.A. Meredith, C. Quinn, D.M. Cate, T.H. Reilly, J. Volckens, C.S. Henry, Analyst 141 (2016) 1874-1887.

[67] J. Kudr, O. Zitka, M. Klimanek, R. Vrba, V. Adam, Sens. Actuators B 246 (2017) 578-590.

[68] S. Li, C. Zhang, S. Wang, Q. Liu, H. Feng, X. Ma, J. Guo, Analyst 143 (2018) 4230-4246.

[69] G. Hanrahan, D.G. Patil, J. Wang, J. Environ. Monit. 6 (2004) 657-664.

[70] T. Florence, J. Electroanal. Chem. Interfacial Electrochem. 27 (1970) 273-281.

[71] H.P. Wu, Anal. Chem. 68 (1996) 1639-1645.

[72] J. Wang, J. Lu, S.B. Hocevar, P.A. Farias, B. Ogorevc, Anal. Chem. 72 (2000) 3218-3222.

[73] J. Wang, J. Lu, Ü.A. Kirgöz, S.B. Hocevar, B. Ogorevc, Anal. Chim. Acta 434 (2001) 29-34.

[74] G. Kefala, A. Economou, A. Voulgaropoulos, M. Sofoniou, Talanta 61 (2003) 603-610.

[75] N. Lezi, A. Economou, P.A. Dimovasilis, P.N. Trikalitis, M.I. Prodromidis, Anal. Chim. Acta 728 (2012) 1-8.

[76] G.-H. Hwang, W.-K. Han, J.-S. Park, S.-G. Kang, Sens. Actuators B 135 (2008) 309-316.

[77] Z. Nie, C.A. Nijhuis, J. Gong, X. Chen, A. Kumachev, A.W. Martinez, M. Narovlyansky, G.M. Whitesides, Lab Chip 10 (2010) 477-483.

[78] R.O. Kadara, I.E. Tothill, Anal. Bioanal. Chem. 378 (2004) 770-775.

[79] R.O. Kadara, I.E. Tothill, Anal. Chim. Acta 623 (2008) 76-81.

[80] G. Aragay, J. Pons, A. Merkoçi, J. Mater. Chem. 21 (2011) 4326-4331.

[81] J.W. Ross, R.D. DeMars, I. Shain, Anal. Chem. 28 (1956) 1768-1771.

[82] S.B. Hočevar, B. Ogorevc, J. Wang, B. Pihlar, Electroanalysis 14 (2002) 1707-1712.

[83] A. Economou, TrAC Trends Anal. Chem. 24 (2005) 334-340.

[84] J. Wang, Electroanalysis 17 (2005) 1341-1346.

[85] A. Królicka, R. Pauliukait, I. Švancara, R. Metelka, A. Bobrowski, E. Norkus, K. Kalcher, K. Vytřas, Electrochem. Commun. 4 (2002) 193-196.

[86] R. Pauliukaitė, S.B. Hočevar, B. Ogorevc, J. Wang, Electroanalysis 16 (2004) 719-723.

[87] M. Bučková, P. Gründler, G.U. Flechsig, Electroanalysis 17 (2005) 440-444.

[88] C. Kokkinos, A. Economou, I. Raptis, C.E. Efstathiou, T. Speliotis, Electrochem. Commun. 9 (2007) 2795-2800.

[89] G. Liu, Y. Lin, Y. Tu, Z. Ren, Analyst 130 (2005) 1098-1101.

[90] I. Švancara, L. Baldrianová, E. Tesařová, S.B. Hočevar, S.A. Elsuccary, A. Economou, S. Sotiropoulos, B. Ogorevc, K. Vytřas, Electroanalysis 18 (2006) 177-185.

[91] L. Baldrianova, I. Svancara, S. Sotiropoulos, Anal. Chim. Acta 599 (2007) 249-255.

[92] G.H. Hwang, W.K. Han, J.S. Park, S.G. Kang, Talanta 76 (2008) 301-308.

[93] H. Xu, L. Zeng, S. Xing, Y. Xian, G. Shi, L. Jin, Electroanalysis 20 (2008) 2655-2662.

[94] J. Li, S. Guo, Y. Zhai, E. Wang, Electrochem. Commun. 11 (2009) 1085-1088.

[95] Y. Bing, H. Liu, L. Zhang, D. Ghosh, J. Zhang, Chem. Soc. Rev. 39 (2010) 2184-2202.

[96] L. Lin, Q. Zhu, A.-W. Xu, J. Am. Chem. Soc. 136 (2014) 11027-11033.

[97] G.R. Zhang, M. Munoz, B.J. Etzold, Angew. Chem. Int. Ed. 55 (2016) 2257-2261.

[98] G.-R. Zhang, T. Wolker, D.J. Sandbeck, M. Munoz, K.J. Mayrhofer, S. Cherevko, B.J. Etzold, ACS Catal. 8 (2018) 8244-8254.

[99] G. Merle, M. Wessling, K. Nijmeijer, J. Membr. Sci. 377 (2011) 1-35.

[100] J.R. Varcoe, P. Atanassov, D.R. Dekel, A.M. Herring, M.A. Hickner, P.A. Kohl, A.R. Kucernak, W.E. Mustain, K. Nijmeijer, K. Scott, Energ. Environ. Sci. 7 (2014) 3135-3191.

[101] I. Martinaiou, T. Wolker, A. Shahraei, G.-R. Zhang, A. Janßen, S. Wagner, N. Weidler, R.W. Stark, B.J.M. Etzold, U.I. Kramm, J. Power Sources 375 (2018) 222-232.

[102] E.R. Choban, L.J. Markoski, A. Wieckowski, P.J. Kenis, J. Power Sources 128 (2004) 54-60.

[103] J.L. Cohen, D.J. Volpe, D.A. Westly, A. Pechenik, H.D. Abruña, Langmuir 21 (2005) 3544-3550.

[104] R.S. Jayashree, L. Gancs, E.R. Choban, A. Primak, D. Natarajan, L.J. Markoski, P.J. Kenis, J. Am. Chem. Soc. 127 (2005) 16758-16759.

[105] M.-H. Chang, F. Chen, N.-S. Fang, J. Power Sources 159 (2006) 810-816.

[106] F. Chen, M.-H. Chang, M.-K. Lin, Electrochim. Acta 52 (2007) 2506-2514.

[107] E. Kjeang, J. McKechnie, D. Sinton, N. Djilali, J. Power Sources 168 (2007) 379-390.

[108] W. Sung, J.-W. Choi, J. Power Sources 172 (2007) 198-208.

[109] E. Kjeang, R. Michel, D.A. Harrington, N. Djilali, D. Sinton, J. Am. Chem. Soc. 130 (2008) 4000-4006.

[110] F.R. Brushett, R.S. Jayashree, W.-P. Zhou, P.J. Kenis, Electrochim. Acta 54 (2009) 7099-7105.

[111] D. Morales-Acosta, L.A. Godinez, L. Arriaga, J. Power Sources 195 (2010) 1862-1865.

[112] M.R. Thorson, F.R. Brushett, C.J. Timberg, P.J. Kenis, J. Power Sources 218 (2012) 28-33.

[113] M.J. González-Guerrero, J.P. Esquivel, D. Sánchez-Molas, P. Godignon, F.X. Muñoz, F.J. Del Campo, F. Giroud, S.D. Minteer, N. Sabaté, Lab Chip 13 (2013) 2972-2979.

[114] R.K. Arun, S. Halder, N. Chanda, S. Chakraborty, Lab Chip 14 (2014) 1661-1664.

[115] T.S. Copenhaver, K.H. Purohit, K. Domalaon, L. Pham, B.J. Burgess, N. Manorothkul, V. Galvan, S. Sotez, F.A. Gomez, J.L. Haan, Electrophoresis 36 (2015) 1825-1829.

[116] V. Galvan, K. Domalaon, C. Tang, S. Sotez, A. Mendez, M. Jalali-Heravi, K. Purohit, L. Pham, J. Haan, F.A. Gomez, Electrophoresis 37 (2016) 504-510.

[117] M.J. González-Guerrero, F.J. del Campo, J.P. Esquivel, F. Giroud, S.D. Minteer, N. Sabaté, J. Power Sources 326 (2016) 410-416.

[118] X. Yan, A. Xu, L. Zeng, P. Gao, T. Zhao, Energy Technol. 6 (2018) 140-143.

[119] C.W.N. Villarrubia, C. Lau, G.P. Ciniciato, S.O. Garcia, S.S. Sibbett, D.N. Petsev, S. Babanova, G. Gupta, P. Atanassov, Electrochem. Commun. 45 (2014) 44-47.

[120] J. Esquivel, J. Buser, C. Lim, C. Domínguez, S. Rojas, P. Yager, N. Sabaté, J. Power Sources 342 (2017) 442-451.

[121] E. Elizalde, R. Urteaga, C.L. Berli, Lab Chip 15 (2015) 2173-2180.

[122] K. Chaudhury, S. Kar, S. Chakraborty, Appl. Phys. Lett. 109 (2016) 224101.

[123] N. Walji, B.D. MacDonald, Micromachines 7 (2016) 73.

[124] K.B. Lee, J. Micromech. Microeng. 15 (2005) S210-S214.

[125] K.B. Lee, J. Micromech. Microeng. 16 (2006) 2312-2317.

[126] N.K. Thom, K. Yeung, M.B. Pillion, S.T. Phillips, Lab Chip 12 (2012) 1768-1770.

[127] N.K. Thom, G.G. Lewis, M.J. DiTucci, S.T. Phillips, RSC Adv. 3 (2013) 6888-6895.

[128] X. Zhang, J. Li, C. Chen, B. Lou, L. Zhang, E. Wang, Chem. Commun. 49 (2013) 3866-3868.

[129] Y. Koo, J. Sankar, Y. Yun, Biomicrofluidics 8 (2014) 054104.

[130] H. Lee, S. Choi, Nano Energy 15 (2015) 549-557.

[131] M. Mohammadifar, S. Choi, Adv. Mater. Technol. 2 (2017) 1700127.

[132] O.A. Ibrahim, P. Alday, N. Sabaté, J.P. Esquivel, E. Kjeang, J. Electrochem. Soc. 164 (2017) A2448-A2456.

[133] F. Cheng, J. Chen, Chem. Soc. Rev. 41 (2012) 2172-2192.

[134] Y. Li, J. Lu, ACS Energy Lett. 2 (2017) 1370-1377.

[135] Y. Liu, Q. Sun, W. Li, K.R. Adair, J. Li, X. Sun, Green Energ. Environ. 2 (2017) 246-277.

[136] L. Fan, H. Lu, J. Leng, Electrochim. Acta 165 (2015) 22-28.

[137] Q. Li, N.J. Bjerrum, J. Power Sources 110 (2002) 1-10.

[138] S. Yang, H. Knickle, J. Power Sources 112 (2002) 162-173.

[139] N. Jayaprakash, S.K. Das, L.A. Archer, Chem. Commun. 47 (2011) 12610-12612.

[140] D.J. Kim, D.-J. Yoo, M.T. Otley, A. Prokofjevs, C. Pezzato, M. Owczarek, S.J. Lee, J.W. Choi, J.F. Stoddart, Nat. Energy (2018) 1.

[141] Z. Zhang, C. Zuo, Z. Liu, Y. Yu, Y. Zuo, Y. Song, J. Power Sources 251 (2014) 470-475.

[142] M. Pino, D. Herranz, J. Chacon, E. Fatás, P. Ocón, J. Power Sources 326 (2016) 296-302.

[143] M. Mokhtar, M.Z.M. Talib, E.H. Majlan, S.M. Tasirin, W.M.F.W. Ramli, W.R.W. Daud, J. Sahari, J. Ind. Eng. Chem. 32 (2015) 1-20.

[144] Z.P. Cano, D. Banham, S. Ye, A. Hintennach, J. Lu, M. Fowler, Z. Chen, Nat. Energy 3 (2018) 279.

[145] Y. Li, H. Dai, Chem. Soc. Rev. 43 (2014) 5257-5275.

[146] H. El Shayeb, F.A. El Wahab, S.Z. El Abedin, Corros. Sci. 43 (2001) 655-669.

[147] M. Nestoridi, D. Pletcher, J.A. Wharton, R.J. Wood, J. Power Sources 193 (2009) 895-898.

[148] I. Smoljko, S. Gudić, N. Kuzmanić, M. Kliškić, J. Appl. Electrochem. 42 (2012) 969-977.

[149] D. Egan, C.P. De León, R. Wood, R. Jones, K. Stokes, F. Walsh, J. Power Sources 236 (2013) 293-310.

[150] J. Ma, J. Wen, J. Gao, Q. Li, J. Electrochem. Soc. 161 (2014) A376-A380.

[151] D. Gelman, B. Shvartsev, Y. Ein-Eli, J. Mater. Chem. A 2 (2014) 20237-20242.

[152] M. Kar, T.J. Simons, M. Forsyth, D.R. MacFarlane, Phys. Chem. Chem. Phys. 16 (2014) 18658-18674.

[153] R. Revel, T. Audichon, S. Gonzalez, J. Power Sources 272 (2014) 415-421.

[154] H. Wang, S. Gu, Y. Bai, S. Chen, F. Wu, C. Wu, ACS Appl. Mater. Interfaces 8 (2016) 27444-27448.

[155] G.-R. Zhang, S. Wöllner, Appl. Catal. B-Environ. 222 (2018) 26-34.

[156] L.-L. Shen, G.-R. Zhang, S. Miao, J. Liu, B.-Q. Xu, ACS Catal. 6 (2016) 1680-1690.

[157] H. Pang, Y. Wang, M. Zhao, Q. Zhao, Q. Li, Nanoscale (2018).

[158] X. Li, Y. Fang, X. Lin, M. Tian, X. An, Y. Fu, R. Li, J. Jin, J. Ma, J. Mater. Chem. A 3 (2015) 17392-17402.

[159] G.-L. Chai, K. Qiu, M. Qiao, M.-M. Titirici, C. Shang, Z. Guo, Energ. Environ. Sci. 10 (2017) 1186-1195.

[160] S. Liu, Z. Wang, S. Zhou, F. Yu, M. Yu, C.Y. Chiang, W. Zhou, J. Zhao, J. Qiu, Adv. Mater. 29 (2017) 1700874.

[161] H. Peng, F. Liu, X. Liu, S. Liao, C. You, X. Tian, H. Nan, F. Luo, H. Song, Z. Fu, P. Huang, ACS Catal. 4 (2014) 3797-3805.

[162] X.-H. Yan, B.-Q. Xu, J. Mater. Chem. A 2 (2014) 8617-8622.

[163] T.Y. Ma, J. Ran, S. Dai, M. Jaroniec, S.Z. Qiao, Angew. Chem. Int. Ed. 54 (2015) 4646-4650.

[164] J. Zhang, Z. Zhao, Z. Xia, L. Dai, Nat. Nanotechnol. 10 (2015) 444.

[165] S. Li, C. Cheng, H.W. Liang, X. Feng, A. Thomas, Adv. Mater. 29 (2017) 1700707.

[166] C. Tang, B. Wang, H.F. Wang, Q. Zhang, Adv. Mater. 29 (2017) 1703185.

[167] Y. Xu, Y. Zhao, J. Ren, Y. Zhang, H. Peng, Angew. Chem. 128 (2016) 8111-8114.

[168] J. Li, Z. Zhou, K. Liu, F. Li, Z. Peng, Y. Tang, H. Wang, J. Power Sources 343 (2017) 30-38.

[169] M. Zhang, Q. Dai, H. Zheng, M. Chen, L. Dai, Adv. Mater. 30 (2018) 1705431.

3 Aim and scope of the thesis

The state-of-the-art shows that microfluidics utilizing capillary driven force within paper matrix is a highly attractive substitute to liquid guides, valves, and pumps, in terms of autonomously transporting small amount of liquid. Paper-based microfluidics provides a wide platform to fabricate low-cost, highly flexible and environmentally friendly electronics, especially in the field of portable electrochemical analysis and miniaturized power sources. Despite that many studies demonstrate the possibility to use paper-based microfluidics to develop electrochemical devices, quite few of them discusses how the device configuration (e.g., electrode arrangement, catalyst/modifier type and amount, electrolyte concentrations, flow rates etc.) influence the device performance. Microfluidics within paper largely depends on the paper properties and configuration. However, the selection criteria of paper substrate are not always clearly discussed in the design of paper-based microfluidic devices, especially the influence of paper properties on the fluidic properties as well as the electrochemical performance. Thus, the real potential of these new devices is studied only to a limited extend.

This thesis aims to show the benefit of holistic studies in the field of microfluidic electrochemical devices, which covers the fields of electrochemistry, chemical engineering and paper chemistry. With this approach three exemplary applications of paper-based electrochemical devices in the field of environmental sensing and power generation will be studied. The applications are paper-based microfluidic:

- electrochemical sensor of heavy metal ions,
- formate fuel cell,
- high-performing aluminum-air battery.

Overarching research questions for all applications are: 1) How the configuration of the paper-based microfluidic electrochemical device influences its overall performance; 2) How paper-based microfluidics facilitates the reaction process in the miniaturized electronic devices; 3) How to precisely control the microfluidic behavior within 2D/3D paper matrix; 4) How to take advantage of the quasi-stationary microfluidic flow on paper to transfer reactant/product continuously and steadily; 5) How does the mass transfer of reactant/product within the microfluidic paper channel effects the performance of the electronic devices.

The results for the three applications were published in three self-contained research articles. This cumulative thesis refers to these three articles, which are presented in chapter 4, chapter 5 and chapter 6 where the motivation, objectives, experimental procedure and summary of the major results are given individually. Chapter 7 deduces some general guidelines and overarching conclusions, which can be drawn from the sum of research of all three paper-based electrochemical devices.

4 Modifier-free microfluidic electrochemical sensor for heavy metal detection

Liu-Liu Shen [a], Gui-Rong Zhang [a,*], Wei Li [b], Markus Biesalski [b], and Bastian J.M. Etzold [a,*]

[a] Ernst-Berl-Institut für Technische und Makromolekulare Chemie, Department of Chemistry, Technische Universität Darmstadt, Alarich-Weiss-Straße 8, 64287 Darmstadt, Germany

[b] Laboratory of Macromolecular Chemistry and Paper Chemistry, Department of Chemistry, Technische Universität Darmstadt, Petersenstrasse 22, 64287 Darmstadt, Germany

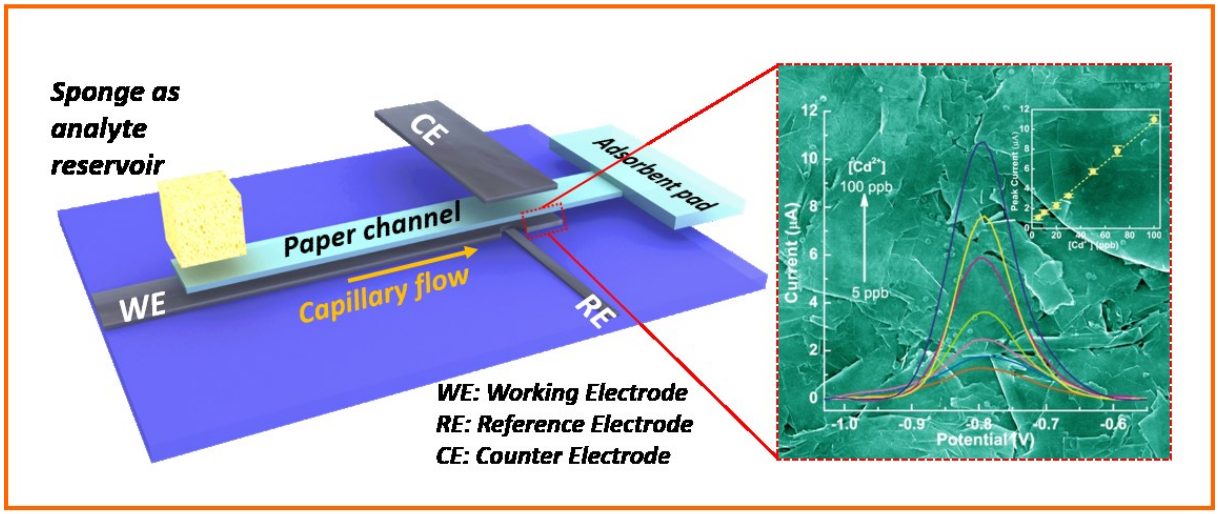

Redrafted from ***ACS Omega 2 (2017) 4593-4603.***

Abstract

Heavy metal pollution poses severe threat to ecological systems and presents a great challenge for global sustainability. Portable point-of-care sensing platform for detection/monitoring of heavy metal pollution in the environment is urgently demanded. Herein, a highly sensitive, robust and low-cost microfluidic electrochemical carbon-based sensor (μCS) for detection of trace heavy metals is presented. The miniaturized μCS devices are based on a microfluidic paper channel combined with a novel 3D layout with working and counter electrodes facing each other and analyte flowing along the microfluidic channel between these two electrodes. Pristine graphite foil free of any surface modifier is not only used as the electronically conductive pad but also directly employed as the working electrode for fabricating the μCS. The resulting simple and portable device was applied in Cd^{2+} and Pb^{2+} detection by using square wave anodic stripping voltammetry. Detection limits down to 1.2 μg/L for Cd^{2+} and 1.8 μg/L for Pb^{2+} can be achieved over the μCS, respectively. The μCS devices are also found to be highly robust and 10 repetitive measurements with a single μCS device resulted to be highly reproducible.

Keywords: electrochemical sensor, microfluidics, microfluidic paper, graphite foil, heavy metal detection, square wave voltammetry

4.1 Introduction

Heavy metals are widely used in manufacture of batteries, pigments, alloys, electroplating and coating et al. [1, 2]. However, mining, pouring, casting, processing and inappropriate disposal of heavy metals have made them hazard pollutants to the environment [3-6]. Their toxic and non-biodegradable nature impose severe risks to human health [6-9]. For example, increasing amounts of lead (Pb) in human body, as indicated by blood Pb levels, can impair neurobehavioral development in children, increase blood pressure, and cause kidney injury and anaemia [2, 5, 9, 10]. Cadmium (Cd) has been proved to be a carcinogenic agent and may cause lung cancer, osteomalacia and proteinuria, even at low doses [1, 9, 11, 12]. Conventional methods for heavy metal detection are mainly based on atomic adsorption spectroscopy (AAS), X-ray fluorescence (XFS), inductively coupled plasma atomic emission spectroscopy (ICP-AES) and inductively coupled plasma mass spectroscopy (ICP-MS) [5, 12-14]. Nevertheless, these ponderous, sophisticated and expensive instruments are not suitable

for fast and point-of-care analysis [5, 13]. Hence, researchers have been striving to develop simple, cost-effective and also portable sensing devices for fast and point-of-care analysis of heavy metal pollution in the environment, especially in developing countries and areas with insufficient infrastructures.

Numerous detection platforms including colorimetric, fluorescent, and electrochemical methods have already been adopted to fabricate miniaturized portable devices for heavy metal detections [15]. Among them, electrochemical method has attracted intensive attention due to its capability for achieving better quantitative results, more rapid analysis and higher sensitivity [13, 15, 16]. While for electrochemical detection of trace amounts of heavy metals, it is usually considered mandatory to modify the surface of working electrode with active electrocatalysts (receptors) which are supposed to have high collection capacity of target metal ions. This surface modification is especially of importance for the miniaturized devices, because of the small amount of analyte (typically within 100 μL) to be used for the analysis. Following this line of reasoning, a wide range of organic and inorganic materials have been used to modify working electrode for electrochemical detection of trace heavy metals. In early times, hanging mercury drop electrodes and electrode modified with a mercury film were commonly used for heavy metal detection, because of the capability of mercury for forming amalgam with heavy metal ions, which results in its high sensitivity and good reproducibility [15, 17-19]. However, the well-known toxicity of mercury limits the development of mercury electrode sensor [20]. Later on, bismuth has been introduced as an alternative surface modifier due to its unique behaviour to form multi-component Bi alloys with numerous heavy metals and less toxicity compared with mercury [21-27]. Detection by bismuth-modified electrodes are usually carried out by simultaneous electro-reduction of Bi ions and heavy metal ions onto carbon-based solid electrodes (e.g., glass carbon [28-30], carbon nanofibers/nanotubes [21, 28, 31-33], graphite [7, 34-36], graphene [13, 37, 38], carbon paste/ink [23, 25, 39, 40]). The pre-reduced Bi could promote the deposition of heavy metal ions from analytes by forming “fuse alloys”, which is analogous to the amalgam mercury forms [21, 26, 27]. However, Bismuth-modified electrode usually needs to be activated using a tedious pretreatment to improve the sensing reproducibility and is not applicable for some in situ and online trace metal measurement in natural or bio-environment because it introduces Bi ions additionally [9, 41]. Besides, Bi ions are easy to hydrolyze to form insoluble compound in aqueous solution [21, 42]. For this reason, pH of the sample

media should be controlled below 5 to avoid hydrolysis of Bi ions, which makes this method unpractical for biological and clinical analysis [9, 21]. In recent years, a great variety of innovative nanomaterials such as metal (Au, Ag, Pd) nanoparticles [5, 43, 44], carbonaceous materials (carbon nanotubes, graphene, carbon spheres) [20, 35, 37], biological materials (DNA, protein/enzyme) [45, 46] have been tested as surface modifier for electrochemical detection of heavy metal ions. Considering the tedious synthesis procedure and relatively high cost of these materials, using these innovative nanomaterials could be a big burden in mass production of electrochemical sensors and prohibit cost effectiveness.

Carbon-based materials including bare glassy carbon electrode in principle can also be directly used for heavy metal detection. Hashemi et al. also demonstrated that surface modifier free carbon fiber micro-electrode in combination HPLC unit can be employed for copper ion detection [47, 48]. In the current work, we are intending to directly use the inexpensive graphite foil without any surface modifier for electrochemical detection of heavy metal ions in water, and graphite foils were chosen because of their excellence in both chemical stability and electrical conductivity. However, the challenge lies in two aspects: 1) How to achieve low limit of detection (e.g., drinking water standards established by WHO or US-EPA) by directly using graphite foils without any surface modifier; and 2) How to transfer the sensing performance to a miniaturized device. Herein, these challenges are overcome by integrating a microfluidic paper channel into the miniaturized carbon-based sensor (μCS), where the pristine graphite foils were used as working, pseudo-reference and counter electrodes. The microfluidic channel continuously and efficiently delivers the aqueous analyte to the detection sites to enable a shortening of the overall current response time. Moreover, the μCS possess a novel 3D structure with working and reference electrodes directly facing each other but separated by the microfluidic paper channel, as shown schematically in **Figure 4.1**. This configuration brings the working electrode in close proximity to the counter electrode, and the resulting more homogeneous and efficient electric field is supposed to facilitate the reductive deposition of metal ion on the graphite foil working electrode [49]. The sensing performance of the μCS built solely from paper and graphite foil as benign and inexpensive materials is evaluated by detecting heavy metal Cd^{2+} and $Pb^{2+,}$ which are common pollutants in the environment. It is found that impressive low detection limits of 1.2 μg/L for Cd^{2+} and 1.8 μg/L for Pb^{2+} can be achieved on the μCS. The μCS also exhibits stable sensing performance up to 10 repetitive measurements, demonstrating the unprecedented

robustness of a sensing device for heavy metal detections. We also successfully demonstrate that even for a miniaturized device, a proper design in the device configuration can completely eliminate the necessity to modify the working electrode by using additional surface modifier such as mercury, or bismuth. We believe these findings would have significant implications in developing other fast and cost-effective detection platforms, such as clinical diagnosis and security inspection.

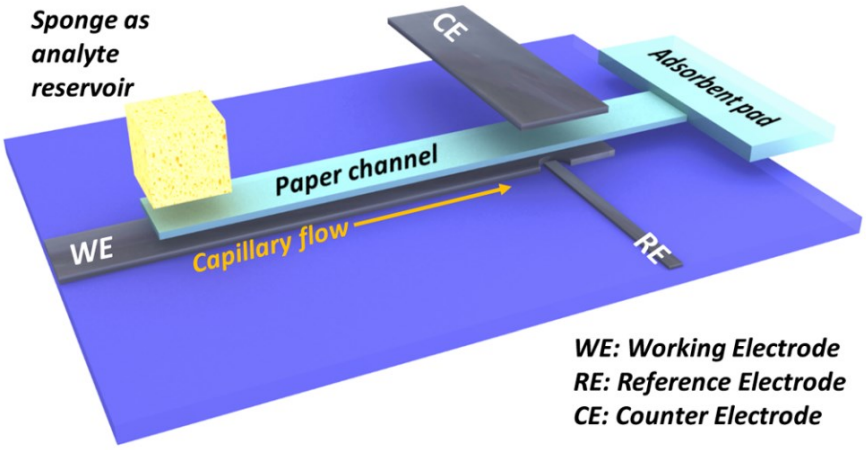

Figure 4.1 Scheme for the μCS device based on paper (light blue) and graphite foil (black).

4.2 Experimental section

Materials and chemicals. Cadmium chloride (Sigma-Aldrich), lead nitrate (Sigma-Aldrich), sodium acetate (Sigma-Aldrich), acetate acid glacial (VWR) and ethanol (VWR) were all analytical grades regents and used as received. Graphite foil was purchased from Sigraflex. Filter paper (pore size: 12-15 μm; thickness: 305 μm) was purchased from VWR. All the solutions were prepared by using double-distilled water.

Device fabrication. Three electrode configuration was employed to construct the sensing devices. A piece of graphite foil with thickness of 0.5 mm was first cleaned by ethanol and deionized water under ultrasonication, followed by being cut into certain shapes as working electrode (WE), counter electrode (CE) and pseudo-reference electrode (RE), respectively. Cleaning protocols for all the other components, i.e., PMMA substrate, sampling sponge were also critically applied by using ethanol and deionized water under ultrasonication before fabricating each μCS device in order to prevent any contaminations. The design and dimensions are detailed in **Figure S4.1**. A piece of microfluidic paper was sandwiched

between the CE and WE, while the RE will be placed adjacent to the RE to reduce the ohmic resistance. To complete the device, the electrodes was taped onto a PMMA substrate for easy operation, as shown in **Figure 4.1**. A piece of sponge, placed on one end of the paper channel, was used as analyte reservoir, which contains 2 mL (initial volume) of analyte solution and can constantly feed the analyte solution in 15 min. During the measurement, a glass vial was used to cover the sampling sponge to prevent the solvent evaporation or concentration change of an analyte. An absorbent pad cut in pieces is located at the other end of the paper channel. The function of the absorbent pad is to wick the fluid through the paper channel, create a quasi-steady flow of analyte within the paper channel and accumulate the amount of analyte flowing through the detection sites. For preparation of the Bi-modified WE, the catalyst suspension ink was firstly prepared by dispersing 5 mg of Bi_2O_3 and 15 mg of carbon black (Vulcan XC-72) together with 0.5 mL of 20 wt% Nafion in 1.5 mL of ethanol solution. The modified electrode was then prepared by applying 5 μL of above ink solution onto graphite foils covering an area of 0.5 × 0.5 mm, which is comparable to the effective surface area of WE in a modifier free μCS device (as detailed in the Supporting Information). The function of carbon black is to better disperse the Bi species and also improve the electric conductivity within the catalyst layer.

Electrochemical measurements. Electrochemical measurements were carried out on PARSTAT Multichannel-1000 (AMETEK) controlled by the Versastudio software. The SWASV measurements were conducted at room temperature, and no deaeration was performed to the supporting electrolyte (0.1 M acetate buffer solution). Heavy metal concentrations were evaluated by using square wave anodic stripping voltammetry (SWASV). The SWASV experiments comprise an electrochemical deposition step and a square wave anodic stripping voltammetry scan. The SWASV was performed using following conditions: pulse height 25 mV, step height 10 mV, frequency 25 Hz. The calibration plots were generated by conducting four independent measurement using four μCS devices. On each device, the measurements were conducted with one standard solution after the other, starting from the lowest to highest concentration. In total four sets of data were obtained, which are later used to generate the error bars (defined as the relative standard deviation) for each concentration.

Structural analysis. Raman spectra were recorded with a Bruker Senterra Raman microscope spectrometer with 532 nm excitation (laser power: 0.5 mW) with a 3 cm^{-1} resolution, and were captured from three different points for each sample. The morphology of graphite foils was investigated by using Scanning Electron Microscopy (Philips XL30 FEG) operated at an accelerating voltage of 30 kV.

4.3 Results and Discussion

4.3.1 Optimization of square wave voltammetry parameters

To evaluate the sensing performance of the as-prepared μCS devices for heavy metal detections, square wave anodic stripping voltammetry (SWASV) measurements, which is well-known for its high sensitivity, were carried out for detections of Cd^{2+} and Pb^{2+}. In order to realize a sensitive measurement, the experiment parameters including electrodeposition potential, deposition time and electrolyte pH, which were considered as the most important influential factors in SWASV were optimized, and the results are shown in **Figure 4.2**. The effect of electrodeposition potential was investigated by studying the anodic stripping peak current of 100 μg/L Cd^{2+} and 100 μg/L Pb^{2+} in 0.1 M acetate buffer solution (pH = 4.6) while varying the electrode potentials (**Figure 4.2a**). Firstly, it can be observed that Cd^{2+} requires a more negative potential (−1.1 V) to be deposited on the graphite foil electrode than Pb^{2+} (−0.9 V), which is not surprising considering their difference in standard reduction potentials. In principle, lower deposition potential could be more efficient to promote the reductive deposition of metal ions on the WEs. Interestingly, the peak currents for both metals exhibit a volcano dependence on the applied potentials with the maximum current obtained at potentials of −1.2 and −1.1 V for Cd^{2+} and Pb^{2+}, respectively, which were later chosen as the deposition potential for SWASV measurements. The decrease of the peak current at relatively lower deposition potential is caused by the competing hydrogen evolution reaction ($H^+ + e^- \rightarrow H_2$) [50], where hydrogen gas bubbles can be clearly observed on the surface of WE at low deposition potential. The effect of deposition time was investigated by varying the deposition time in the range of 1 to 10 min for Cd^{2+} and from 1 to 15 min for Pb^{2+} (**Figure 4.2b**). Although longer deposition time always leads to higher current intensity, it could lower the upper range of heavy metal detection due to the fast surface saturation in higher ion concentration. Herein, the deposition time was fixed at 1 and 3 min for detecting of Cd^{2+} and Pb^{2+}, respectively, as the trade-off between fast analysis and significant current response.

Shorter deposition time was chosen for Cd^{2+} is simply because a good linear calibration plot has already been obtained with a shorter time. As shown in **Figure 4.2b**, the proportional increase in the peak current with increasing the deposition time from 7 to 10 min indicates that the electrode surface is still far from being saturated. It is therefore possible to further improve the detection sensitivity by increasing the deposition time. The effect of electrolyte pH was studied by varying the pH values of acetate buffer solution from 3.0 to 6.0 (**Figure 4.2c**). It turns out that the square wave stripping peak current was increasing rapidly with the increase of the pH values from 3.0 to 4.6, while further increasing pH to 6.0 has imposed minor influence on the peak currents for Cd^{2+} and Pb^{2+} detection. In contrast, it is well documented that the stripping current on Bi-modified electrode would decrease with increasing the pH values [50, 51]. These result demonstrate that the detection performance of the μCS would be compromised for the sample with low pH values (≤ 4.0), which is also the case for the modified electrodes [50-53]. Therefore, for analyte with low pH values (e.g., acidified water samples with pH < 2), we cannot expect the modifier free μCS to exhibit superior sensing performance with respect to the conventional modified electrodes. However, for the samples with relatively high pH values, the μCS does show better tolerance on the pH values of the water samples. As the maximum stripping current can be obtained at pH = 4.6, the acetate buffer solution with pH at 4.6 was therefore used in subsequent experiments.

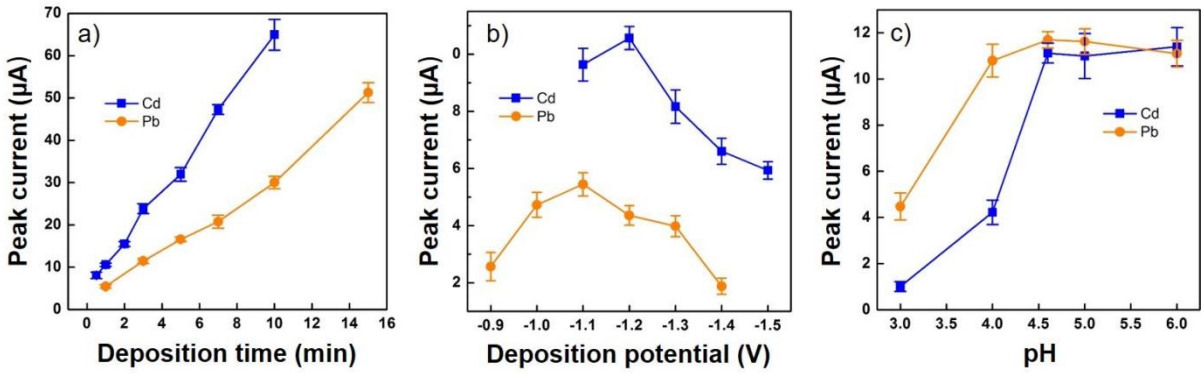

Figure 4.2 Effect of deposition potential (a), deposition time (b) and electrolyte pH (c) on Cd^{2+} and Pb^{2+} detection. The concentration of Cd^{2+} and Pb^{2+} is 100 μg/L.

As the sensing performance of a microfluidic device is also sensitive to the flow rate of an analyte to the detection sites, herein we also made attempt to evaluate the average flow rate of analytes within the paper channel. A typical capillary flow follows the Lucas-Washburn equation, which predicts that the flow rate decreases with increasing time. While it has been

experimentally demonstrated that, the capillary flow behaviour would significantly deviate from the Lucas-Washburn equation in presence of an absorbent pad, and in this case the capillary flow is sustained over time (quasi-stationary flow with time) because the liquid in the microfluidic channel would encounter a continuous increase in unwetted pore volume as it advanced in the porous absorbent pad. The constant cross-section assumed by the Lucas-Washburn equation does not apply anymore [54]. Similarly, in the current work, due to the presence of an absorbent pad at the end of the paper channel, we found that the stripping peak current was rather constant over 15 min measurement time. This implies that the flow rate of analyte within paper channel is not diminishing significantly over time and thus allows us to estimate average flow rate of analyte by quantifying the mass (volume) of solution within the sampling sponge before and after the measurement over 15 min. The average flow rate or consumption rate of an aqueous analyte is estimated to be 130 µL/min. The sampling volume for a single detection are ca. 130 and 390 µL for Cd^{2+} and Pb^{2+}, respectively, which appears to be sufficient to get well resolved stripping signals.

4.3.2 Individual detection of Cd^{2+} and Pb^{2+}

After optimizing the square wave voltammetry parameters, the µCS was applied in individual detection of Cd^{2+} and Pb^{2+} in acetate buffer solution. Typical square wave voltammograms in presence of Cd^{2+} and Pb^{2+} with different concentrations are displayed in **Figure 4.3**. Well defined anodic stripping peaks centering at −0.78 and −0.52 V (vs. carbon pseudo-reference electrode) were obtained for Cd^{2+} and Pb^{2+}, respectively. The peak currents of both Cd^{2+} and Pb^{2+} increase linearly with concentration from 5 to 100 µg/L (**Figure 4.3b, d**). However, peak broadening occurs at analyte concentration below 10 µg/L for both Cd^{2+} and Pb^{2+}, which might stem from the heterogeneity of surface active sites on the surface of graphite foils and associated varied interactions with the deposited metal particles. This might also lead to the loss of linear response of SWASV signals at lower analyte concentrations ($<$ 5 µg/L) by using the µCS. For instance, it is difficult for us to discriminate the analytes with Cd^{2+} concentrations between 1 to 2 ppb by comparing their SWASV signals, though their stripping peaks are still well resolved. Attempt were also made to study the upper limit of the linear range for both metals. As shown in **Figure S4.2**, the linear range for Cd^{2+} can be extended up to at least 500 µg/L. In contrast, we found that the although the peak current response for Pb^{2+} would still get increased with the concentration, however, deviate from the linear calibration

plot obtained at concentration range from 5 to 100 µg/L, which would stem from saturation of surface sites for metal ions with higher concentrations. The calibration plots and correlation coefficients are shown in **Figure 4.3 b, d** (x: concentration/µg/L, y: current/µA). The limit of detection for Cd^{2+} and Pb^{2+} are 1.2 and 1.8 µg/L based on 3σ method (detailed in the Supporting Information), respectively, which are below the allowable limits in drinking water proposed by US-EPA (Cd: 5 µg/L, Pb: 15 µg/L) and WHO (Cd: 3 µg/L, Pb: 10 µg/L) [55, 56]. Specifically, in the case of Cd^{2+} detection, the µCS device is not only capable for quantifying Cd^{2+} in water samples with ion concentration above the US-EPA allowable limits (5 µg/L), but also capable to raise an alert for the water sample that contains ions with concentration below the allowable limit. Moreover, the impressive low detection limits and wide linear detection range achieved by using the µCS for both analytes also indicate that the potential selective absorption of Cd^{2+} or Pb^{2+} by the sensor components, i.e., paper, graphite foil or sampling sponge, plays a minor role in the electrochemical sensing on the µCS, at least for analytes with concentration above the lower limit of linear detection range. This is consistent with the finding reported by Pickering, that the presence of competing electrolyte could significantly reduce the absorption/uptake of heavy metal ions (e.g., Pb^{2+}, Cd^{2+}) by filter paper [57]. It is proposed that absorption of metal ions (Pb^{2+}, Cd^{2+} etc.) by filter paper may be attributed to an ion exchange process, while abundant cations in the electrolyte would suppress this exchange process due to the preferential retention of cations in the electrolyte [57]. The capability and performance of µCS are also compared with some modified electrodes, screen printing electrodes and miniaturized sensors in recent literatures in **Table 4.1**. Apart from using miniaturized sensors, electrochemical sensing measurement can also be conducted by using the bulk electrochemical cell configuration, where a surface modified glassy carbon electrode, as the WE, is placed in excess amount of electrolyte with analyte (e.g., 100 mL). The bulk electrochemical cell configuration usually gives lower detection limit compared with those miniaturized sensors because of the significantly much larger amount of analyte being used during the sensing process. It can be seen that the µCS devices exhibits almost comparable sensing performance to some state-of-the-art surface modified electrodes in bulk electrochemical cell configuration, and is also among the best miniaturized on-chip sensing devices in terms of detection limit and sensitivity. To be noted, for practical application, usually an analyte solution with big collection volume (e.g., 100 mL) is provided, and the small analyte volume required by using these µCS devices for a single analysis would

enable strict replicate analysis and allow to achieve even lower detection limit by concentrating the analyte solution.

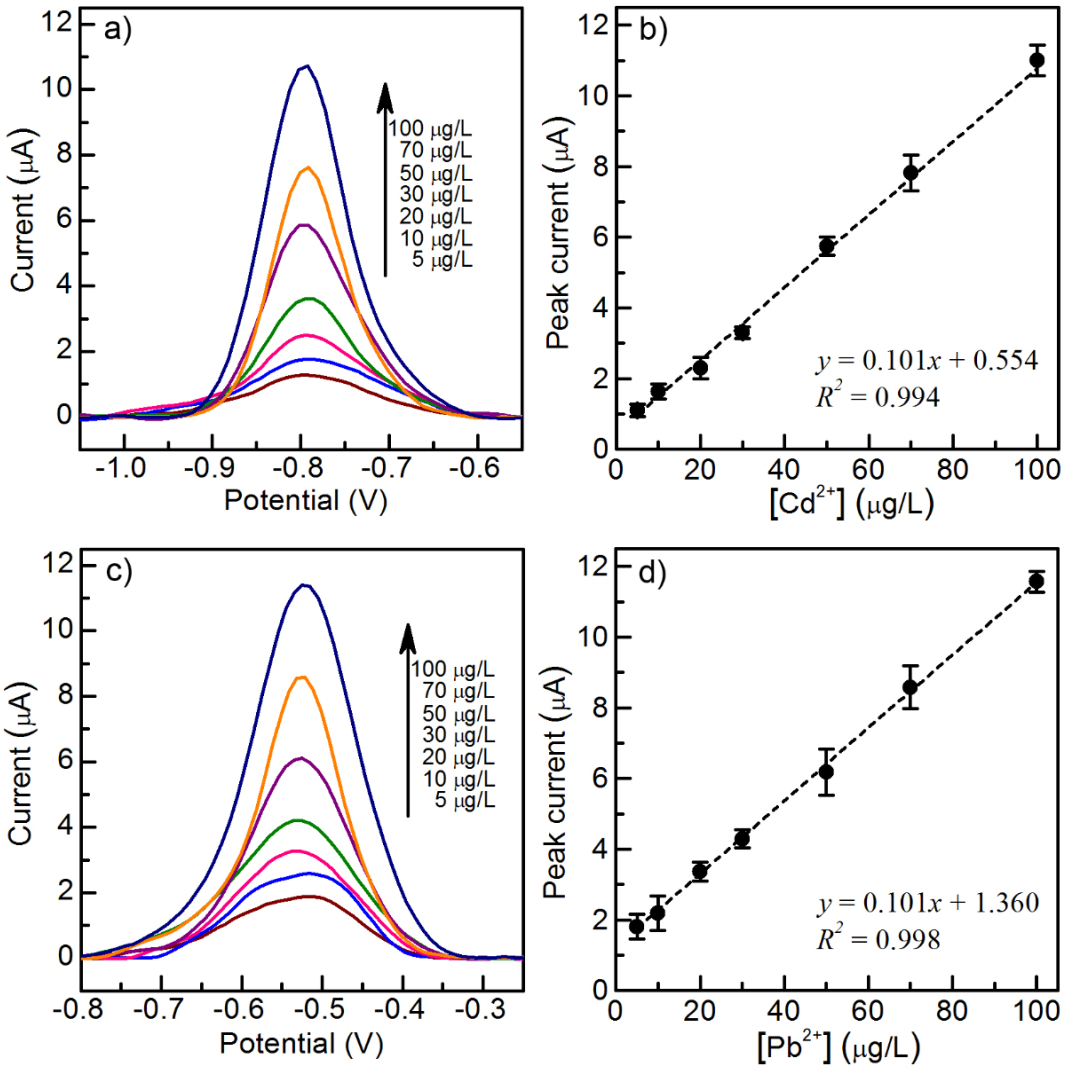

Figure 4.3 Square wave voltammograms for Cd^{2+} (a) and Pb^{2+} (c) in 0.1 M acetate buffer (pH = 4.6) on μCS. Linear correction from 5 to 100 μg/L for Cd^{2+} (b) and Pb^{2+} (d).

Compared to these sensing platform where relatively expensive (Pd, Ag, CNF) or other heavy metal (Bi/Bi_2O_3) surface modifiers have to be used, here in the current work, only inexpensive and environmental friendly materials (cellulose paper, graphite foil) was used to fabricate the μCS devices. The low cost and environmental friendly nature make these μCS devices entirely disposable without causing additional pollution to the environment, thus holding great application prospect in future point-of-care analysis of heavy metal ions.

Table 4.1 Performance of various sensing devices for heavy metal detection.

Sensor or electrode	Modifier	Method	Deposition time (s)	Linear range (µg/L)		Detection of limit (µg/L)		Sensitivity[a] (µA (µg/L)$^{-1}$)		Ref.
				Cd^{2+}	Pb^{2+}	Cd^{2+}	Pb^{2+}	Cd^{2+}	Pb^{2+}	
Electrospun CNF modified GCE	CNF	SWV	300	46-182	27-145	0.17	0.19	0.107	0.25	[20]
CNF array modified GCE	CNF array	SWV	120	–	10-100	–	0.4	–	0.04	[58]
Pd NPs / porous activated carbon modified GCE	Pd/C	DPV	not mentioned	56-1440	104-4640	4.6	10.4	–	–	[43]
Porous bismuth-carbon nanocomposites electrode	Bi	SWV	300	1-100	1-100	0.6	0.6	0.2	0.15	[59]
Bismuth bulk electrode	Bi	SWV	180	10-100	10-100	0.54	0.93	0.112	0.125	[60]
Bismuth citrate modified SPE	Bi	DPV	120	5-40	10-80	1.1	0.9	0.028	0.04	[61]
Bismuth coated microband SPE	Bi	SWV	120	5-45	–	1.3	–	0.01	–	[62]
Bi nanoparticle porous carbon composite SPE	Bi	SWV	120	5-100	5-100	2.1	3.9	0.024	0.025	[63]
Disposable Bi_2O_3 SPE	Bi_2O_3	SWV	120	10-150	10-150	5	10	0.013	0.0085	[64]
On-chip sensor with silver electrode	Ag	SWV	300	–	1-1000	–	0.55	–	0.028	[65]
Bismuth Screen printing microfluidic sensor	Bi	SWV	120	–	5-100	–	1	–	0.17	[16]
MWCNT and graphite powder modified screen printing sensor	MWCNTs	SWV	240	5-150	5-150	1	1	0.0066	0.0068	[66]
Bi_2O_3 modified screen printing sensor	Bi_2O_3	SWV	300	20-100	20-100	1.5	2.3	0.065	0.0022	[67]
Screen printing (Graphite ink) microfluidic sensor	Graphite ink	SWV	120	10-100	10-100	11	7	0.015	0.0025	[8]
On-chip microfluidic channel sensor using Bi electrode	Bi	SWV	Cd: 90 Pb: 60	28-280	25-400	9.3	8	0.065	0.0022	[9]
Microfluidic carbon based sensor (µCS)	None	SWV	Cd: 60 Pb: 180	5-500	5-100	1.2 (6)[b]	1.8 (6)[b]	0.101	0.101	this work

CNF: carbon nanofiber; GCE: glass carbon electrode; SPE: screen printing electrode; MWCNT: multiwall carbon nanotube; SWV: square wave voltammetry; DPV: differential pulse voltammetry.

[a]The sensing sensitivity is expressed as the slope of the calibration plot.

[b]Detection limit in the simultaneous detection of Cd^{2+} and Pb^{2+}.

4.3.3 Simultaneous detection of Cd^{2+} and Pb^{2+}

The performance of the µCS for simultaneous detection of Cd^{2+} and Pb^{2+} was also evaluated. The measurements were carried out in 0.1 M acetate buffer solution (pH = 4.6) contained Cd^{2+} and Pb^{2+} by firstly holding the deposition potential at −1.2 V and then square wave anodic stripping. The reductive deposition time is fixed at 3 min for simultaneous detection of both metals, in order to ensure that SWASV signal for Pb is strong enough for quantification analysis. As shown in **Figure 4.4a**, stripping peaks for Cd and Pb slightly overlap with each other and detection limits for both ions are worse than their corresponding individual

detection. Similar peak intensity is obtained for Pb by comparing with the individual Pb detection. However, the peak intensity of Cd decreased in comparison with the individual analysis. This phenomenon may arise from the competitive adsorption of Cd^{2+} and Pb^{2+} on the surface of graphite foil, which leads to a reduction in the stripping peak intensity of Cd. Due to the overlap between these two stripping peaks, peak deconvolution was applied by using a Gaussian line shape, in a hope to obtain the "real" current contributed from individual metal ion. We found that calibration plots obtained on the basis of apparent or deconvoluted peak current gave quite comparable slope (0.11 for Pb; and 0.05 for Cd), and only minor differences in interception (< 0.1 µA for both metals) can be observed. Therefore, in principle both apparent or deconvoluted peak current can be used to quantify the heavy metal concentration, and for simplicity we chose to use the apparent peak current later on. The slope changes in calibration plots, shown in **Figure 4.4b**, indicate that there are some interactions between Cd^{2+} and Pb^{2+} deposition process. Nevertheless, these two ions could still be simultaneously detected within the linear range from 20 to 100 µg/L by using µCS devices, with the detection limit of 6 µg/L for both metals. It should be noted that the µCS device actually still holds the potential to exhibit further improved sensing sensitivity for simultaneous detection by simply increasing the deposition time, given that recommended deposition time is as long as 10 min for some commercial available screen printed electrodes for heavy metal detection [68].

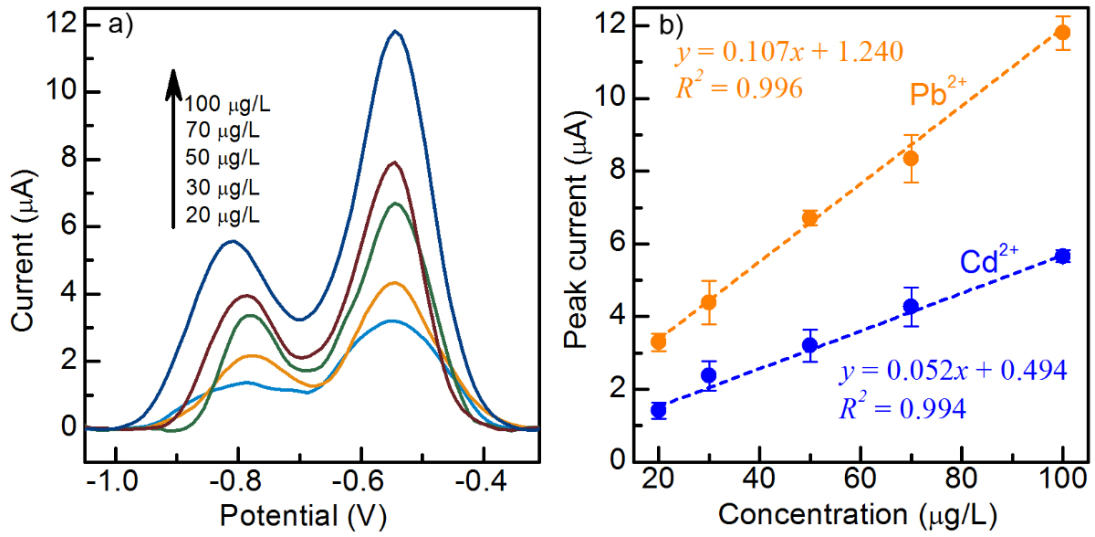

Figure 4.4 Square wave voltammograms for simultaneous detection of Cd^{2+} and Pb^{2+} in 0.1 M acetate buffer on µCS (a). Linear correction from 20 to 100 µg/L for Cd^{2+} and Pb^{2+} (b).

4.3.4 Detection of Cd^{2+} and Pb^{2+} in commercial mineral water

In order to test the sensing performance of these μCS devices under more complex conditions, attempts herein were made to use commercial mineral water, which contains Na^+ (109 mg/L), K^+ (13.3 mg/L), Mg^{2+} (28.6 mg/L), Ca^{2+} (175 mg/L), Cl^- (128 mg/L), sulfate (31 mg/L) and bicarbonate (706 mg/L) according to its specification, as a practical sample for the detection of Cd^{2+} and Pb^{2+}. Prior to the measurement, the bottled mineral water was used to prepare acetate buffer solution (0.1 M, pH = 4.6). It can be seen that no stripping peak for either Cd^{2+} or Pb^{2+} can be detected for the pristine mineral water sample (**Figure S4.3**). However, clear stripping peaks can be seen on the mineral water samples with intentionally added Cd^{2+} or Pb^{2+}. The peak intensities were increased proportionally with the concentration of both metal ions from 10 to 50 μg/L, and the calculated concentrations by using the calibration plots (**Figure 4.3b, d**) are consistent with their nominal values (i.e., 10 or 50 μg/L), as listed in **Table 4.2**. Based on these results, we can draw two conclusions that: 1) There is no or little amount (below the limit of detection) of these heavy metals in this commercial mineral water; 2) The presence of various mineral ions in the commercial mineral water imposes little effect on the sensing performance of the μCS, again demonstrating the great prospect of the μCS to be used in practical sample analysis.

Table 4.2 Determination of Cd^{2+} and Pb^{2+} in commercial mineral water by using the μCS

Sample	Actual Concentration / (μg/L)[a]		Calibrated Concentration / (μg/L)[b]	
	[Cd^{2+}]	[Pb^{2+}]	[Cd^{2+}]	[Pb^{2+}]
Mineral water	0	0	Not detected	Not detected
Mineral water-10	10	10	10.8 ± 1.1	10.6 ± 1.4
Mineral water-50	50	50	51.9 ± 2.9	50.3 ± 2.7

[a]The concentration reached by adding Cd^{2+} and Pb^{2+} into the mineral water.

[b]The concentration calculated based on the calibration plot shown in Figure 4.3b, d. At least three measurements were conducted to determine the standard deviation.

4.3.5 Influence of interfering ions on Cd^{2+} and Pb^{2+} detection

In order to test the selectivity behaviour of μCS toward Cd^{2+} and Pb^{2+} detection, Ba^{2+}, Mn^{2+}, Zn^{2+}, Fe^{2+}, Co^{2+}, Ni^{2+}, Fe^{3+} and Cu^{2+} were chosen as interfering ions. The standard reduction potential of these ions is shown in **Table 4.3**. Acetate buffer (pH = 4.6) containing 100 μg/L Cd^{2+} or Pb^{2+} together with 5 mg/L interfering ions was tested by using the μCS. In principle, ions with higher reduction potential could affect the detection of ions with lower reduction

potential. For example, the existence of Co^{2+}, Ni^{2+}, Fe^{3+} and Cu^{2+} may have influence on the electro-reduction process of Cd^{2+}. In order to investigate the influence of interfering ions on Cd^{2+} detection by using μCS, the 8 interfering ions were divided into 4 groups: 1) Ba^{2+}, Mn^{2+}, Zn^{2+}, Fe^{2+}, which have lower reduction potential than Cd^{2+}; 2) Co^{2+}, Ni^{2+}, which have similar reduction potential; 3) Fe^{3+}; and 4) Cu^{2+}. **Figure 4.5a** shows the influence of interfering ions on Cd^{2+} detection, which clearly shows that Ba^{2+}, Mn^{2+}, Zn^{2+}, Fe^{2+}, Co^{2+}, Ni^{2+} and Fe^{3+} do not have much influence on Cd^{2+} detection, even their concentration is 50 fold higher than Cd^{2+}. While Cu^{2+} has an impact on Cd^{2+} detection maybe because of its oxidation property. For real applications, thus it becomes necessary to choose the appropriate calibration plot according to the absence/presence of the stripping peak characteristic of the interfering ion as Cu^{2+}. Similar results could be obtained on Pd^{2+} detection against interfering ions, as shown in **Figure 4.5b**.

Table 4.3 Standard reduction potential of Cd^{2+}, Pb^{2+} and interfering ions [69].

Half reaction	Standard reduction potential (V)
$Cu^{2+} + 2e^- \rightarrow Cu$	0.337
$Fe^{3+} + 3e^- \rightarrow Fe$	-0.04
$Pb^{2+} + 2e^- \rightarrow Pb$	-0.13
$Ni^{2+} + 2e^- \rightarrow Ni$	-0.25
$Co^{2+} + 2e^- \rightarrow Co$	-0.28
$Cd^{2+} + 2e^- \rightarrow Cd$	-0.40
$Fe^{2+} + 2e^- \rightarrow Fe$	-0.44
$Zn^{2+} + 2e^- \rightarrow Zn$	-0.76
$Mn^{2+} + 2e^- \rightarrow Mn$	-1.18
$Ba^{2+} + 2e^- \rightarrow Ba$	-2.91

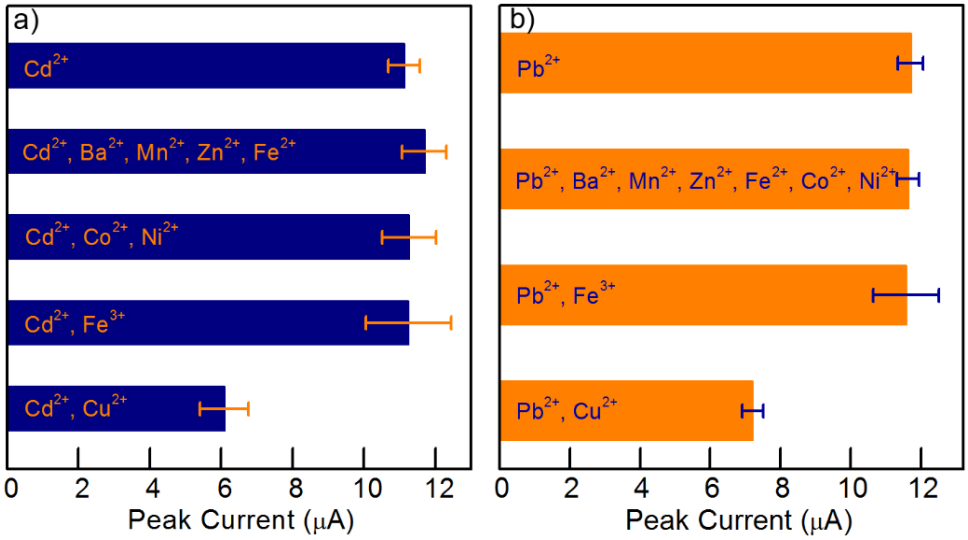

Figure 4.5 Influence of interfering ions on Cd^{2+} (a) and Pb^{2+} (b) detection. The concentration of Cd^{2+} and Pb^{2+} was 100 µg/L. The concentration of each interfering ions was controlled at 5 mg/L.

4.3.6 Influence of 3D configuration and paper channel

To study the influence of the newly introduced 3D sandwich configuration, a sensor with a 2D configuration was prepared. Similar to the design of some commercial screen printed electrochemical sensors, 3 electrodes are parallel to each other and lie in the same horizontal plane, while the microfluidic channel is placed across the three electrodes (as illustrated in **Figure S4.4**). However, in contrast to the 3D configuration the 2D one always lead to rather small current signal and can hardly be used to detect any trace amount of heavy metals (**Figure S4.4**). The poor performance of the 2D structured µCS would originate from the small amount of analyte solution being used for the analysis and relatively long distance between electrodes, which would cause significant resistance between WE and RE (solution resistance) and the inefficient electric field between WE and CE for metal ion migration and deposition. This drawback seems to be overcome by the 3D configuration, where WE and CE facing each other and electrolyte going along the microfluidic channel between these two electrodes.

We also made attempts to study the exact role of the paper channel in the µCS device. To achieve this, a drop of analyte (200 µL) was added to gap between the working electrode and reference electrode. This droplet stays well between these two electrodes because of the large surface tension of water on the graphite foil. However, detection of 100 µg/L Cd^{2+} over this

stagnant-analyte-design sensor gives weak stripping peak intensity (4 μA), which is much lower than the value obtained in microfluidic configuration (**Figure S4.5**). After introducing paper channel into the sensor, which change the stagnant analyte into fluidic one, the SWV signal increased from 4.0 to 11.5 μA, as shown in **Figure S4.5**. Therefore, besides 3D structure, the paper channel is another key point in the sensor design.

4.3.7 Stability and reproducibility of the μCS

The reusability is a highly desirable feature for a sensing device, which might result in significant cost and waste reduction during the field analysis. For this reason, the electrochemical stability/reusability of the μCS was studied by subjecting a single μCS device to 10 repetitive SWASV measurements for detecting Cd^{2+} and Pb^{2+} with concentration of 50 and 100 μg/L, and the current response is plotted against the cycle number, as shown in **Figure 4.6**. Three sensors are studied in each stability test. It can be seen that the anodic stripping current shows negligible drop after 10 times repetitive measurements regardless of the type/concentration of metal ions, demonstrating the great robustness of these μCS devices for heavy metal detections. Specifically, the signal drops by 6% and 9% for 50 and 100 μg/L Cd detection, respectively. The signal drops by 6% and 13% for 50 and 100 μg/L Pb detection, respectively. After 10 repetitive measurements, the stripping current would gradually decrease with further increasing the cycle numbers, which is stemming from the depletion of the analyte within the sampling sponge. Considering that for practical application, it is less likely to frequently reuse these portable devices due to its low cost and possible cross-contamination from different samples, no further attempt was made to increase the cycle number by refilling the sampling sponge. In addition to the superior stability of a single device, the good reproducibility of the μCS has already been reflected by the small relative standard deviation ($< 5\%$) over at least four independent measurements (**Figure 4.3**). Attempt was also made to investigate the electrochemical sensing capability of a Bi-modified electrode (denoted as Bi-WE, WE modified with a mixture ink of Bi_2O_3 powder and carbon black). Firstly, we investigated the effect of loading amount of Bi_2O_3 within the electrocatalysts on the electrochemical sensing performance by varying the loading from 2 wt% to 50 wt%, and found the highest stripping peak current can be obtained at the loading around 25 wt%, which was later used for further investigation. Surprisingly it was found that the current response differs significantly from one electrode to another, and is highly sensitive

to the exposure time of the Bi-WE in the air (**Figure S4.7**). Firstly, it can be seen from **Figure 4.6c** that the stripping peak current on fresh Bi-WE is actually ca. 25% higher than that on the modifier free µCS, demonstrating that in principle Bi-modified electrode could exhibit higher sensitivity for Cd detection. Secondly, the SWASV signal decreases by 43% relative to its initial value after exposing the Bi-WE in air for only 5 min, and it is further decreased by over 67% when the air exposure time is expanded to 30 min. Although the deactivation mechanism of the Bi-WE is still not fully understood, it can be seen that the ill-defined initial status of the Bi-WE would lead to scattered current response in electrochemical sensing measurement. In contrast, the sensing performance is rather consistent over different graphite foil WEs free from any surface modifiers (**Figure 4.6c**). We believe that these results echo the importance of elimination of surface modifier in developing high performing sensing platform with superior stability and reproducibility.

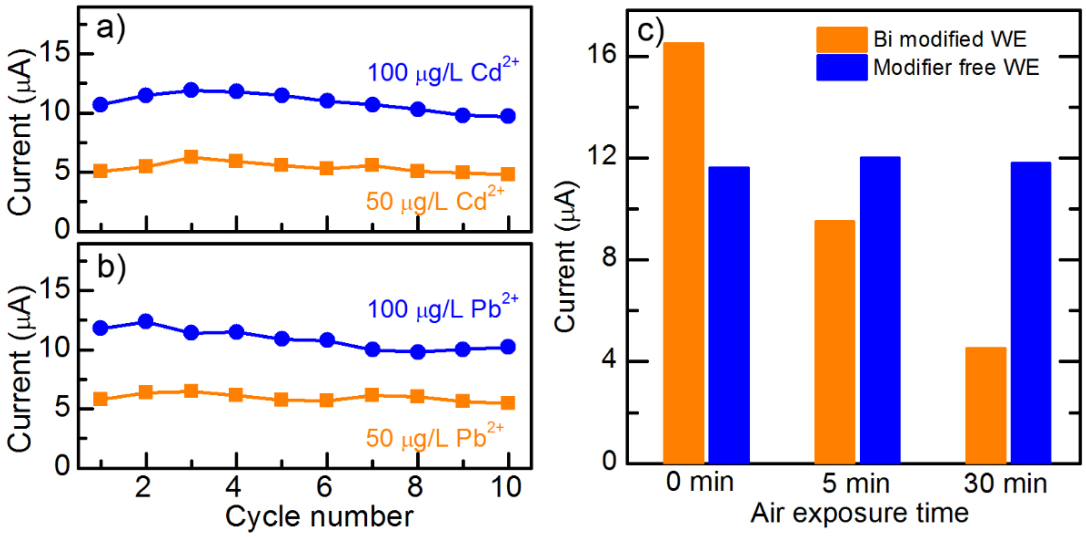

Figure 4.6 Stability measurement under concentration of 50 and 100 µg/L of Cd^{2+} (a) and Pb^{2+} (b). Sensing performance of graphite foil WEs with and without Bi_2O_3 modification for Cd^{2+} detection after being exposed in air for a certain time (c).

4.3.8 Structural analysis of the graphite foil

To probe the possible structural change of the graphite foil, Raman spectra were captured on the graphite foils before and after the electrochemical measurements. As shown in **Figure 4.7**, three characteristic peaks at 1350 cm, 1580 cm and 2716 cm can be clearly resolved, which refer to disordered carbon structure (D-band), graphite structure (G-band) and second-order double-resonant scattering in graphite (G'-band), respectively. The identical Raman spectra

recorded on these two sample indicate that graphite foil is rather robust during the electrochemistry measurement. Specifically, the intensity ration of the D band and G band (ID/IR), which is usually taken as an indicator of the graphitization degree for a carbon sample, is also comparable (0.04) on the graphite foils with and without experiencing the electrochemical measurements. These results confirm that the graphite foil has a high graphitization degree, and is chemically stable during the electrochemistry measurement, which could rationalize the aforementioned well reproducible performance of the μCS device in the repetitive heavy metal sensing.

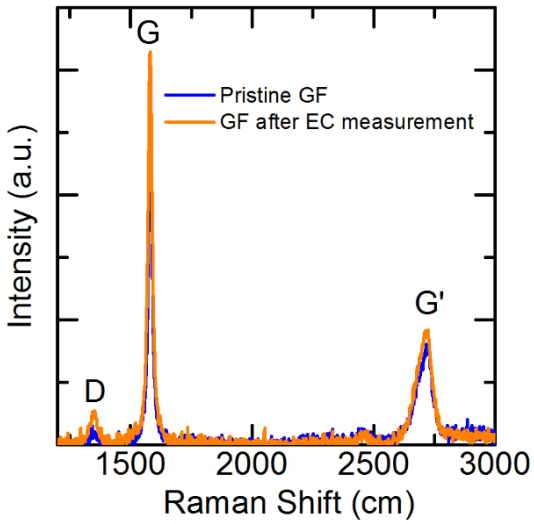

Figure 4.7 Raman spectrum for graphite foil (GF) before and after electrochemical measurements.

We have demonstrated that the modifier-free graphite foil is capable for heavy metal detection with high sensitivity, low detection limit and wide linear calibration region. While as it is still not well understood why the inherently less active pristine carbon, i.e., graphite foil, could provide sufficient sites for the pre-concentration of metal ions. To explore the nature of active sites for electrodeposition of metal ions on the graphite foil, we conducted SEM analysis on the graphite foils before and after electrodeposition of Cd^{2+}. As shown in **Figure 4.8a**, firstly it can be seen that the surface of graphite foils consisting of interconnected flakes. After electrodepositing of Cd^{2+}, sphere-like particles (Cd or CdO) can be clearly seen on the surface of graphite flakes (**Figure 4.8b**). Interestingly, it can be found that majority of the particles are selectively located at the edge position of the graphite flakes, as illustrated by the marked squares in **Figure 4.8b**. These results demonstrate that edge surface positions of graphite

flakes, where the carbon atoms have lower coordination number, could be more active to catalyze the electrodeposition of metal ions, and provide the basis for graphite foils to be directly used as WE for heavy metal detection. This phenomenon is actually not surprising, considering that it has been well documented that electrochemical reaction at graphite edge sites is preferential as the kinetics of bond formation at basal plane sites is much slower than at edge/defect sites [70]. Nevertheless, as shown previously, the properly designed sensor configuration is also a necessity for achieving high sensing performance of these μCS devices.

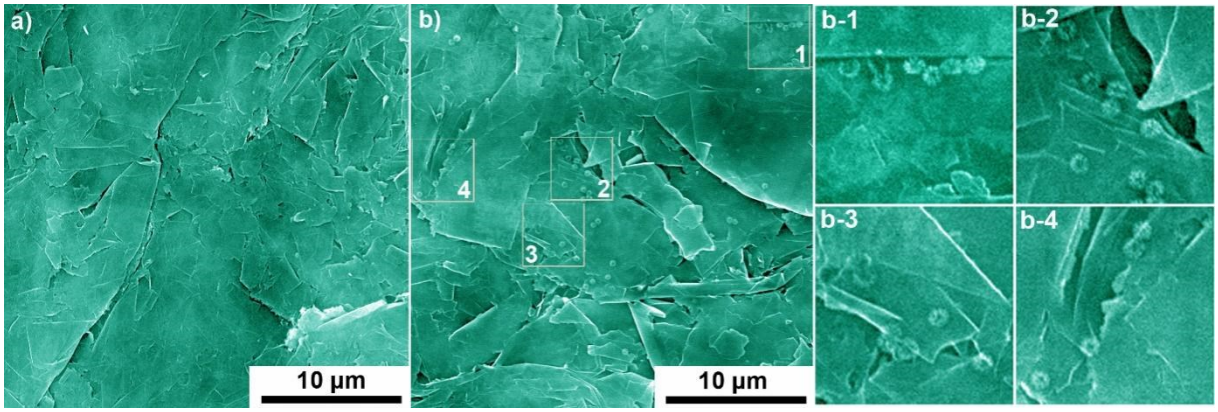

Figure 4.8 Representative SEM images of pristine graphite foil (a) and graphite foil after electro-reductive deposition of Cd^{2+} (b). The square areas which are magnified in b-1, b-2, b-3 and b-4 indicate that the electrodeposited Cd species are selectively located at the edge positions of graphite flakes.

4.4 Conclusion

A heavy metal electrochemical sensor assembled by using graphite foil and paper was developed, which is capable to detect heavy metal ions (Cd^{2+} and Pb^{2+}) with wide linear range and low detection limits. The sensor is modifier-free, low cost, reusable and easy to fabricate, which would benefit from the combined microfluidic configuration and novel 3D electrode layout. We also disclose that the graphite foil comprising of graphite flakes with abundant of edge sites could favour the metal deposition, thus providing a simple block material to be used in electrochemical sensors. This easy handling method could provide some new ideas for other portable electroanalytical/sensing systems.

References

[1] T. O. Llewellyn, Cadmium (materials flow), United States. Department of the Interior. Bureau of Mines, 1994.

[2] D. Gidlow, Occup. Med. 54 (2004) 76-81.

[3] M. Mejáre, L. Bülow, Trends Biotechnol. 19 (2001) 67-73.

[4] P. Lodeiro, J. Barriada, R. Herrero, M. S. De Vicente, Environ. Pollut. 142 (2006) 264-273.

[5] M. F. M. Noh, I. E. Tothill, Anal. Bioanal. Chem. 386 (2006) 2095-2106.

[6] P. Apostoli, J. Chromatogr.B 778 (2002) 63-97.

[7] R. T. Kachoosangi, C. E. Banks, X. Ji, R.G. Compton, Anal. Sci. 23 (2007) 283-289.

[8] M. Medina-Sánchez, M. Cadevall, J. Ros, A. Merkoçi, Anal. Bioanal. Chem. 407 (2015) 8445-8449.

[9] Z. Zou, A. Jang, E. MacKnight, P.-M. Wu, J. Do, P. L. Bishop, C. H. Ahn, Sens. Actuators B 134 (2008) 18-24.

[10] W. Lo, H. Chua, K.-H. Lam, S.-P. Bi, Chemosphere 39 (1999) 2723-2736.

[11] D. G. Bostwick, H. B. Burke, D. Djakiew, S. Euling, S. M. Ho, J. Landolph, H. Morrison, B. Sonawane, T. Shifflett, D. J. Waters, Cancer 101 (2004) 2371-2490.

[12] E. L. Silva, P. dos Santos Roldan, J. Hazard. Mater. 161 (2009) 142-147.

[13] J. Li, S. Guo, Y. Zhai, E. Wang, Anal. Chim. Acta 649 (2009) 196-201.

[14] A. K. Wanekaya, Analyst 136 (2011) 4383-4391.

[15] G. Aragay, J. Pons, A. Merkoçi, Chem. Rev. 111 (2011) 3433-3458.

[16] Z. Nie, C. A. Nijhuis, J. Gong, X. Chen, A. Kumachev, A.W. Martinez, M. Narovlyansky, G. M. Whitesides, Lab Chip 10 (2010) 477-483.

[17] J. W. Ross, R. D. DeMars, I. Shain, Anal. Chem. 28 (1956) 1768-1771.

[18] T. Florence, J. Electroanal. Chem. Interfacial Electrochem. 27 (1970) 273-281.

[19] H. P. Wu, Anal. Chem. 68 (1996) 1639-1645.

[20] D. Zhao, T. Wang, D. Han, C. Rusinek, A. J. Steckl, W.R. Heineman, Anal. Chem. 87 (2015) 9315-9321.

[21] S. B. Hočevar, B. Ogorevc, J. Wang, B. Pihlar, Electroanalysis 14 (2002) 1707-1712.

[22] R. O. Kadara, I. E. Tothill, Anal. Bioanal. Chem. 378 (2004) 770-775.

[23] L. Baldrianova, I. Svancara, S. Sotiropoulos, Anal. Chim. Acta 599 (2007) 249-255.

[24] C. Kokkinos, A. Economou, I. Raptis, C. E. Efstathiou, T. Speliotis, Electrochem. Commun. 9 (2007) 2795-2800.

[25] I. Švancara, L. Baldrianová, E. Tesařová, S.B. Hočevar, S.A. Elsuccary, A. Economou, S. Sotiropoulos, B. Ogorevc, K. Vytřas, Electroanalysis 18 (2006) 177-185.

[26] A. Economou, TrAC Trends Anal. Chem. 24 (2005) 334-340.

[27] J. Wang, Electroanalysis 17 (2005) 1341-1346.

[28] J. Wang, J. Lu, S. B. Hocevar, P. A. Farias, B. Ogorevc, Anal. Chem. 72 (2000) 3218-3222.

[29] J. Wang, J. Lu, Ü. A. Kirgöz, S. B. Hocevar, B. Ogorevc, Anal. Chim. Acta 434 (2001) 29-34.

[30] G. Kefala, A. Economou, A. Voulgaropoulos, M. Sofoniou, Talanta 61 (2003) 603-610.

[31] G. Liu, Y. Lin, Y. Tu, Z. Ren, Analyst 130 (2005) 1098-1101.

[32] G. H. Hwang, W. K. Han, J. S. Park, S. G. Kang, Talanta 76 (2008) 301-308.

[33] H. Xu, L. Zeng, S. Xing, Y. Xian, G. Shi, L. Jin, Electroanalysis 20 (2008) 2655-2662.

[34] Ü. A. Kırgöz, S. Marín, M. Pumera, A. Merkoçi, S. Alegret, Electroanalysis 17 (2005) 881-886.

[35] G. Aragay, J. Pons, A. Merkoçi, J. Mater. Chem. 21 (2011) 4326-4331.

[36] R. Nasraoui, D. Floner, F. Geneste, Journal of Electroanal. Chem. 629 (2009) 30-34.

[37] J. Li, S. Guo, Y. Zhai, E. Wang, Electrochem. Commun. 11 (2009) 1085-1088.

[38] Y. Teng, T. Chen, F. Xu, W. Zhao, W. Liu, Int. J. Electrochem. Sci. 11 (2016) 1907-1917.

[39] J. Wang, J. Lu, S. B. Hocevar, B. Ogorevc, Electroanalysis 13 (2001) 13-16.

[40] A. Królicka, R. Pauliukait, I. Švancara, R. Metelka, A. Bobrowski, E. Norkus, K. Kalcher, K. Vytřas, Electrochem. Commun. 4 (2002) 193-196.

[41] R. Pauliukaitė, S. B. Hočevar, B. Ogorevc, J. Wang, Electroanalysis 16 (2004) 719-723.

[42] M. Bučková, P. Gründler, G.U. Flechsig, Electroanalysis 17 (2005) 440-444.

[43] P. Veerakumar, V. Veeramani, S.-M. Chen, R. Madhu, S.-B. Liu, ACS Appl. Mater Interfaces 8 (2016) 1319-1326.

[44] S. Prakash, V. K. Shahi, Anal. Methods 3 (2011) 2134-2139.

[45] L. Shen, Z. Chen, Y. Li, S. He, S. Xie, X. Xu, Z. Liang, X. Meng, Q. Li, Z. Zhu, Anal. Chem. 80 (2008) 6323-6328.

[46] Y. Xiao, A. A. Rowe, K. W. Plaxco, J. Am. Chem. Soc. 129 (2007) 262-263.

[47] P. Pathirathna, Y. Yang, K. Forzley, S. P. McElmurry, P. Hashemi, Anal. Chem. 84 (2012) 6298-6302.

[48] Y. Yang, P. Pathirathna, T. Siriwardhane, S. P. McElmurry, P. Hashemi, Anal. Chem. 85 (2013) 7535-7541.

[49] C. Winkelmann, W. Lang, Int. J. Mach. Tool. Manu. 72 (2013) 25-31.

[50] X. Xuan, M. F. Hossain, J. Y. Park, Sci. Rep. 6 (2016).

[51] J. A. Barón-Jaimez, J. L. Marulanda-Arévalo, J. J. Barba-Ortega, Dyna 81 (2014) 122-128.

[52] S. Xiong, B. Yang, D. Cai, G. Qiu, Z. Wu, Electrochim. Acta 185 (2015) 52-61.

[53] G. Zhao, H. Wang, G. Liu, Int. J. Electrochem. Sci 11 (2016) 1840-1851.

[54] S. Mendez, E. M. Fenton, G. R. Gallegos, D. N. Petsev, S. S. Sibbett, H. A. Stone, Y. Zhang, G. P. López, Langmuir 26 (2009) 1380-1385.

[55] Table of Regulated Drinking Water Contaminants. https://www.epa.gov/ground-water-and-drinking-water/table-regulated-drinking-water-contaminants (accessed Feb 28, 2017).

[56] W. H. Organization, Guidelines for drinking-water quality, Geneva: world health organization, 2011.

[57] W. Pickering, J. Chromatogr. A 4 (1960) 481-484.

[58] J. E. Robinson, W. R. Heineman, L. B. Sagle, M. Meyyappan, J. E. Koehne, Electrochem. Commun. (2016).

[59] M. Gich, C. Fernández-Sánchez, L.C. Cotet, P. Niu, A. Roig, J. Mater. Chem. A 1 (2013) 11410-11418.

[60] K. C. Armstrong, C. E. Tatum, R. N. Dansby-Sparks, J. Q. Chambers, Z.-L. Xue, Talanta 82 (2010) 675-680.

[61] N. Lezi, A. Economou, P. A. Dimovasilis, P. N. Trikalitis, M. I. Prodromidis, Anal. Chim. Acta 728 (2012) 1-8.

[62] O. Zaouak, L. Authier, C. Cugnet, A. Castetbon, M. Potin-Gautier, Electroanalysis 21 (2009) 689-695.

[63] P. Niu, C. Fernández-Sánchez, M. Gich, C. Navarro-Hernández, P. Fanjul-Bolado, A. Roig, Microchim. Acta 183 (2016) 617-623.

[64] R. O. Kadara, N. Jenkinson, C. E. Banks, Electroanalysis 21 (2009) 2410-2414.

[65] W. Jung, A. Jang, P. L. Bishop, C. H. Ahn, Sens. Actuators B 155 (2011) 145-153.

[66] P. Rattanarat, W. Dungchai, D. Cate, J. Volckens, O. Chailapakul, C. S. Henry, Anal. Chem. 86 (2014) 3555-3562.

[67] G.-H. Hwang, W.-K. Han, J.-S. Park, S.-G. Kang, Sens. Actuators B 135 (2008) 309-316.

[68] L.-L. Shen, G.-R. Zhang, S. Miao, J. Liu, B.-Q. Xu, ACS Catal. 6 (2016) 1680-1690.

[69] W. M. Haynes, CRC handbook of chemistry and physics, CRC press, 2014.

[70] C. E. Banks, T. J. Davies, G. G. Wildgoose, R. G. Compton, Chem. Commun. (2005) 829-841.

Supporting Information

1. Assemble of the microfluidic carbon based sensor

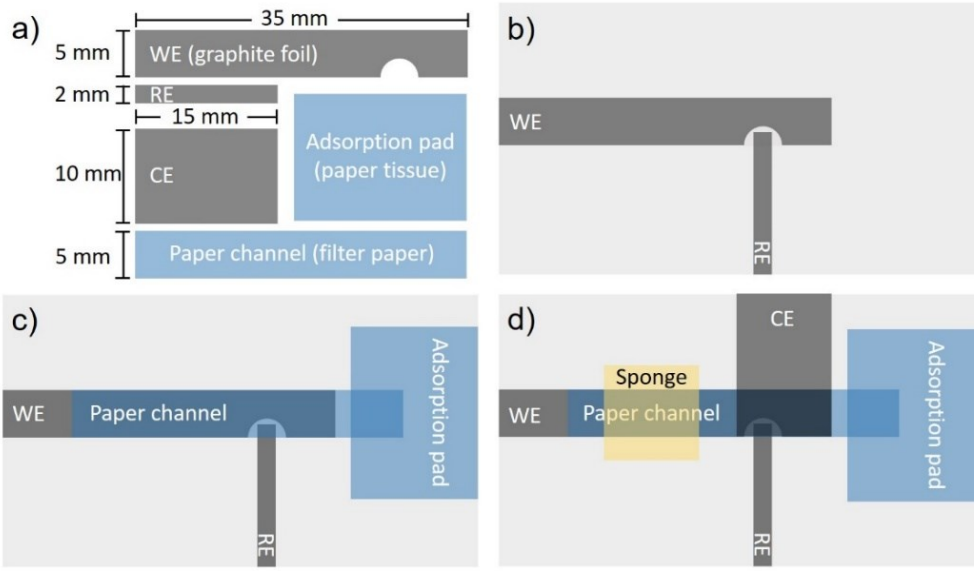

Figure S4.1 Top view of the sensor. (a) Working electrode (WE), reference electrode (RE), counter electrode (CE), paper channel and adsorption pad. (b)-(d) Scheme for the sensor assembling process.

2. Optimization of SWASV parameters and detection of heavy metal ions

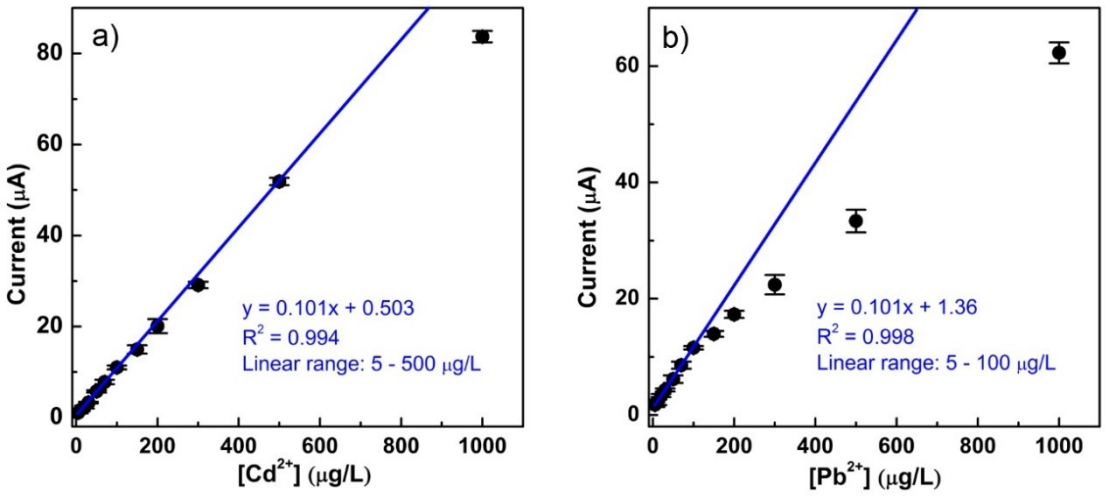

Figure S4.2 The calibration plots for Cd^{2+} (a) and Pb^{2+} (b) at concentrations ranging from 5 to 1000 µg/L. It can be seen that the linear range for Cd^{2+} can be extended up to at least 500 µg/L. However, for Pb^{2+}, the current would deviate from the linear plot at concentrations above 100 µg/L.

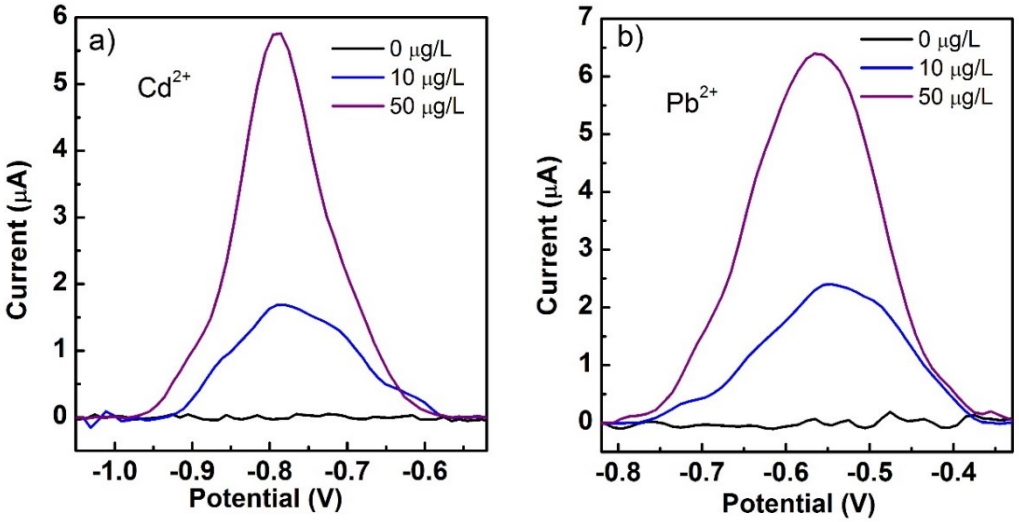

Figure S4.3 Square wave voltammograms for Cd^{2+} (a) and Pb^{2+} (b) in the commercial mineral water with and without intentionally added Cd^{2+} and Pb^{2+}.

3. Determination of detection limit

Detection limit (DL) was calculated by the following equation [1]:

$$DL = \frac{C_1 - C_0}{I_1 - I_0}(3\sigma)$$

Where C_1 is the concentration of the high sample; C_0 is the concentration of the blank; I_1 is the raw intensity of the high sample; I_0 is the raw intensity of the blank; σ is the standard deviation from 4 measurements of the blank.

4. Optimization of sensor configuration

Inspired by the ideas from the screen printing sensor, the sensor in our work was initially designed into a 2D configuration, as shown in **Figure S4.4**. CE, WE and RE are parallel to each other on the same horizontal plane and analyte flows along the paper channel over the 3 electrodes, as shown in **Figure S4.4a**. However, this configuration always leads to weak signal (**Figure S4.4b**), which may be caused by the high resistance between WE and CE as well as low current efficiency during deposition process.

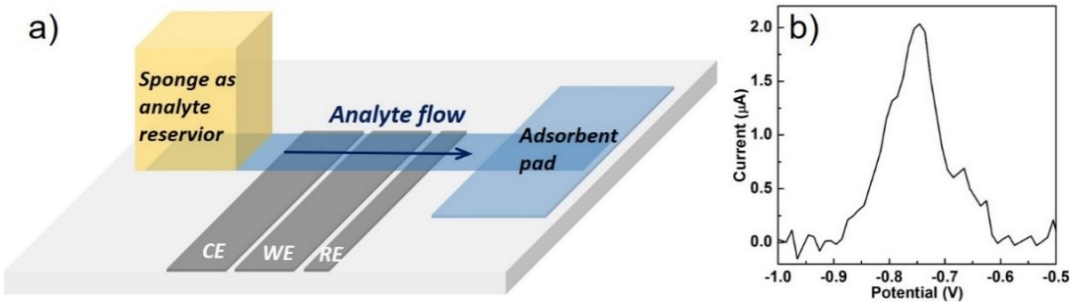

Figure S4.4 (a) Microfluidic carbon based sensor assembled in 2D configuration. (b) Square wave voltammograms for 100 μg/L Cd^{2+} by using 2D structured sensor.

Attempts were also made to directly use the graphite foil as working, counter and reference electrodes in a conventional electrochemical cell containing 20 mL analyte. In this electrochemical cell test, the SWV signal of 100 μg/L Cd^{2+} reaches 12 μA, as shown in **Figure S4.5**. This result is comparable that obtained in the microfluidic carbon based sensor (11.5 μA).

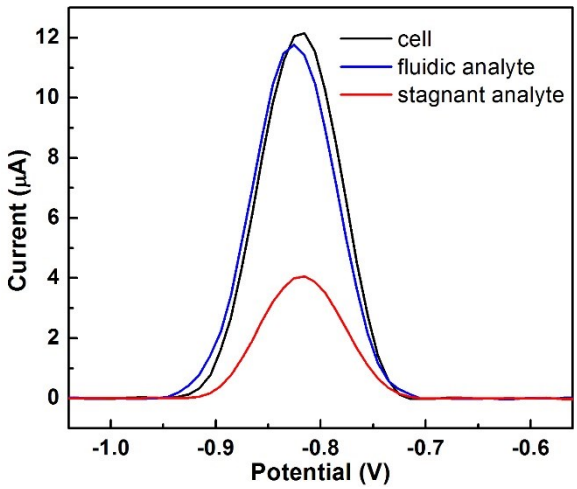

Figure S4.5 Square wave voltammograms for 100 μg/L Cd^{2+} by using electrochemical cell test (black line), fluidic analyte in 3D structured sensor (blue line) and stagnant analyte in 3D structured sensor (red line).

5. Effective surface area of WE in the μCS

To investigate the effective surface area of WE in the μCS, we have made attempts to change the area of the WE from 0.1 to 0.75 cm^2. It turns out that little change in the stripping voltammetry curves can be observed when the area of WE is large than 0.25 cm^2.

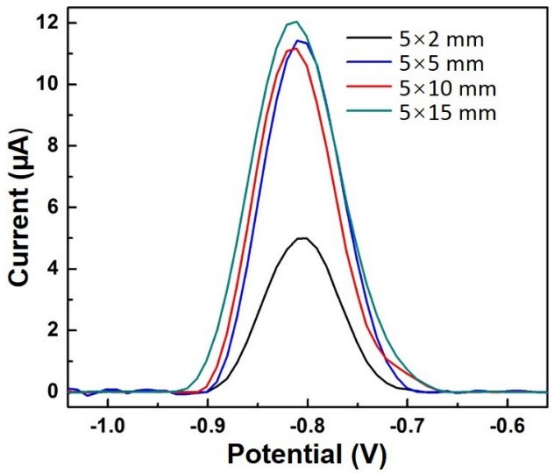

Figure S4.6 Square wave voltammograms for 100 μg/L Cd^{2+} by using μCS with different WE size.

6. Sensing performing of Bi_2O_3 modified working electrode

Bi_2O_3 modified working electrode was firstly prepared by dropping the mixture ink of Bi_2O_3 and carbon black (Vulcan XC-72) onto graphite foil [2]. After drying in air, the as prepared WE was tested in a conventional 3-electrode electrochemical cell, with graphite foil as counter and pseudo-reference electrode. One of the main drawbacks of Bi_2O_3 modified carbon electrode lies in its instability, as shown in **Figure S4.7**. After exposing WE for 5 min in air, the anodic stripping voltammetry peak current drops by 43%. The detection activity is only 34% of the initial activity after exposing the WE in air for 30 min.

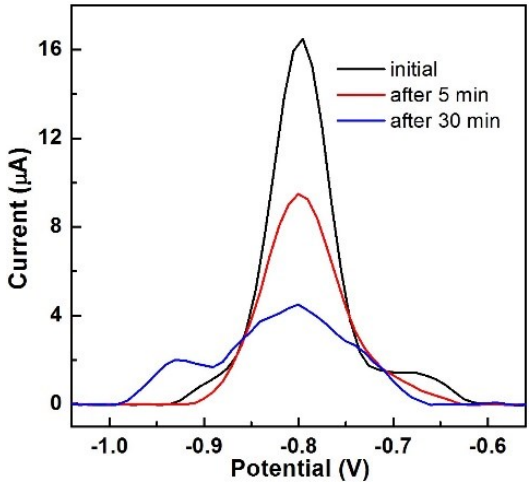

Figure S4.7 Square wave voltammograms by using Bi_2O_3 modified carbon electrode for Cd^{2+} detection.

References:

[1] V. Thomsen, D. Schatzlein, D. Mercuro, Spectroscopy 18 (2003) 112-114.

[2] R. O. Kadara, N. Jenkinson, C. E. Banks, Electroanal. 21 (2009) 2410-2414.

5 Toward best practices for improving paper-based microfluidic fuel cells

Liu-Liu Shen [a], Gui-Rong Zhang [a,*], Tizian Venter [b], Markus Biesalski [b], and Bastian J.M. Etzold [a,*]

[a] Ernst-Berl-Institut für Technische und Makromolekulare Chemie, Department of Chemistry, Technische Universität Darmstadt, Alarich-Weiss-Straße 8, 64287 Darmstadt, Germany

[b] Laboratory of Macromolecular Chemistry and Paper Chemistry, Department of Chemistry, Technische Universität Darmstadt, Petersenstrasse 22, 64287 Darmstadt, Germany

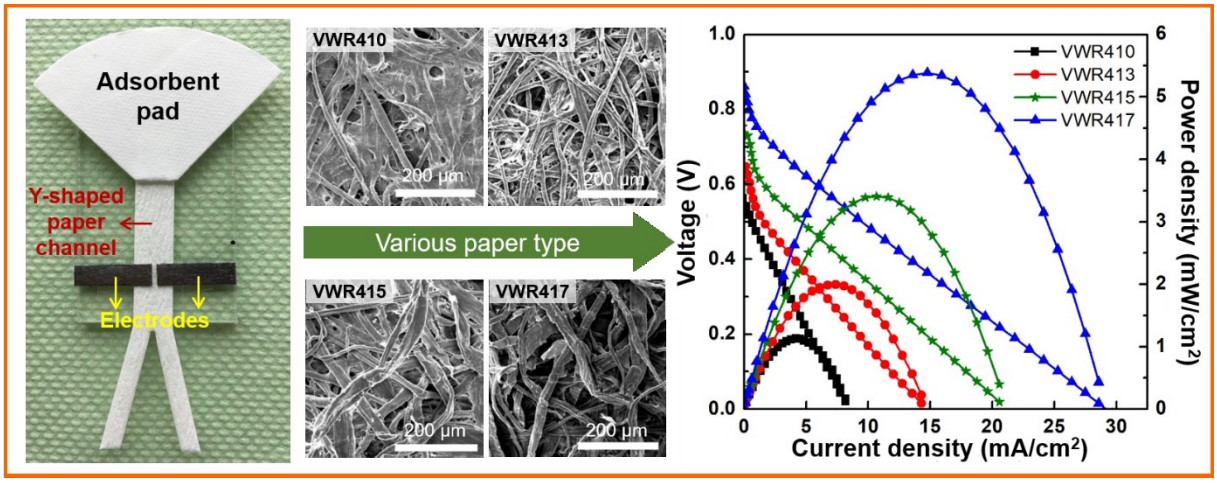

Redrafted from ***Electrochimica Acta 298 (2019) 398-399.***

Abstract

Paper-based microfluidic fuel cells emerge as a promising clean energy sources for small-scale electronic devices, while their broad-based applications require a comprehensive understanding of their structure-performance relationships. Here in this work, we made attempt to identify the key structural parameters that impact the overall performance of paper-based microfluidic fuel cells. The influences of fuel crossover, cell resistance, limitations from both anode and cathode, and in particular microfluidic paper channel properties have been systemically investigated and optimized toward the best practices. Among various structural parameters, we unravel for the first time that the overall performance of these paper-based microfluidic fuel cells is largely dependent on the textural properties of microfluidic paper channels. By correlating the fuel cell performance with the unambiguously determined flow rate of electrolyte within different paper channels, we found that a greater flow rate which is achieved by using paper with larger mean pore diameter, could result in higher peak power density and open circuit voltage. This performance enhancement would benefit from minimized reactant depletion near electrode surfaces and suppressed fuel crossover. Technically, an open circuit voltage of 0.86 V and a maximum power density of 7.10 mW/cm^2 can be achieved on a single cell (fuel: 4 M KCOOH; oxidant: air; electrolyte: 1 M KOH; catalyst: 0.2 mg/cm^2 Pd/C on 0.15 cm^2 graphite foil), and the maximum power output can be sustained for at least 1 h. The fuel cell power can also be easily increased proportionally when connecting two or more cells in series, which makes theses paper-based microfluidic fuel cells capable to power various electronic devices with different power requirements.

Keywords: Fuel cell; Paper microfluidic; Paper texture; Flow rate; Depletion effect

5.1 Introduction

There is a growing demand for small-scale energy sources due to the emergence of portable and disposable electronics, especially single-use devices in diagnostic and sensing fields, e.g., blood glucose analysis, on-chip disposable sensor, iontophoresis therapy, pregnancy test [1-4], where button cells are commonly used as energy sources. However, the disposal of these button cells after short-time use often causes energy waste and environment pollution [1, 3, 5]. Recently, Li-ion and Zn/MnO_2 based thin-film batteries have also been developed for low

power disposable electronics, but the production and disposal of these batteries have raised serious concerns about their adverse effects on human health and environment [6, 7]. Therefore, it is highly desirable to develop some miniaturized power supply platforms which can not only be integrated into small electronic devices but also have minimum impact on the ecosystem. To cope with this demand, microfluidic fuel cells emerge as a promising energy platform due to their features of being environment-friendly, lightweight, fully disposable and cost-effective [4, 8]. Moreover, the high energy density of fuel cells makes them prospective in commercial application to meet the great demands in clean energy sources for disposable electronics [4, 9-11].

In a microfluidic fuel cell, anode and cathode streams converge in the same main channel and flow in parallel to each other at low Reynolds numbers (i.e. laminar flow) with no significant turbulent mixing [12-21]. Due to the laminar flow, reactions can take place independently at anode and cathode in a microfluidic fuel cell without a physical membrane. H^+ (or OH^-) are transferred by diffusion from anode (cathode) to cathode (anode) through the interface of both streams, as shown in **Figure 5.1**. This membraneless microfluidic fuel cell concept was first proposed by Whitesides et al. in 2002 [18]. In their work, two separate streams, the anolyte and catholyte flow parallel to each other controlled by using syringe pumps. An open circuit of 1.52 V was obtained at a flow rate of 25 μL/s based on vanadium redox couple. Later on, the membraneless microfluidic fuel cells have been demonstrated by using different electrode catalysts, e.g., noble metal catalysts (Pt, Pd, PtRu alloy, Au), carbon-based catalysts (graphite, porous carbon, multi-walled carbon nanotubes), as well as various fuels and oxidants, e.g., vanadium compounds, methanol, formic acid, hydrogen, potassium permanganate, peroxide, oxygen, air in both acid and alkaline solutions [18-29]. Among all the design of microfluidic fuel cells, one of the key points lies in the control of fluid behavior, typically in a submillimeter scale. Conventional microfluidic devices require highly precise pumps and pressure control units to drive small amount of fluids [2, 30]. However, uses of pumps cause extra electric energy consumption [21], and at the same time make it challenging to miniaturize the whole device for portable applications [31]. A solution toward these drawbacks was proposed by Esquivel et al. by demonstrating the first paper-based self-pumping microfluidic fuel cell in 2014 [8]. Their work shows that when implemented in paper, microfluidic fuel cells benefit from the capillarity as reactants flow laterally within the paper channel without any external assistance. A maximum power density of 4.4 mW/cm^2 and

an OCV of 0.55 V were obtained using methanol as fuel on this paper-based microfluidic fuel cell. The intrinsic porosity of paper enables the spontaneous capillary flows within the paper channels, making paper an ideal platform for microfluidic devices without the need for the expensive auxiliary equipment [8, 30-38].

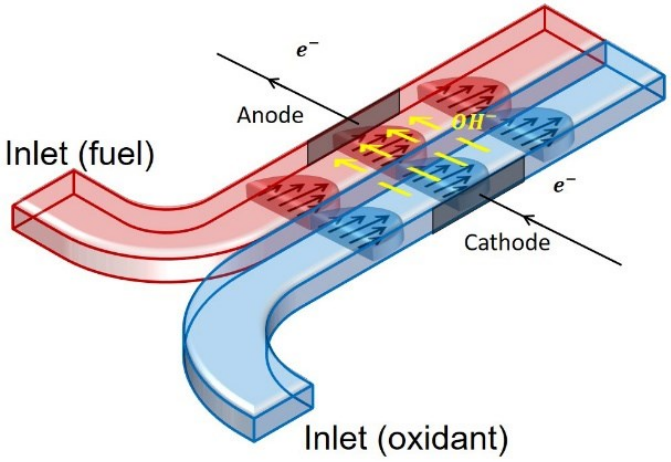

Figure 5.1 Scheme of the microfluidic fuel cell.

Many efforts have been made to improve the performance of microfluidic fuel cells by varying electrode catalysts, electrolyte, redox chemistry, and cell configurations [25, 27, 28, 39-44], while systematic structure-performance relationship of the paper-based microfluidic fuel cell is still lacking. For a conventional microfluidic fuel cell, there is a lack of engineering solutions for important functions such as integration of fuel and oxidant storage, waste handling, and low-power microfluidics-based fluid delivery using integrated micropumps and microvalves [45]. Thus the main challenge is to develop a microfluidic system, including auxiliary equipment and fluid storage [45]. Analogously, for a paper-based microfluidic fuel cell, the electrolyte microfluidic behavior is supposed to play a key role in determining the device performance. The microfluidic behavior within the paper channels is affected not only by the intrinsic properties of the solutions (e.g., surface tension and viscosity), but also by paper properties (e.g., fiber origin and pore size) as well as geometry and surrounding conditions (e.g., temperature, humidity) [39, 42, 46, 47]. Among these parameters, the paper properties are supposed to play an essential role in the flow control, which determines the final performance of a paper-based microfluidic fuel cell. However, the influence of paper properties on the electrolyte flow behavior and microfluidic fuel cell performance remains unelucidated.

To this end, in the current work, paper-based microfluidic fuel cells featuring lightweight, thinness, and cost-effectiveness were fabricated. Fuel cell tests were carried out using formate as fuel, O2 from air as oxidant, and KOH solution was used as the supporting electrolyte. The electrochemical reactions taking place in this fuel cell are described by the following equations (**5.1**) – (**5.3**):

Anode: $HCOO^- + OH^- \rightarrow CO_2 + H_2O + 2e^-$ $E_A = -1.08\,V$ (**5.1**)

Cathode: $H_2O + 1/2O_2 + 2e^- \rightarrow 2OH^-$ $E_C = 0.40\,V$ (**5.2**)

Overall: $HCOO^- + 1/2O_2 \rightarrow CO_2 + OH^-$ $E = 1.48\,V$ (**5.3**)

The influences of the fuel crossover, limitations at cathode and anode, concentrations of fuel/oxidants, and especially the properties of microfluidic paper channels on the obtainable power density were investigated and shown point by point. This allows to gain insight into the best practices for constructing high-performing paper-based microfluidic fuel cells. It discloses that the overall performance of these paper-based microfluidic fuel cells is mainly limited by the depletion of fuel/oxidants at the electrodes, which can be rationally regulated by tuning the electrolyte flow rate using paper channels with different textural properties. We believe that these findings may have great implications for understanding the microfluidic behavior of electrolytes on paper and assist the design and application of paper-based microfluidic fuel cells, and then could be expanded to other paper-based microfluidic devices.

5.2 Experimental section

Material and chemicals. Potassium hydroxide (Alfa Aesar), potassium formate (Alfa Aesar), Pd/C (10 wt. %, type 487, Alfa Aesar), hydrogen peroxide (35%, Acros Organics), new coccine (Sigma-Aldrich), indigo carmine (Sigma-Aldrich), ethanol (99.8%, VWR) and Nafion solution (5 wt%, Sigma-Aldrich) were all analytical grades reagents and used as received without any further purification. Graphite foil was purchased from Sigraflex. Filter paper (grade 410, 413, 415, 417) was purchased from VWR. All the solutions were prepared by using double-distilled water.

Device fabrication. A piece of graphite foil with thickness of 0.5 mm was firstly cut into rectangular shaped pieces with 20 mm in length and x mm in width (x = 2.5, 5, 10, 15), and

then cleaned with ethanol and deionized water under ultrasonication. PMMA substrate was cleaned under the same protocols as graphite foil. A catalyst ink (30 mg/mL) was prepared by ultrasonic dispersion of Pd/C in water. A certain amount of suspension was carefully deposited onto the graphite foil covering an area of $3x$ mm^2 (x = 2.5, 5, 10, 15). After dried in air for 30 min, a certain amount of Nafion solution was carefully casted onto the catalyst layer to prevent any catalyst detachment, and then the electrodes were air dried for 30 min at room temperature. The Pd loading on the graphite was varied from 0.033 to 0.20 mg/cm^2, and the mass ratio of Pd to Nafion is fixed at 150:1. Filter paper was cut into "Y" shaped geometry using a custom-made die to serve as bi-laminar flow channel with two inlets. The design and dimensions are detailed in **Figure S5.1**. The Y shaped filter paper was placed on the PMMA substrate for easy operation, and then electrodes were placed symmetrically on the paper channel. Tape was used to fix the electrodes onto the substrate. The gap between anode and cathode electrodes was controlled at 2 mm. Electrodes with four different widths (i.e., 2.5, 5, 10, 15 mm) were used for constructing microfluidic fuel cells. For comparison, their current and power were normalized to the projected geometric electrode active area (EAA, i.e., 3×2.5, 3×5, 3×10, 3×15 mm^2), which is defined as the overlapping area between the catalyst coated graphite foil and the paper channel. A quarter-fan shaped absorbent pad was placed at the end of the paper channel. Fuel cell tests were carried out using KCOOH as fuel, O_2 from air as oxidant, and KOH solution was used as the supporting electrolyte for both anolyte and catholyte. The anolyte (mix solution of KCOOH and KOH) and catholyte (air-saturated KOH solution with oxygen concentration of ca. 0.028 mM) were added into two sample vials to serve as oxidant and fuel reservoirs, respectively.

Electrochemical measurements. Electrochemical measurements were carried out on a PMC-1000 multichannel potentiostat (AMETEK) controlled by Versastudio software. The device was placed horizontally and two ends of the Y shaped channel were separately and simultaneously immersed in the anode and cathode reservoirs, and then anolyte and catholyte begin to flow side-by-side spontaneously in a laminar way. After open circuit voltage (V-t) gets stabilized, the cell resistance between anode and cathode electrodes was determined by conducting the AC impedance analysis (10 kHz, 10 mV). The voltage-current (V-I) measurements were then carried out by linear potential scanning from open circuit voltage to 10 mV with a step height of 20 mV at 2 s intervals. To probe the operation durability of these paper-based microfluidic fuel cells, chronoamperometry (I-t) measurements were carried out

for 1 h at 0.4 V, at which potential microfluidic fuel cells regardless of paper channel types can approximately reach their peak power. For each condition, the measurements were conducted at least four times by using different fuel cells (cell number ≥ 4) to generate the error bars (defined as the relative standard deviation).

Structural analysis. The morphology of the four types of VWR filter paper was investigated by using Scanning Electron Microscopy (Philips XL30 FEG) operated at an accelerating voltage of 30 kV. The thickness of the paper materials was measured by using a ProGage Thickness tester (Thwing-Albert). The paper textural parameters including porosity and mean pore diameter (characteristic length) were adapted from the product specification of the manufacturer (VWR).

Flow rate measurements. Flow rate of electrolyte within different paper channels was measured by monitoring the mass gain of the adsorbent pad over time using an analytical balance. A digital webcam (Logitech C920 PRO HD) was used to record the readings of the balance. As shown in **Figure S5.2**, the two inlets of the Y-shaped channel were immersed in two reservoirs out of the balance, and the absorbent pad was placed on the balance. The two reservoirs were filled with catholyte (1 M KOH, 1.049 g/mL at 20 °C) and anolyte (1 M KOH and 2 M KCOOH, 1.135 g/mL at 20 °C), respectively. The solution density was obtained by weighting 1.000 mL solution. The balance was tared immediately when the liquid front reached the adsorbent pad. A steady weight increase can be observed until the adsorbent pad being fully saturated by the electrolyte. The mean density (1.092 g/mL at 20 °C) of the two solutions from the two reservoirs was used when the mass (g) of the electrolyte on adsorbent pad was converted into volume (mL). The volume (mL) of the electrolyte on adsorbent pad was then plotted against time (min), and linear regression was used to determine the volumetric flow rate.

5.3 Results and discussion

The performance of paper-based microfluidic fuel cells is determined by the interplay of a wide range of structural parameters, including electrode layout, concentrations of electrolyte and reactants, catalyst loadings and property of paper channel materials which is the focus of the current study. Before we can unambiguously correlate the paper property with fuel cell performance, firstly, the influence of the other structural parameters and their associated

physicochemical properties (e.g., fuel crossover, cell resistance, limitations of electrode reactions) are studied and the fuel cell configuration is to be optimized. Secondly, the influence of the paper channels will be investigated based on a configurationally optimized fuel cell, and the correlations between the textural properties of paper materials and the electrolyte flow rate as well as the fuel cell performance will be deduced. Thirdly, the practical application of paper-based microfluidic fuel cells for electronic devices with varied power requirements will be demonstrated.

5.3.1 Optimization of fuel cell configurations

Fuel crossover effect. The slow kinetics of oxygen reduction reaction (ORR) is considered to be one of the major limitations in conventional polymer electrolyte membrane fuel cell [48-52]. Although ORR has a faster kinetics in alkaline than in acidic electrolyte, one of the major challenges for conventional alkaline fuel cells lies in the development of anion exchange membranes [53-55]. Nevertheless, the membrane can be completely omitted in a paper-based microfluidic fuel cell device, which enables us to take the full advantage of faster ORR kinetics in alkaline electrolyte. However, due to the lack of a physical barrier between the anode and cathode, fuel crossover from anode to cathode seems to be inevitable, which might result in a mixed potential at the cathode and consequently a power loss in the fuel cell [19].

In order to obtain a clear picture of the crossover effect of bi-laminar flows within one single microfluidic paper channel, two dye solutions with different colors (red: new coccine, blue: indigo carmine) were used to mimic the flows of anolyte and catholyte, respectively. The flow test was carried out by placing the two ends of a Y-shaped paper strip into two dye solutions, and the imbibition of solutions in the paper channel was recorded as the time elapsed from 0 to 600 s, as shown in **Figure 5.2**. It can be found that the majority of the dye solutions flows separately along the channel without any significant mixing. At the same time, cross diffusion (crossover) can also be observed at the interface of the two streams, and the cross diffusion zone becomes broader along the flow direction, which is consistent with the simulation results [15, 47]. These results indicate that the crossover indeed takes place at the interface of the two streams, and therefore the influence of the fuel crossover on the performance of microfluidic fuel cells needs to be properly investigated.

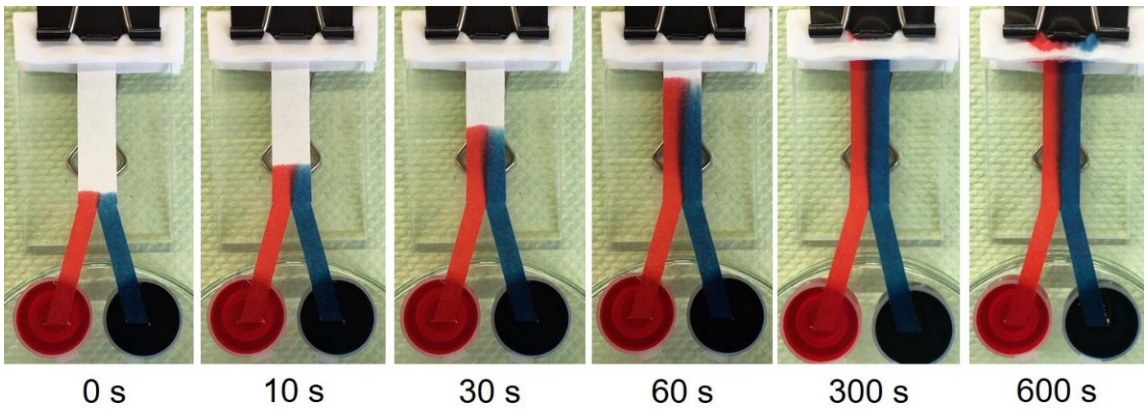

Figure 5.2 Bi-stream laminar flow on a Y-shaped paper (grade 415) channel.

To study the crossover effect, anode and cathode were first placed separately with varied distances along the electrolyte flow direction, as shown in **Figure S5.3a**. The intention of this design is to facilitate the fuel to be consumed at the anode before reaching the cathode, in a hope to minimize the fuel crossover effect by preventing the oxidation reaction of fuel at the cathode. However, as shown in **Figure S5.3b-c**, the longer distance between anode and cathode electrodes, the lower peak power density of the fuel cell. The worse performance likely arises from the cell resistance gain between anode and cathode when increasing the distance between these two electrodes. As shown in **Figure S5.3c**, the cell resistance (ohmic resistance) which is determined by conducting impedance analyses is increased by a factor of over 3 along with the relative distance of anode and cathode. The inflation of this ohmic resistance would give birth to the loss of fuel cell power [56]. Similar phenomenon was also found in pump-based microfluidic fuel cells. For example, Sung and coworkers found that increasing the relative distance between anode and cathode electrodes from 1 to 100 mm resulted in a 26% drop in peak power [24]. In view of this, the anode and cathode electrodes were placed in a symmetrical configuration on the Y-shaped paper channel for the subsequent investigations. Secondly, in order to study how strongly the observed mixing and thus fuel crossover reduce the fuel cell power density, the distance of the electrodes from the splitting point of the Y-shaped paper channel was varied. As the dye study showed, the longer the distance to the splitting point, the broader the cross diffusion zone. Despite this visually observed mixing, it was found that the difference in fuel cell performance is within the measurement error and not influenced by the electrode pair position (**Figure S5.4**), indicating that the electrolyte cross diffusion is negligible within the studied distance of up to 2 cm.

Influence of cell resistance. As discussed in the above section, the cell resistance between anode and cathode seems to play an important role in controlling the performance of a microfluidic fuel cell. The cell resistance is not only affected by the cell configuration, but also largely determined by the concentration/conductivity of electrolyte. Herein, the concentration of KOH in the electrolyte was varied from 0.2 to 2 M, and the corresponding fuel cell performance is compared (**Figure S5.5**). It can be seen that peak power density is enhanced by a factor of 4 when the KOH concentration is increased from 0.5 to 1.5 M. A further increase in the KOH concentration shows negligible improvement (**Figure S5.5b**). The increase in power density seems to be strongly coupled to the reduced cell resistance, which decreased by over 90% by increasing the KOH concentration from 0.2 to 1.5 M (**Figure S5.5**). While it needs to be mentioned that a higher KOH concentration can also promote the anodic formate oxidation reaction [57, 58], due to the clear link of performance to the resistance and as the cathodic kinetics are more likely to limit the fuel cell, we believe that the higher conductivity of the electrolyte shows the main influence here.

While with more concentrated KOH solution ($\geq$ 1.5 M) the highest initial peak power densities resulted, it was also observed that the fuel cell performance becomes unstable and drops quickly within 5 min, as shown in **Figure S5.6**, which may arise from the degradation of the electrode catalyst/paper cellulose. Based on these results, we can learn that the cell resistance which is highly sensitive to the electrolyte concentration, plays an important role in determining the performance of a paper-based microfluidic fuel. In the following investigations, KOH concentration of 1.0 M was chosen for both anolyte and catholyte as a tradeoff between low cell resistance and good fuel cell operation stability.

Limitations at the cathode. Since no air breathing electrode is used in these paper-based microfluidic fuel cells and oxidant (i.e., O_2) solely comes from the naturally dissolved air in the electrolyte, depletion of the dissolved oxidant at the cathode may limit the obtainable power density [59]. Herein, the influence of oxidant on the performance of these paper-based microfluidic fuel cells (**Figure 5.3**) is investigated by varying oxidants in the catholyte stream. The first attempt was made by saturating the catholyte with O_2 by bubbling pure O_2 into the electrolyte reservoir, we found that the peak power density of the fuel cell is dramatically enhanced by 55%. Furthermore, another attempt was made by using H_2O_2 solution (35%) as the catholyte in microfluidic fuel, and it turns out that the peak power

density is enhanced by 47% compared to that of the fuel cell using dissolved air, while fluctuation of the V-I curve can be observed (**Figure 5.3**), which might arise from the formation of gaseous O_2 during the H_2O_2 decomposition. These results confirm that the performance of these paper-based microfluidic fuel cells is largely limited by the cathode reaction, e.g., the depletion of oxidants at the electrode surfaces. At the same time, it can be seen that for a given paper-based microfluidic fuel cell, its power density can be effectively improved by increasing the concentration of oxidant in the catholyte or varying the redox chemistry at the cathode. This result is not surprising, considering that increasing the O_2 concentration in catholyte or introducing stronger oxidizer have also been demonstrated as efficient methods to boost the cell performance of the conventional pump-based microfluidic fuel cells [26, 60]. However, we have to admit that for practical applications, air based microfluidic fuel cells are much more preferable due to their overwhelming advantages like low-cost, operation convenience, clean product and minimum environment impact. Therefore, despite the room left to further improve their power output, naturally dissolved air is selected as the oxidant in the following investigations.

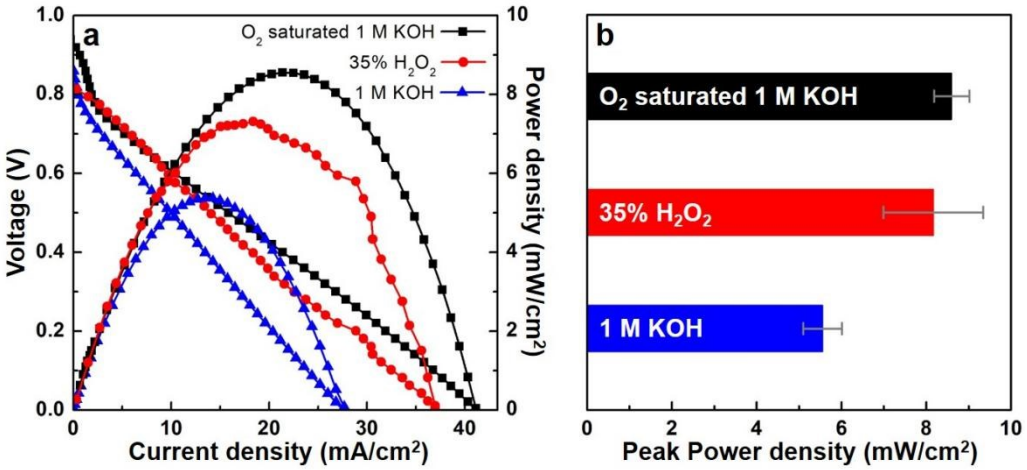

Figure 5.3 (a) Voltage-current measurement and (b) comparison of the peak power of the paper-based microfluidic fuel cells with different oxidants. The errors bars (defined as the standard deviation) were generated by conducting four independent measurements. (Formate concentration: 4 M; KOH concentration in anolyte: 1 M; EAA: 3×5 mm^2; Pd loading: 0.1 mg/cm^2; paper: grade 417).

Limitations at the anode. While we have seen limitations at the cathode side, possible limitations at the anode side also need to be clarified. It should be noted that these studies

about the anode limitation are overlaid by the cathode limitation as discussed prior. Nevertheless, trends for reducing anode side limitations can still be deduced. To investigate the key parameters at the anode that limit the obtainable power density, the Pd loading on the electrodes was first varied from 0.033 to 0.20 mg/cm^2, while the formate concentration in the anolyte was fixed at 2 M. As shown in **Figure 5.4a**, the peak power density increases linearly when Pd loading increases from 0.033 to 0.10 mg/cm^2. In this region the fuel cell performance seems to be mainly limited by the number of catalytically active sites and intrinsic reaction rate. When further increasing Pd loading up to 0.20 mg/cm^2, a plateau for the power density is reached. The low utilization of the additional added catalyst in this high loading region could stem from i) a mass transfer limitation from the surface through the catalyst layer coated on the electrode or ii) depletion of the fuel or oxygen species along the electrode, hence from the inlet to the outlet. To check for depletion effects, the fuel concentration was varied for the different Pd loadings. Increasing the formate concentration to 3 and 4 M imposes little effect on the peak power density for loadings below 0.10 mg/cm^2 (**Figure 5.4b**). While for electrode with higher Pd loadings, an increase in the peak power density can only be leveraged if the highest fuel concentration is employed. Nevertheless, in this region the increase is under proportional. In order to gain more insights, further attempt was made to increase the absolute catalyst amount by widening the catalyst coated working electrode while keeping the catalyst loading fixed at 0.10 mg/cm^2. As shown in **Figure S5.7**, the absolute power increases when the electrodes are widened. However, when the electrode width increases from 5 to 15 mm, the peak power density decreases from 5.33 to 3.24 and 3.60 mW/cm^2 for formate concentrations of 2 and 3 M, respectively (**Figure 5.4c**). Similarly, Thorson et al. reached the same conclusion based on pump-based microfluidic fuel cells, that the fuel cells fabricated using shorter/smaller electrodes can usually exhibit higher power densities for a given flow rate, which is rationalized by the reduced boundary layer depletion effect [28]. However, this is not the case when the formate concentration is as high as 4 M (**Figure 5.4c**), under which condition the power density of the resulting fuel cell stays almost unchanged with enlarging the electrode size. Both variations indicate that up to a catalyst concentration of 0.10 mg/cm^2 the depletion of fuel is the limiting factor, which can be avoided by increasing the fuel concentration. Higher catalyst loading above 0.10 mg/cm^2 seems to suffer from mass transfer limitation within the catalyst layer and thus not all catalyst can be used efficiently. This is illustrated clearly in **Figure 5.4d** which compares the obtainable peak power vs. total mass of Pd. As presented above, the total mass of Pd can be increased either

by enlarging the electrode size (width) or by thickening the catalyst layer. It can be found that the former approach can result in a linear increase in the absolute peak power, implying a high catalyst utilization efficiency. However, following the latter approach, the peak power cannot be proportionally increased any more when the catalyst layer gets too thick, which is not surprising since catalyst layer thickening is accompanied by a higher mass transportation resistance within the catalyst layer and consequently a lower catalyst utilization efficiency.

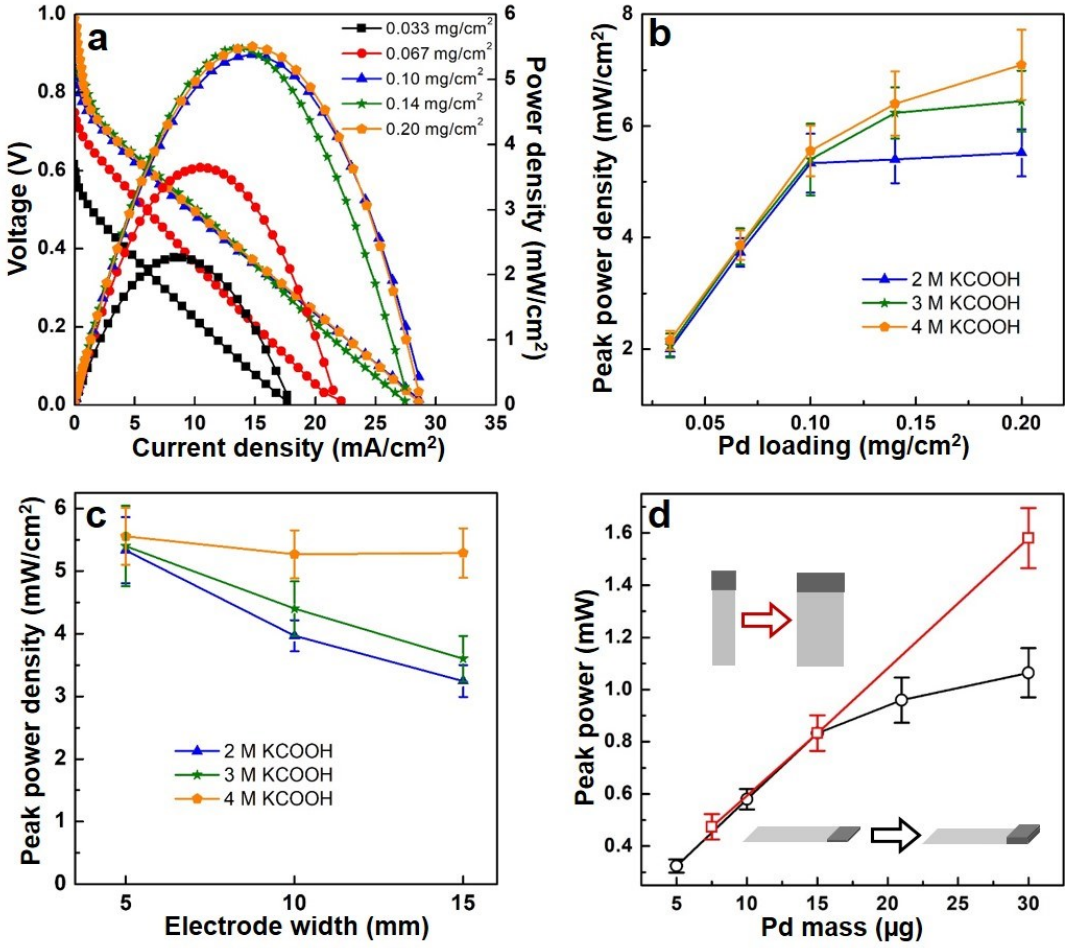

Figure 5.4 (a) Voltage-current measurement of paper-based microfluidic fuel cell at different Pd loadings (KOH concentration: 1 M; formate concentration: 2 M; EAA: 3×5 mm^2). (b) Influence of Pd loading on the peak power density at different formate concentrations. (KOH concentration: 1 M; EAA: 3×5 mm^2). (c) Influence of electrode size on the peak power density at different formate concentrations. (KOH concentration: 1 M; Pd loading: 0.1 mg/cm^2; EAA: 3×5, 3×10, 3×15 mm^2). (d) Influence of the absolute Pd mass on peak power. Black circle: increasing the Pd mass by thickening the catalyst layer (KOH concentration: 1 M; formate concentration: 4 M; EAA: 3×5 mm^2). Red square: increasing the Pd mass by

enlarging the catalyst coated electrode (EAA, 3×2.5, 3×5, 3×10 mm^2) while fixing the Pd loading at 0.10 mg/cm^2. Grade 417 paper were used for all these measurements.

5.3.2 Influences of paper channel properties

As discussed in the above section, the overall performance of the paper-based microfluidic fuel cell is largely limited by the depletion of both oxidant and fuel at the cathode and anode. The depletion effect can be minimized not only by using more concentrated oxidants and/or fuels, but also by regulating the flow rate of anolyte and catholyte through the electrodes. For a paper-based microfluidic device, among numerous factors, the flow rate of the electrolyte is supposed to be mainly influenced by the intrinsic textural properties of the paper channel. The prior electrochemistry measurement results were obtained with grade 417 paper, and in the following section, influence of paper properties on the microfluidic fuel cell performance is presented by introducing other three types of filter paper (grade 410, 413,415) with different textures.

Textural properties of different paper materials. The microstructure of the paper materials was first characterized using a scanning electron microscope (SEM). The SEM images in **Figure 5.5** show that these four types of paper are featuring different pore sizes and fiber densities. For instance, the grade 410 paper exhibits rather dense structure along with relatively small pore sizes. In contrast, the paper fiber texture in grade 417 paper features more opened structure than the other 3 types of paper and the pore size is significantly larger. Both the pore sizes and fiber densities of grade 413 and 415 paper lie somewhere between those of 410 and 417 paper, which is consistent with the order of their specified mean pore diameters (**Table 5.1**). The detailed textural properties of these filter papers, including pore size, porosity, thickness and weight can also be found in **Table 5.1**. These paper materials were cut into the Y-shaped pieces with the same size and then assembled into microfluidic fuel cells. The above optimized parameters including cell configuration, catalyst loading, and concentrations of formate and KOH were adopted in the following investigation.

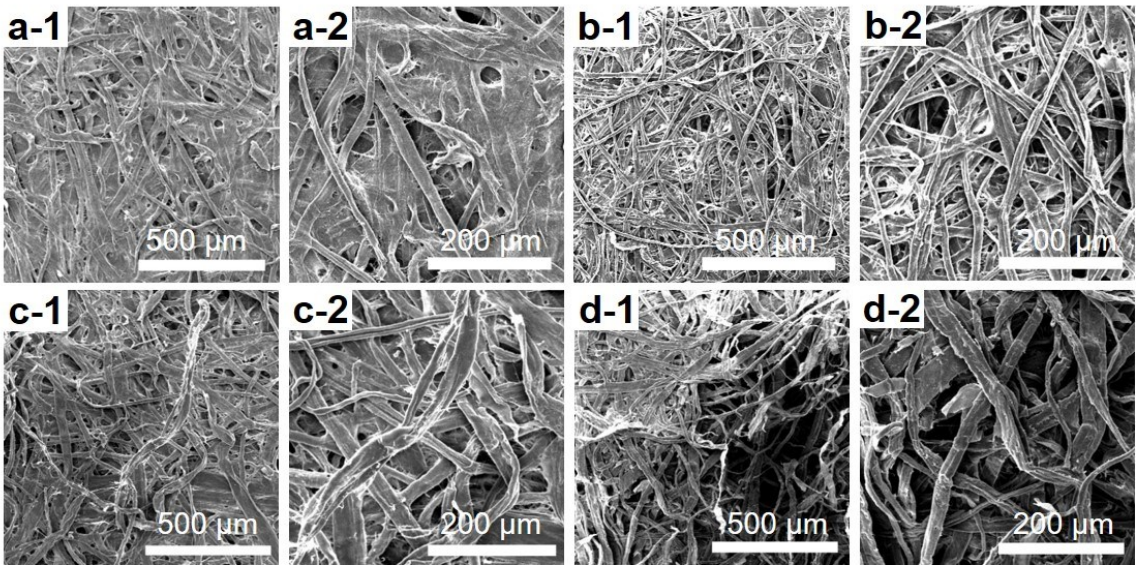

Figure 5.5 SEM images of the VWR grade 410 (a), 413 (b), 415 (c) and 417 (d) filter paper.

Table 5.1 Properties of the VWR filter paper

Paper	Max. Pore size (µm)	Min. Pore size (µm)	Weight (g/m^2)	Thickness (µm)	Porosity (%)
VWR410	20	9	80	150	15-30
VWR413	45	20	73	160	18-36
VWR415	50	31	80	160	40-80
VWR417	50	/	110	147	30-70

Electrochemical performance of microfluidic fuel cells using different papers. The open circuit voltage (OCV) and peak power density, as two important parameters in quantifying the performance of microfluidic fuel cells, are compared in **Figure 5.6a** for the fuel cells fabricated using different papers. Their corresponding polarization curves can be found in **Figure S5.8**. It is notable that the fuel cell performance varies sensitively with the paper types. The fuel cell using the paper that features a larger mean pore diameter can always give a better performance in terms of both OCV and peak power density. Specifically, the OCV and peak power density are increased from 0.55 V, 1.17 mW/cm^2 on the 410 paper with the smallest mean pore diameter (14.5 µm) to 0.86 V, 5.33 mW/cm^2 on the 417 paper with the largest mean pore diameter (50 µm). This is also the case for pump-based microfluidic fuel cells, as reported by Choban and Li based on different cell configurations that a higher flow rate, which is regulated using micropumps, can also bring about significant enhancement in fuel cell performance, despite much higher flow rates (i.e., 0.3 – 1.6 mL/min) being employed

during the measurements compared to that of our current paper-based microfluidic fuel cells (i.e., 0.0012 – 0.0590 mL/min) [19, 60].

Besides activity also the influence of the paper employed on the fuel cell operation stability was studied. To achieve this, the power output was monitored over time by carrying out chronoamperometry tests at 0.4 V (**Figure 5.6b**). Firstly, we observed that the activity order was consistent with the V-I measurements, i.e., the paper with larger mean pore diameter can bring about higher power density; secondly, the power density drop is less than < 9% for all the paper channels after 1 h test. These results demonstrate that the filter paper materials can maintain their structural integrity for at least 1 h in presence of the aggressive alkaline electrolyte, and these paper-based microfluidic fuel cells exhibit great robustness during operation, which would be of significance for practical applications.

Correlation between paper material properties and fluid flow rate. Since the capillary flow rate of a fluid within a porous medium, e.g., a cellulose paper as in the current study, is directly influenced by the mean pore diameter of the porous medium, it is reasonable to hypothesize that the observed correlation between the fuel cell power and the mean pore diameter is a resultant of the increased flow rate and thus reduced depletion of fuel and oxidant [23]. To validate the hypothesis, the actual flow rate of electrolyte within different paper channels in connection with absorbent pads needs to be properly determined. Given that the presence of the absorbent pad will greatly impede the attempt to analyze the liquid imbibition dynamics by visually tracking the front of the flow, in the current work, a new method is proposed to unambiguously determine the flow rate of electrolyte by monitoring the weight gain of the absorbent pad over the liquid imbibition time. The weight gain versus elapsed-time can then be utilized to analyze the flow dynamics of electrolyte within different paper channels, which is summarized in **Figure 5.6c**. The mass (volume) of the solution increases linearly in the first 60 min over the grade 410, 413 and 415 paper channels. As to the grade 417 paper, the solution mass (volume) also keeps increasing linearly with time at the initial stage, while deviation from this linear trend was observed after 30 min. The deviation is caused by the limited capacity of the absorbed pad, as evidenced by the extended linear region by using more absorbent pads (**Figure S5.9**). Linear regression analyses of these volume vs. time plots were employed to deduce flow rates on different paper channels (**Figure 5.6c** and **Table S5.1**), from which we can see that quasi-stationary flows can be

obtained over all these paper channels. This is also in line with the stable power output of fuel cells (**Figure 5.6b**). As a matter of fact, the liquid imbibition dynamics within a porous medium (e.g., paper) usually follows the Lucas-Washburn equation, which predicts that the liquid flow rate will diminish with flow distance and elapsed time [42]. In the current work, the deviation from the above Lucas-Washburn behavior is caused by the presence of the absorbent pads, which breaks the assumption of constant cross section for the Lucas-Washburn equation. In presence of an absorbent pad, the capillary flow can be sustained over time because the liquid can encounter continuously increased unwetted pores as the flow advanced in the absorbent pad, and this phenomenon has also been observed in other paper-based microfluidic systems [34].

Remarkably, the flow rate of electrolyte is greatly dependent on the nature of paper channels, as we can see that the flow rate on grade 417 paper (59 μL/min) is almost 50 times higher than that on grade 410 paper (1.2 μL/min). The difference in flow rate on four types of filter paper is the reflection of the Darcy's law:

$$v = \frac{k}{\mu}\frac{\Delta P}{\Delta x} \tag{5.4}$$

where v is the flow velocity (m/s), k is the permeability (m^2), μ is the viscosity (Pa·s), $\Delta P/\Delta x$ represents the pressure change per unit length (Pa/m). In the paper-based microfluidic system, the capillarity force is mainly caused by the unwetted pores in the adsorbent pad. Since same adsorbent pads are used to maintain the steady microfluidic flow on different paper, and all the paper channels are designed in the same geometry, the change of pressure per unit length is considered as the same. Therefore, the flow rate is positively correlated to the permeability of the paper, which is approximately proportional to the square of the mean pore size [61].

In **Figure 5.6c**, peak power density for each microfluidic fuel cell is plotted against the flow rate for comparison. The most prominent phenomenon can be identified is the strong dependence of power density on the flow rate (**Figure 5.6d**). For a conventional microfluidic fuel cell, its power output performance can be regulated by directly applying different flow rates using a pump to meet power requirements of different applications. Herein, the current work demonstrates that the both the flow rate as well as the associated power output of a paper-based microfluidic fuel cell can also be rationally regulated by choosing paper channels

with different textures. The strong dependence of power density on the flow rate indicates that the performance of these microfluidic fuel cells is predominantly limited by the fuel and/or oxidant depletion near the electrode, which is in accordance with the limitations for anode and cathode side described prior. Note that the cell resistance differentiates by varying paper in the microfluidic fuel cell. As shown in **Figure S5.10**, the cell resistance decreases when the pore size of paper increases, which indicates that larger pore size helps to increase the ionic conductivity. Therefore, the highest power density obtained on 417 paper-based microfluidic fuel cell may benefit from both the slowest fuel/oxidant depletion and the lowest cell resistance.

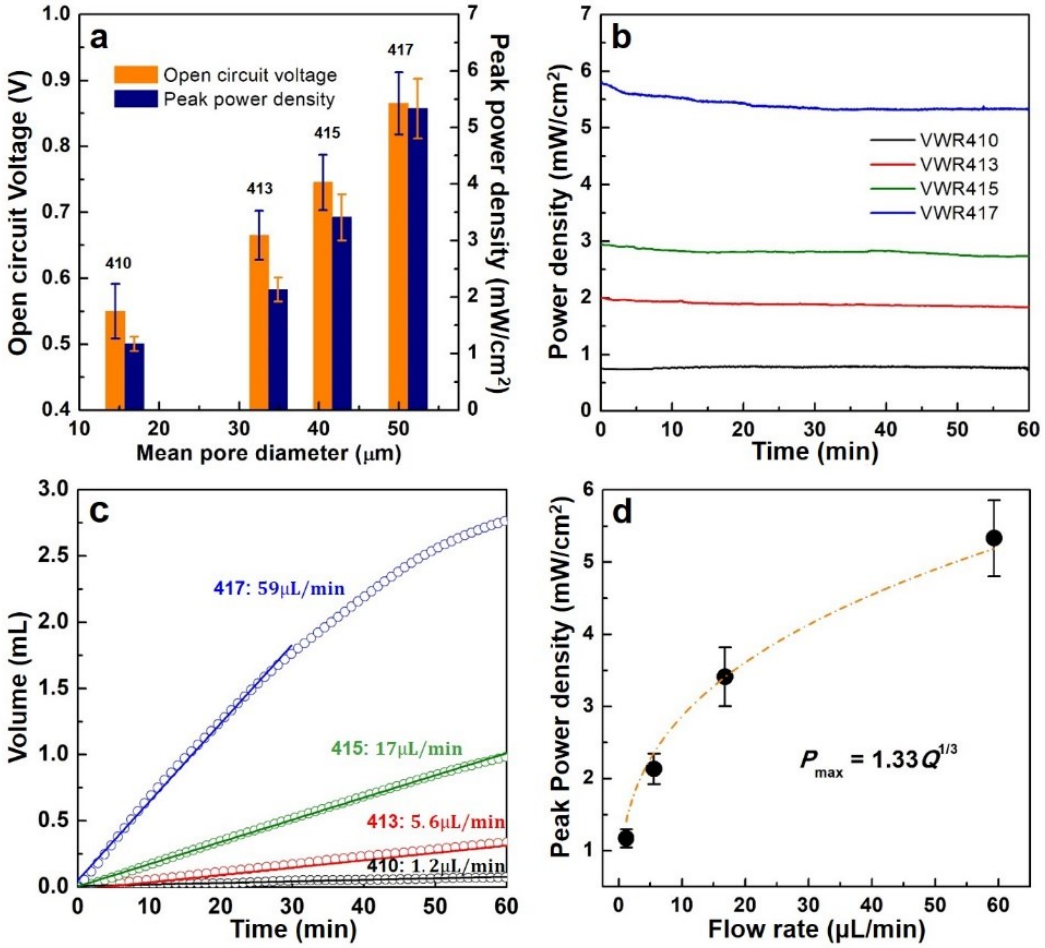

Figure 5.6 Comparisons of open circuit voltage and peak power density (a) and chronoamperometry test (b) of paper-based microfluidic fuel cells fabricated with different papers. (Formate concentration: 2 M; KOH concentration: 1 M; EAA: 3×5 mm^2; Pd loading: 0.1 mg/cm^2). (c) Plots of electrolyte volume absorbed by the absorbent pad vs. the elapsed time. The flow rates calculated by linear regression analyses are marked. (d) Plot of the peak

power density vs. the experimentally determined flow rate. (Formate concentration: 2 M; KOH concentration: 1 M; EAA: 3×5 mm^2; Pd loading: 0.1 mg/cm^2).

Attempts were also made to find a quantitative correlation between peak power density and flow rate. Interestingly we found that the peak power density is proportional to the cube root of the volumetric flow rate, as described in the following equation:

$$P_{max} = 1.33Q^{1/3} \quad (\mathbf{5.5})$$

where P_{max} denotes the peak power density (mW/cm^2), and Q stands for the flow rate (μL/min). As proposed by Wilson and Geankoplis, the mass transfer coefficient of reactants from bulk solution to electrode interface within porous medium is also proportional to the cube root of liquid flow rate at a low Reynold number [62-65]. Therefore, this unique dependence behavior of peak power density on the cube root of flow rate provides the second piece of evidence that for a paper-based microfluidic fuel cell with a given configuration, its performance is mainly determined by the mass transfer of reactants (e.g., O_2) from the bulk solution to the electrode-electrolyte interfaces. More insights about this unique dependence behavior are expected to be derived by conducting separate studies with the assistance of simulations. Nevertheless, this result points out for the first time that the performance of paper-based microfluidic fuel cells can be readily regulated by using paper channels with different textural properties, and a faster flow rate of electrolyte can result in higher peak power density of a microfluidic fuel cell, which benefits from the accelerated mass transfer of reactants to electrode surfaces.

Besides the peak power density, the open circuit voltage (OCV) was also found increased by using paper channels enabling higher flow rate, which cannot be directly correlated to the mass transfer properties. The OCV value of a fuel cell is sensitive to the fuel crossover from anolyte to catholyte which can be caused by either turbulent or diffusive mixing. In view of this, we made attempt to analyze the flow pattern quantitatively over different types of paper by introducing the Reynolds and Peclet numbers [42]. In the conventional pump-based microfluidic fuel cell, both Reynolds and Peclet numbers are determined by flow rate, channel geometry and electrolyte properties [19, 60]. As to a paper-based microfluidic fuel cell, the Reynolds and Peclet numbers of the electrolyte flow on paper can be calculated by taking account of the flow rate, paper properties and the electrolyte properties, which is detailed in

the Supporting Information. The calculation process is detailed in the Supporting Information. The results in **Table S5.2** imply that the Reynolds numbers are all far below 2000 which rules out existence of the turbulent flow. Therefore, the dependence behavior of OCV on the flow rate of electrolyte can only be ascribed to the diffusion induced fuel crossover [66]. To quantify the diffusion induced fuel crossover on different paper channels, the Peclet number which is defined as the ratio of advection flow to diffusion flow is determined, and a lower Peclet number usually indicates severer fuel crossover. Not surprisingly, the paper with higher Peclet number can always result in higher OCV values (**Table S5.2**). We tend to believe that the highest OCV obtained on the 417 paper based microfluidic fuel cell would likely benefit from its lowest fuel crossover. Furthermore, another attempt was made to directly visualize the fuel crossover of the bi-laminar flow on different filter papers. To achieve this, two dye solutions with different colors were used to mimic the flows of anolyte and catholyte on different paper channels. As shown in **Figure S5.11a**, a broader diffusion zone can always be observed on the paper with smaller pore size. Different from the 417 paper, on which the OCV and peak power density is almost independent on the electrode pair position (**Figure S5.4**) due to the narrow diffusion zone and the resultant limited fuel crossover, the paper with smaller pore diameter cannot efficiently suppress the fuel crossover as evidenced by the significantly broader diffusion zone and the fact that both OCV and peak power density are sensitive to the electrode pair position (**Figure S5.11b-c**).

Based on these evidence, we tend to believe that for a paper-based microfluidic fuel cell device, the textural property of paper channel materials which have long been overlooked by many studies, actually can be used as an effective regulator in controlling the overall fuel cell performance. In developing other high performing paper-based microfluidic fuel cells, it is favorable to select paper materials with large mean pore diameters, which can help minimize both the mass transfer resistance and fuel crossover effect by enabling a fast flow rate of electrolyte.

5.3.3 Toward practical applications

It can be found that as a miniaturized power source, a structurally optimized paper-based microfluidic fuel cell can exhibit a fairly high peak power (2.38 mW) among the paper-based microfluidic fuel cells (**Table S5.3**), and is even comparable to some microfluidic fuel cells using pumps to maintain the bi-laminar flow. Intrigued by its excellent performance, we

manage to demonstrate the potential capability of these paper-based microfluidic fuel cells for practical applications. By using these microfluidic fuel cell devices, continuous current ranging from 2 to ~6 mA can be expected for at least 1 h at the maximum power output, which can meet the energy requirements of many low power electronic devices, e.g., electrochemical glucometers and pregnancy test devices with digital display which typically require maximum currents of 1.1 and 4 mA, respectively, for a couple of seconds [8]; and single-use iontophoresis patches which requires a current output ranging from 1 to 4 mA for a treatment duration time of 20 − 40 min [67, 68].

However, the main drawback of these paper-based microfluidic fuel cells lies in their low voltage output. As presented above, the OCV value of a single device is lower than 0.9 V, and the maximum power can only be obtained at around 0.4 V regardless of the working electrode sizes, which is inadequate for some specific applications. For instance, a single paper-based fuel cell cannot power a low current LED, because the cell voltage cannot reach the threshold forward voltage of the LED and no current can flow through the diode. To tackle this problem, two solutions can be implemented. The first solution is to use a voltage boost converter (step-up DC-to-DC converter) which can boost the cell voltage from 0.13 up to 5.5 V [8]. As demonstrated by Zebda et al., they found that when a biofuel cell (voltage output: 0.3 to 0.6 V) was coupled with a voltage boost converter, it was capable to illuminate a LED (4.1 mA@2.9 V) [69]. Esquivel et al. demonstrated that by coupling with a voltage boost converter a micro fuel cell with nominal cell voltage of 0.186 V could provide a voltage output up to 3 V [70]. However, using voltage boost converters will add to the system cost, and may also cause intermittence in the power output [69]. The second solution is to connect several paper-based microfluidic fuel cells in series, which is demonstrated herein. The structure of the serial-connected cells are illustrated in the insert of **Figure 5.7a**, and three or more cells could be connected in a similar way. The V-I measurement in **Figure 5.7a** shows that the open circuit voltage (1.55 V) and the peak power (2.72 mW) are almost doubled on the serial connected two cells (electrode width: 10 mm). An even higher power output of 3.94 mW can be obtained over the serial-connected cells by using larger electrodes (electrode width: 15 mm), as shown in **Figure 5.7b**. Meanwhile, it can be observed that the average voltage and power for an individual cell in the serial-connected cells are lower than those for a single cell (**Figure 5.7**). This may arise from the parasitic internal circuit discharge caused by the electrolytic connection, which can be seen from **Figure S5.12** that part of the wetted

adsorbent pad are overlapped with each other [71]. Thus, there's still room left for achieving higher performance for the serial-connected cell, and structure optimization is needed to avoid any internal shunt current.

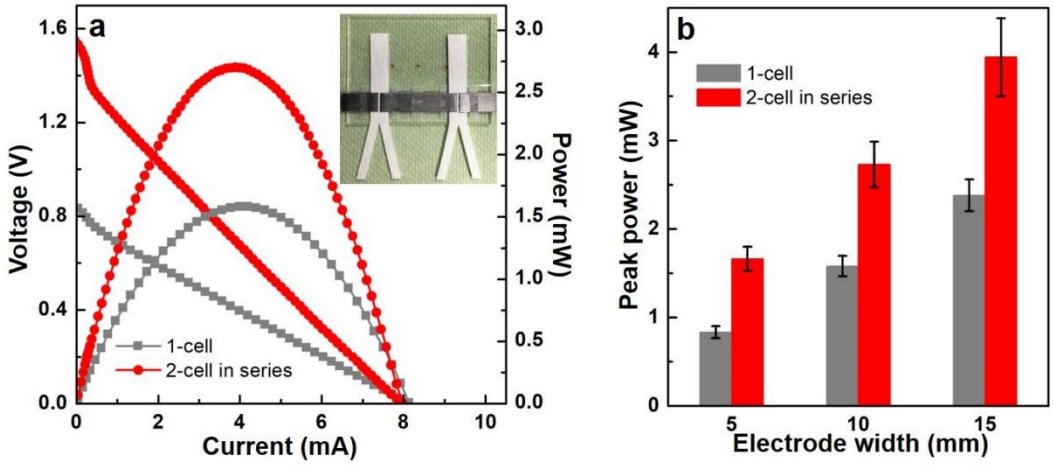

Figure 5.7 (a) Voltage-current measurement of a single paper-based microfluidic fuel cell and two cells connected in series. (Formate concentration: 4 M; KOH concentration: 1 M; EAA: 3×10 mm^2; Pd loading: 0.1 mg/cm^2; paper: VWR grade 417). The insert is the photo of two paper-based microfluidic fuel cell connected in series. (b) The peak power of a single cell and two cells in series with three different electrode sizes. (Formate concentration: 4 M; KOH concentration: 1 M; Pd loading: 0.1 mg/cm^2; EAA: 3×5, 3×10, 3×15 mm^2; paper: grade 417).

To demonstrate whether these paper-based microfluidic fuel cells can be used for practical applications, the serial-connected two cells (electrode width: 5 mm) were used as the power supply for a handheld calculator with a LCD display. We found that the self-made paper-based microfluidic fuel cell was sufficient to power a calculator and fulfill the power requirement to implement its full function (**Figure S5.12a**). To meet the voltage requirement of a LED (~3 V), we also connected four cells (electrode width: 10 mm) in a serial configuration, as shown in **Figure S5.12b-d**. The open circuit of the serial-connected four cells reaches 2.95 V **(Figure S5.12b)**, which makes it capable to continuously light 3 LED lamps (**Figure S5.12c**), and as a matter of fact, its high absolute power output allows it to light over 10 LED lamps at the same time (**Figure S5.12d**). These results have successfully demonstrated the great prospect of these paper-based microfluidic fuel cells to meet the power demand of portable low power electronic devices. The maximum power output can be further improved by constructing fuel cell stacks, to ensure theses paper-based microfluidic fuel cells

to be able to act as clean energy source for a wider range of electronic applications. At the same time, we have to admit that there's still great room left for us to further optimize the structure of these microfluidic fuel cells for practical applications. For instance, the volumetric power density (estimated as 0.238 mW/cm^3) of a single microfluidic fuel cell still needs to be improved, which is mainly due to the large volume of the electrolyte reservoirs (around 5 cm^3). To this end, a fuel cell integrated with solid redox species, which can be activated by adding water before use, holds great promise as already documented in some recent works [8, 38, 44].

5.4 Conclusions

In conclusion, low-cost and membrane-less paper-based microfluidic fuel cells were successfully fabricated. By comprehensively investigating the influences from the structures/components of paper-based microfluidic fuel cells, several key parameters including paper pore structure, electrode position, concentrations of fuel, oxidant and supporting electrolyte have been identified and optimized toward best practices for developing high-performing microfluidic fuel cells. Main influence on the performance of a microfluidic fuel cell is identified as the reactant depletion along the electrode for low reactant concentration and flow rates (which correlate with the paper pore structure) and the mass transfer limitation through the catalyst film for high catalyst concentration. Technically, an OCV of 0.86 V and a peak power density of 7.10 mW/cm^2 were achieved on a single paper-based microfluidic fuel cell and the maximum power output can be sustained for at least 1 h. The open circuit voltage and the output power could be further improved by connecting cells in series, which makes the paper-based microfluidic fuel cell able to power some small devices. We believe these results would also have wide implications for developing other more efficient paper-based microfluidic devices for energy storage/conversion, diagnosis and/or sensing applications.

References

[1] C. K. Dyer, J. Power Sources 106 (2002) 31-34.

[2] S. A. M. Shaegh, N.-T. Nguyen, S.H. Chan, Int. J. Hydrogen Energy 36 (2011) 5675-5694.

[3] N. K. Thom, K. Yeung, M. B. Pillion, S.T. Phillips, Lab Chip 12 (2012) 1768-1770.

[4] M. Safdar, J. Jänis, S. Sanchez, Lab Chip 16 (2016) 2754-2758.

[5] S. Chou, W. Yang, K. Chua, J. Li, K. Zhang, Appl. Energ. 88 (2011) 1-16.

[6] D. A. Notter, M. Gauch, R. Widmer, P. Wager, A. Stamp, R. Zah, H.-J.r. Althaus, Environ. Sci. Technol. 44 (2010) 6550-6556.

[7] M. Cabral, F. Pedrosa, F. Margarido, C. Nogueira, Environ. Technol. 34 (2013) 1283-1295.

[8] J. Esquivel, F. Del Campo, J. G. de la Fuente, S. Rojas, N. Sabate, Energ. Environ. Sci. 7 (2014) 1744-1749.

[9] S. Srinivasan, O. A. Velev, A. Parthasarathy, D. J. Manko, A. J. Appleby, J. Power Sources 36 (1991) 299-320.

[10] Y. Zhu, S. Y. Ha, R.I. Masel, J. Power Sources 130 (2004) 8-14.

[11] A. Khaligh, Z. Li, IEEE Trans. Veh. Technol. 59 (2010) 2806-2814.

[12] M.-A. Goulet, E. Kjeang, J. Power Sources 260 (2014) 186-196.

[13] O. A. Ibrahim, M.-A. Goulet, E. Kjeang, Electrochim. Acta 187 (2016) 277-285.

[14] R. F. Ismagilov, A. D. Stroock, P. J. Kenis, G. Whitesides, H. A. Stone, Appl. Phys. Lett. 76 (2000) 2376-2378.

[15] M.-H. Chang, F. Chen, N.-S. Fang, J. Power Sources 159 (2006) 810-816.

[16] M. Sun, G. V. Casquillas, S. Guo, J. Shi, H. Ji, Q. Ouyang, Y. Chen, Microelectron. Eng. 84 (2007) 1182-1185.

[17] J. L. Osborn, B. Lutz, E. Fu, P. Kauffman, D. Y. Stevens, P. Yager, Lab Chip 10 (2010) 2659-2665.

[18] R. Ferrigno, A. D. Stroock, T. D. Clark, M. Mayer, G. M. Whitesides, J. Am. Chem. Soc. 124 (2002) 12930-12931.

[19] E. R. Choban, L. J. Markoski, A. Wieckowski, P. J. Kenis, J. Power Sources 128 (2004) 54-60.

[20] R. S. Jayashree, L. Gancs, E. R. Choban, A. Primak, D. Natarajan, L. J. Markoski, P. J. Kenis, J. Am. Chem. Soc. 127 (2005) 16758-16759.

[21] E. Kjeang, R. Michel, D. A. Harrington, N. Djilali, D. Sinton, J. Am. Chem. Soc. 130 (2008) 4000-4006.

[22] J. L. Cohen, D. J. Volpe, D. A. Westly, A. Pechenik, H. D. Abruña, Langmuir 21 (2005) 3544-3550.

[23] E. Kjeang, J. McKechnie, D. Sinton, N. Djilali, J. Power Sources 168 (2007) 379-390.

[24] W. Sung, J.-W. Choi, J. Power Sources 172 (2007) 198-208.

[25] F. R. Brushett, R. S. Jayashree, W.-P. Zhou, P. J. Kenis, Electrochim. Acta 54 (2009) 7099-7105.

[26] D. Morales-Acosta, L.A. Godinez, L. Arriaga, J. Power Sources 195 (2010) 1862-1865.

[27] A. S. Gago, Y. Gochi-Ponce, Y. J. Feng, J. P. Esquivel, N. Sabaté, J. Santander, N. Alonso-Vante, ChemSusChem 5 (2012) 1488-1494.

[28] M. R. Thorson, F. R. Brushett, C. J. Timberg, P. J. Kenis, J. Power Sources 218 (2012) 28-33.

[29] M.-A. Goulet, O. A. Ibrahim, W. H. Kim, E. Kjeang, J. Power Sources 339 (2017) 80-85.

[30] M. J. González-Guerrero, F. J. del Campo, J. P. Esquivel, F. Giroud, S. D. Minteer, N. Sabaté, J. Power Sources 326 (2016) 410-416.

[31] T. S. Copenhaver, K. H. Purohit, K. Domalaon, L. Pham, B. J. Burgess, N. Manorothkul, V. Galvan, S. Sotez, F. A. Gomez, J. L. Haan, Electrophoresis 36 (2015) 1825-1829.

[32] T. H. Nguyen, A. Fraiwan, S. Choi, Biosens. Bioelectron. 54 (2014) 640-649.

[33] V. Galvan, K. Domalaon, C. Tang, S. Sotez, A. Mendez, M. Jalali-Heravi, K. Purohit, L. Pham, J. Haan, F. A. Gomez, Electrophoresis 37 (2016) 504-510.

[34] L.-L. Shen, G.-R. Zhang, W. Li, M. Biesalski, B. J. Etzold, ACS Omega 2 (2017) 4593-4603.

[35] H. Lee, S. Choi, Nano Energy 15 (2015) 549-557.

[36] C. Chen, Y. Zhang, Y. Li, J. Dai, J. Song, Y. Yao, Y. Gong, I. Kierzewski, J. Xie, L. Hu, Energ. Environ. Sci. 10 (2017) 538-545.

[37] J. Esquivel, J. Buser, C. Lim, C. Domínguez, S. Rojas, P. Yager, N. Sabaté, J. Power Sources 342 (2017) 442-451.

[38] J. P. Esquivel, P. Alday, O. A. Ibrahim, B. Fernández, E. Kjeang, N. Sabaté, Adv. Energy Mater. 7 (2017) 1700275.

[39] N. Walji, B. D. MacDonald, Micromachines 7 (2016) 73.

[40] M. K. Rashed, M. Salleh, M. Amran, H. A. Abdulbari, M. H. Shah Ismail, S. Izhar, ChemBioEng Rev. 2 (2015) 356-372.

[41] M. Tanveer, K.-Y. Kim, Energy Convers. Manage. 136 (2017) 372-381.

[42] A. Böhm, F. Carstens, C. Trieb, S. Schabel, M. Biesalski, Microfluid. Nanofluid. 16 (2014) 789-799.

[43] S. Mendez, E. M. Fenton, G. R. Gallegos, D. N. Petsev, S. S. Sibbett, H. A. Stone, Y. Zhang, G. P. López, Langmuir 26 (2009) 1380-1385.

[44] O. A. Ibrahim, P. Alday, N. Sabaté, J. P. Esquivel, E. Kjeang, J. Electrochem. Soc. 164 (2017) A2448-A2456.

[45] E. Kjeang, N. Djilali, D. Sinton, J. Power Sources 186 (2009) 353-369.

[46] E. Elizalde, R. Urteaga, C. L. Berli, Lab Chip 15 (2015) 2173-2180.

[47] K. Chaudhury, S. Kar, S. Chakraborty, Appl. Phys. Lett. 109 (2016) 224101.

[48] Y. Bing, H. Liu, L. Zhang, D. Ghosh, J. Zhang, Chem. Soc. Rev. 39 (2010) 2184-2202.

[49] L. Lin, Q. Zhu, A.-W. Xu, J. Am. Chem. Soc. 136 (2014) 11027-11033.

[50] G.-R. Zhang, M. Munoz, B. J. Etzold, Angew. Chem. Int. Ed. 55 (2016) 2257-2261.

[51] G.-R. Zhang, T. Wolker, D. J. Sandbeck, M. Munoz, K. J. Mayrhofer, S. Cherevko, B. J. Etzold, ACS Catal. 8 (2018) 8244-8254.

[52] G.-R. Zhang, S. Wöllner, Appl. Catal. B-Environ. 222 (2018) 26-34.

[53] J. R. Varcoe, P. Atanassov, D. R. Dekel, A. M. Herring, M.A. Hickner, P.A. Kohl, A.R. Kucernak, W. E. Mustain, K. Nijmeijer, K. Scott, Energ. Environ. Sci. 7 (2014) 3135-3191.

[54] G. Merle, M. Wessling, K. Nijmeijer, J. Membr. Sci. 377 (2011) 1-35.

[55] I. Martinaiou, T. Wolker, A. Shahraei, G.-R. Zhang, A. Janßen, S. Wagner, N. Weidler, R. W. Stark, B. J. M. Etzold, U. I. Kramm, J. Power Sources 375 (2018) 222-232.

[56] H. A. Gasteiger, S. S. Kocha, B. Sompalli, F. T. Wagner, Appl. Catal. B-Environ. 56 (2005) 9-35.

[57] W. Jin, H. Du, S. Zheng, H. Xu, Y. Zhang, J. Phys. Chem. B 114 (2010) 6542-6548.

[58] H. A. Miller, J. Ruggeri, A. Marchionni, M. Bellini, M. V. Pagliaro, C. Bartoli, A. Pucci, E. Passaglia, F. Vizza, Energies 11 (2018) 369.

[59] S. Hasegawa, K. Shimotani, K. Kishi, H. Watanabe, Electrochem. Solid-State Lett. 8 (2005) A119-A121.

[60] A. Li, S.H. Chan, N.-T. Nguyen, J. Micromech. Microeng. 17 (2007) 1107.

[61] B. M. Cummins, R. Chinthapatla, F. S. Ligler, G. M. Walker, Anal. Chem. 89 (2017) 4377-4381.

[62] E. Wilson, C. Geankoplis, Ind. Eng. Chem. Fundam. 5 (1966) 9-14.

[63] R. M. Darling, M. L. Perry, J. Electrochem. Soc. 161 (2014) A1381-A1387.

[64] J. D. Milshtein, K. M. Tenny, J. L. Barton, J. Drake, R. M. Darling, F. R. Brushett, J. Electrochem. Soc. 164 (2017) E3265-E3275.

[65] R. M. Darling, H.-S. Shiau, A. Z. Weber, M. L. Perry, J. Electrochem. Soc. 164 (2017) E3081-E3091.

[66] S. K. Yoon, G. W. Fichtl, P. J. Kenis, Lab Chip 6 (2006) 1516-1524.

[67] S. H. Roy, S.L. Wolf, D. A. Scalzitti, The Rehabilitation Specialist's Handbook, FA Davis, 2012.

[68] Iontophoresis. http://www.electrotherapy.org/modality/iontophoresis.

[69] A. Zebda, S. Cosnier, J.-P. Alcaraz, M. Holzinger, A. Le Goff, C. Gondran, F. Boucher, F. Giroud, K. Gorgy, H. Lamraoui, Sci. Rep. 3 (2013) 1516.

[70] J. Esquivel, J. Colomer-Farrarons, M. Castellarnau, M. Salleras, F. Del Campo, J. Samitier, P. Miribel-Catala, N. Sabate, Lab Chip 12 (2012) 4232-4235.

[71] O. A. Ibrahim, M.-A. Goulet, E. Kjeang, J. Electrochem. Soc. 162 (2015) F639-F644.

Supporting Information

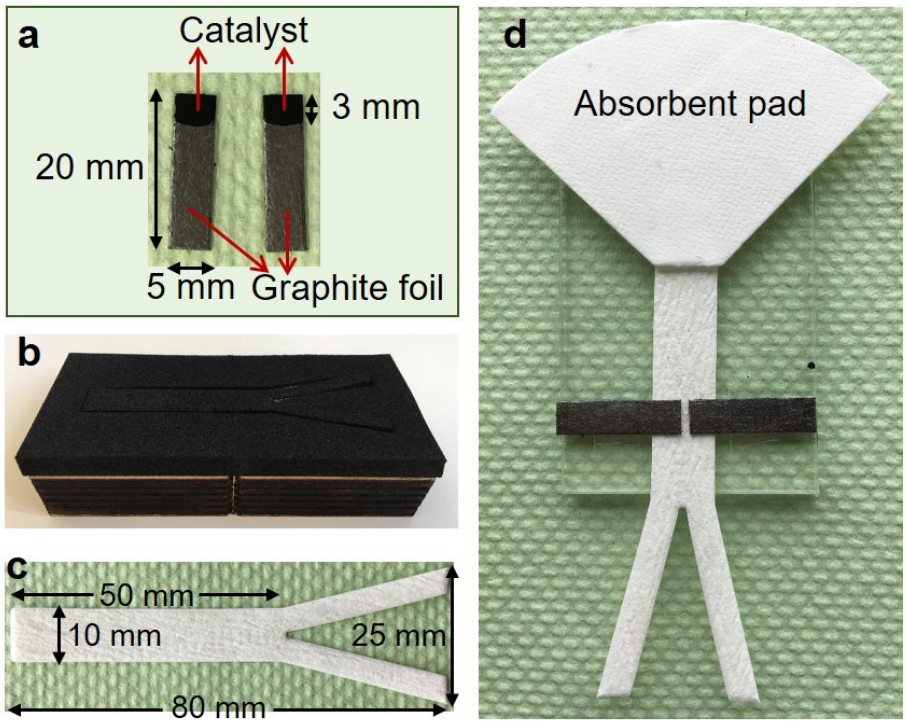

Figure S5.1 Dimensions of the paper-based microfluidic fuel cell. (a) Catalyst coated electrodes; (b) The die for cutting Y-shaped paper channels; (c) Y-shaped paper channel; (d) Paper-based microfluidic fuel cell with a fan-shaped absorbent pad at the end of the paper channel.

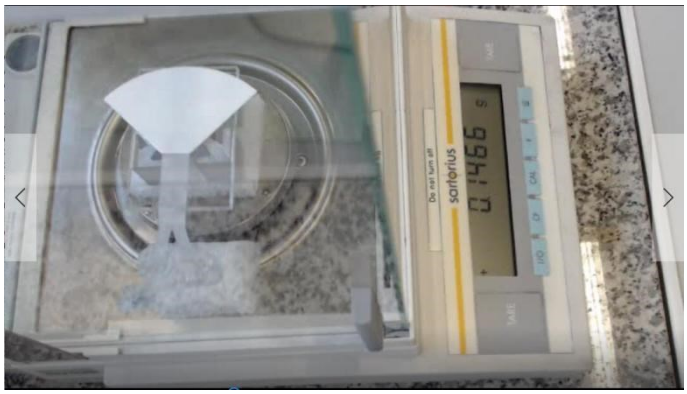

Figure S5.2 Flow rate was measured by using a balance. The weight gain of the absorbent pad can be read from the balance. The balance is tared immediately after the flow front reaching the absorbent pad.

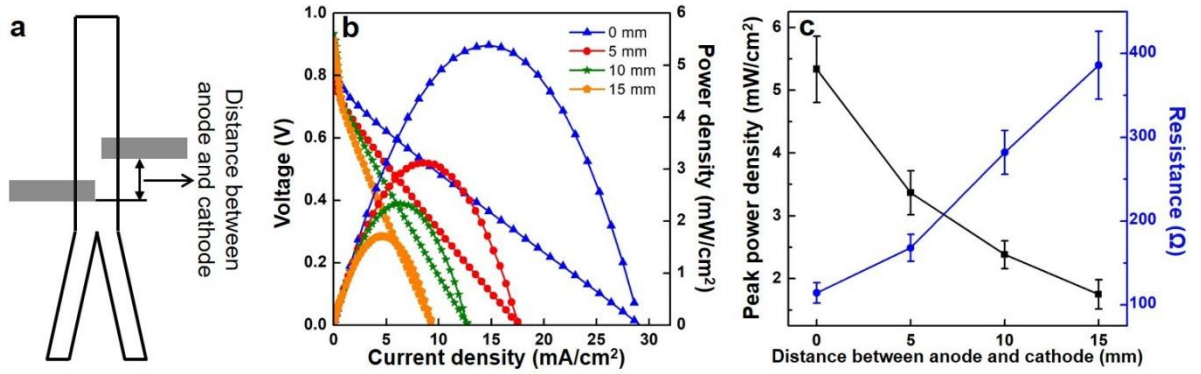

Figure S5.3 (a) Definition of the distance between the anode and cathode electrode. (b) Voltage-current measurement of the paper-based microfluidic fuel cell with different anode and cathode distance. (c) Peak power density and cell resistance of the paper-based microfluidic fuel cell with different anode and cathode distance. (KOH concentration: 1 M; formate concentration: 2 M; EAA: 3×5 mm^2; Pd loading: 0.1 mg/cm^2; paper: VWR grade 417).

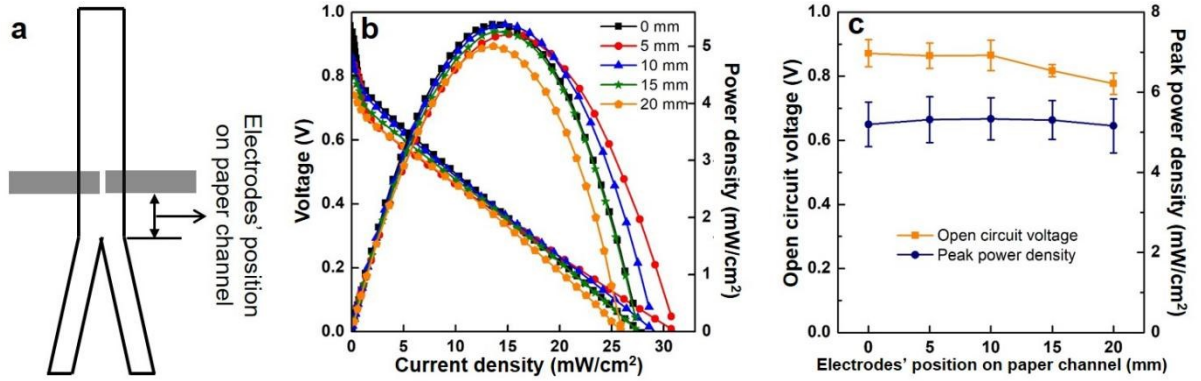

Figure S5.4 (a) Definition of the electrodes' position on paper channel. (b) Voltage-current measurement of the paper-based microfluidic fuel cell with different electrodes' position. (c) Open circuit voltage and peak power density of the paper-based microfluidic fuel cell with different electrodes' position. (KOH concentration: 1 M; formate concentration: 2 M; EAA: 3×5 mm^2; Pd loading: 0.1 mg/cm^2; paper: VWR grade 417).

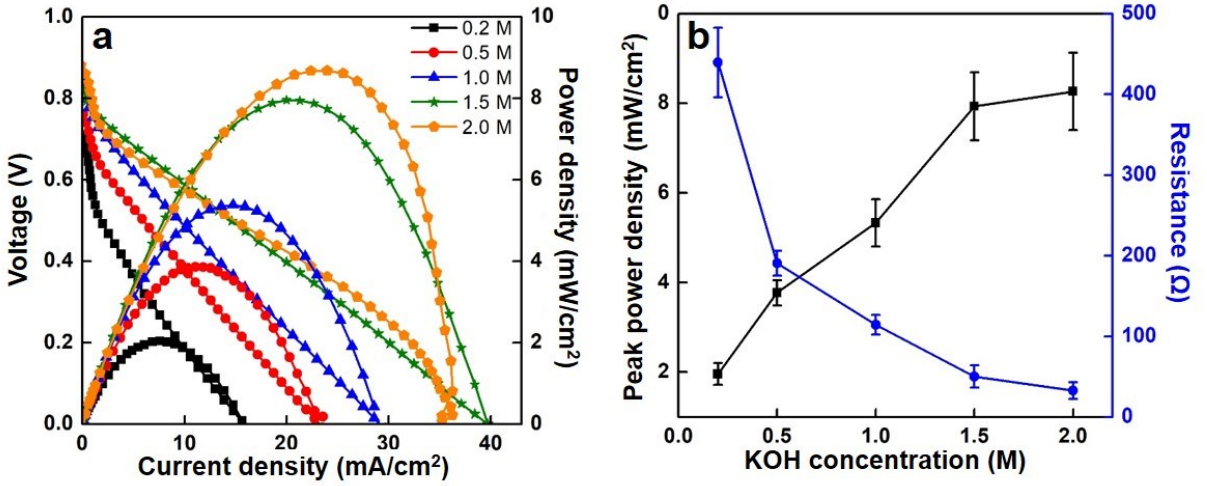

Figure S5.5 (a) Voltage-current measurement of paper-based microfluidic fuel cell under different KOH concentration. (b) Influence of KOH concentration on the peak power density and cell resistance. (Formate concentration: 2 M; EAA: 3×5 mm^2; Pd loading: 0.1 mg/cm^2; paper: VWR grade 417).

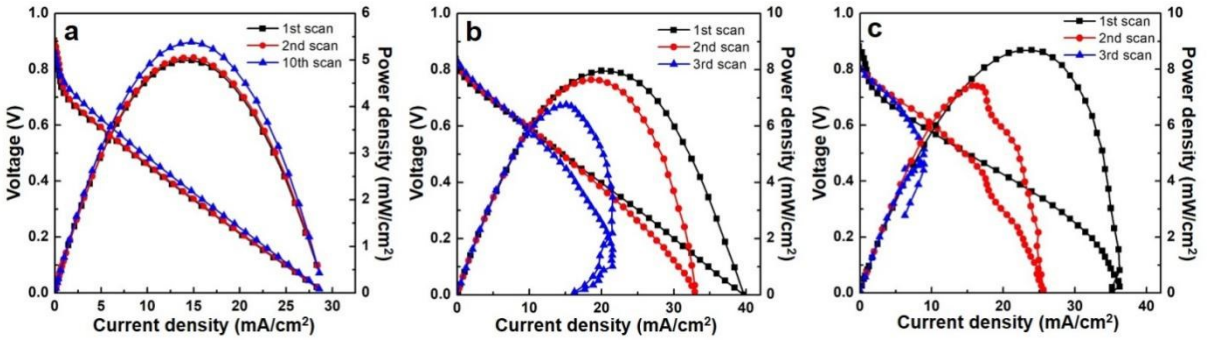

Figure S5.6 Voltage-current measurement of paper-based microfluidic fuel cell with 1 M (a), 1.5 M (b) and 2 M (c) KOH solution by continuous scan. (Formate concentration: 2 M; EAA: 3×5 mm^2; Pd loading: 0.1 mg/cm^2; paper: VWR grade 417).

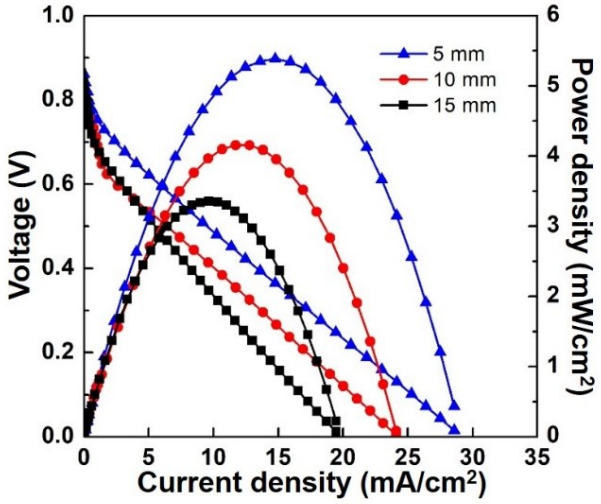

Figure S5.7 Voltage-current measurement of paper-based microfluidic fuel cell at different electrode size under 2 M formate solution. (KOH concentration: 1 M; Pd loading: 0.1 mg/cm^2; EAA: 3×5, 3×10, 3×15 mm^2; paper: VWR grade 417).

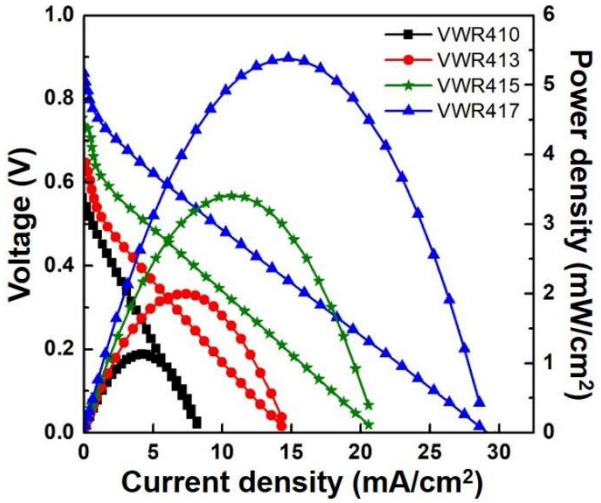

Figure S5.8 Voltage-current measurement of the paper-based fuel cell with four types of paper channel. (Formate concentration: 2 M; KOH concentration: 1 M; EAA: 3×5 mm^2; Pd loading: 0.1 mg/cm^2)

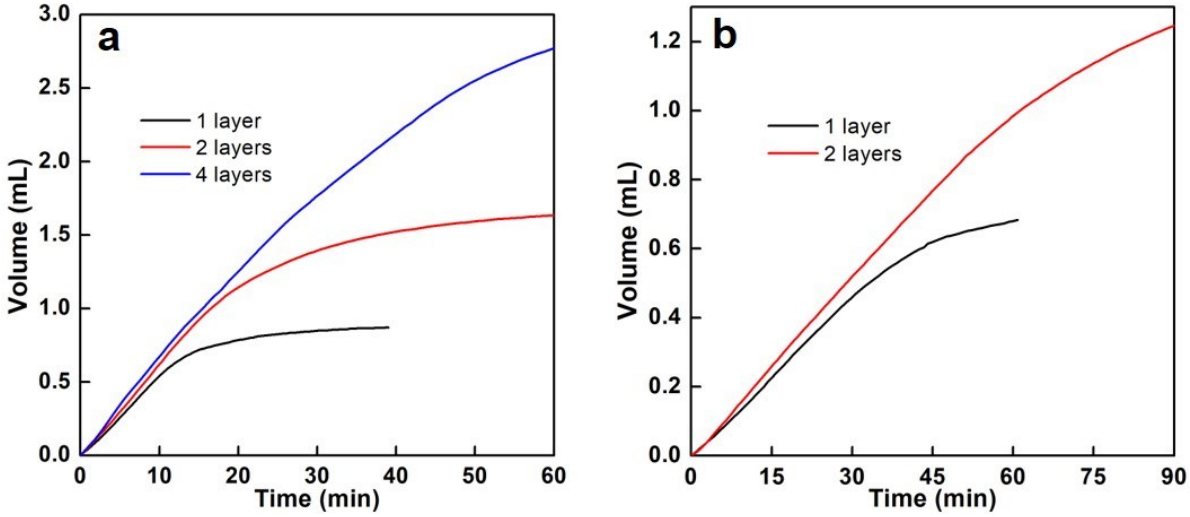

Figure S5.9 Flow rate measurement of VWR grade 417 (a) and grade 415 (b) by using different layer of absorbent pad. (Formate concentration: 2 M; KOH concentration: 1 M).

Table S5.1 Linear regression equations of flow rates vs. time on VWR paper channels

Paper	Fitting equation	R^2
Grade 410	$y = 0.0074 + 0.0012x$	0.958
Grade 413	$y = -0.019 + 0.0056x$	0.996
Grade 415	$y = 0.0063 + 0.017x$	0.999
Grade 417	$y = 0.052 + 0.059x$	0.997

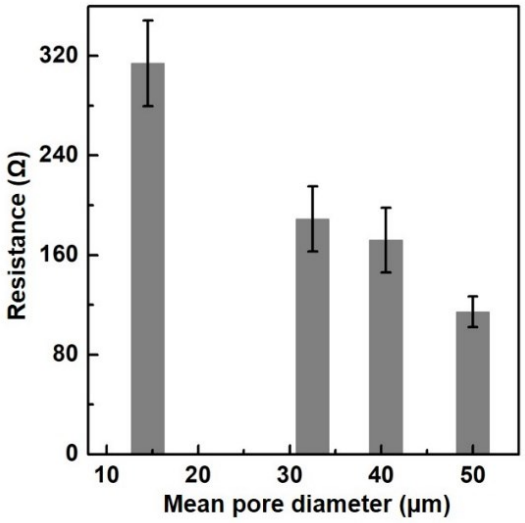

Figure S5.10 Cell resistance measured by AC impedance on microfluidic fuel cell with four types of filter paper.

Calculation of Reynolds number and Peclet number

The fuel crossover on a microfluidic fuel cell device can be triggered by turbulent flow of the anolyte stream. To investigate the flow pattern of electrolyte over different types of paper, we calculated the Reynolds numbers for different paper channels, which is defined as the ratio of inertial force to viscous force and can be used to distinguish the laminar flow from turbulent flow. The Reynolds number is defined as:

$$Re = \frac{\rho v L}{\mu} \quad \textbf{(S5.1)}$$

where ρ is the density (kg/m^3), v is the flow velocity (m/s), L is the characteristic length (m), μ is the viscosity (Pa·s) [1]. The flow velocity (m/s) can be obtained from the measured volume flow rate by the following equation:

$$v = \frac{u}{wh\varphi} \quad \textbf{(S5.2)}$$

where u is the volume flow rate (m^3/s), w is the paper channel width (m), h is the paper thickness (m), φ is the porosity. The results are summarized in **Table S5.1**. Despite the difference over different paper channels, it seems that the Reynolds numbers are all sufficiently low to ensure typical laminar flows. Therefore, we can rule out the possibility that fuel crossover is caused by the uncontrolled turbulent flow. While by revisiting the working principle of microfluidic fuel cells, we can learn that for a co-laminar flow fuel cell device, electrolyte diffusion would occur at the interfaces between anolyte and catholyte regardless of their flow patterns. Then the question lies in how to evaluate the diffusion rate at the interfaces of anolyte and catholyte. To achieve this, the Peclet numbers, which defined as the ratio of advection transport rate to diffusive transport rate, were determined for different paper channels and listed in **Table S5.1**.

The Peclet number is defined as:

$$Pe = \frac{vL}{D} \quad \textbf{(S5.3)}$$

where, v is the flow velocity (m/s), L is the characteristic length (m), D is the mass diffusion coefficient (m^2/s) [1, 2]. In the paper-based microfluidic system, the advection flow refers to the fuel and oxidant solution flow in parallel along the paper channel, and generate electricity

power by redox reaction at the anode and cathode electrode. The diffusion flow refers to the diffusion of KCOOH from anode to cathode side, which causes power loss in the fuel cell.

The Peclet number of the flow on grade 417 paper (26.3) is higher than 10, indicating that the advection dominates in the flow. However, the Peclet numbers of flow on grade 410 paper (0.34), 413 paper (2.76) and 415 paper (4.69) are ranging from 0.1 to 10, indicating that both the advection or the diffusion take effect, the lower the Peclet number, the severer the fuel crossover and the lower OCV values.

Table S5.2 Summary of the flow rate, the Reynolds number and the Peclet number

Paper	Characteristic length[a] (μm)	Thickness (μm)	Mean Porosity (%)	Flow rate (μL/min)	Reynolds number[b]	Peclet number
VWR410	14.5	150	22.5	1.18	0.00090	0.34
VWR413	32.5	160	27	5.56	0.0073	2.76
VWR415	40.5	160	60	16.8	0.012	4.69
VWR417	50	147	50	59.3	0.070	26.3

[a] Characteristic length is equivalent to the mean pore diameter.

[b] $\rho_{KOH} = 1.049\ \mathrm{g/cm^3}$, $\mu_{KOH} = 1005\ \mathrm{pa \cdot s}$, $D = 2546\ \mu\mathrm{m^2/s}$ [3, 4]

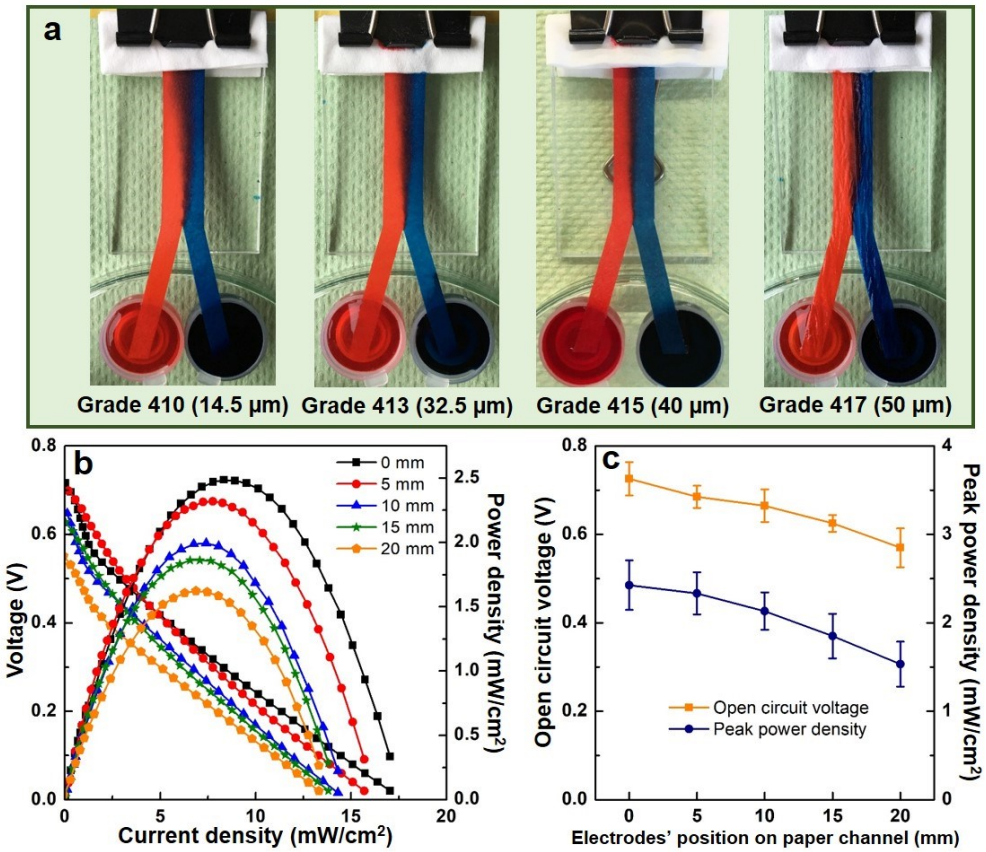

Figure S5.11 (a) Cross diffusion over four types of filter paper grade illustrated by dye solutions (red: coccine, blue: indigo carmine). The average pore diameter is shown in the brackets. (b) Voltage-current measurement of the paper-based microfluidic fuel cell with different electrodes' position. (c) Open circuit voltage and peak power density of the paper-based microfluidic fuel cell with different electrodes' position. (KOH concentration: 1 M; formate concentration: 2 M; EAA: 3×5 mm^2; Pd loading: 0.1 mg/cm^2; paper: VWR grade 413)

Table S5.3 Comparisons of the microfluidic fuel cells

Anode Cathode	Anode fuel	Cathode oxidant	Flow rate[a] (mL/min)	OCP (V)	P_{max} (mW/cm^2)	I @ P_{max} (mA/cm^2)	P_{max} (mW)	Ref.
Carbon-on-gold electrode Carbon-on-gold electrode	1 M V^{2+} in 25% H_2SO_4	1 M VO_2^+ in 25% H_2SO_4	1.5	1.57	38	35	0.32	[5]
			0.004	1.59	3.1	3.5	0.026	
Pt black Pt black	2.1 M HCOOH	0.144 M $KMnO_4$ 0.5 M H_2SO_4	0.5	1.1	2.4	4		[6]
	2.1 M HCOOH	0.5 M H_2SO_4		0.7	0.17	0.4		
Pt on Kapton electrode Pt on Kapton electrode	H_2 saturated in 0.1 M KOH	O_2 saturated in 0.1 M H_2SO_4	4	1.45	0.75	0.85	0.375	[7]
10 mg/cm^2 Pd 2 mg/cm^2 Pt	1 M KCOOH 0.5 M H_2SO_4	0.5 M H_2SO_4	0.3	0.9	26	95	16.1	[8]
Graphite rods Graphite rods	2 M V^{2+} 2 M H_2SO_4	2 M VO_2^+ 2 M H_2SO_4	0.3	1.42	35	45	5.8	[9]
2 µm Ni(OH)2 2 µm AgO on Au	2 M CH_3OH 0.2 M KOH 0.05 M H_2O_2	2 M CH_3OH 0.2 M KOH 0.05 M H_2O_2	0.2	0.1	0.028	0.8	0.032	[10]
Porous carbon Porous carbon	2 M V^{2+} 4 M H_2SO_4	2 M VO_2^+ 4 M H_2SO_4	0.3	1.53	131	150	15.7	[11]
			0.001	1.52	20	25	2.4	
10 mg/cm^2 Pd black 2 mg/cm^2 Pt black	1 M KCOOH 0.5 M H_2SO_4	0.5 M H_2SO_4	0.3	0.9	27	100	17.8	[12]
10 mg/cm^2 Pt/Ru black 2 mg/cm^2 Pt black	1 M CH_3OH 1 M KOH	1 M KOH		0.7	17.2	60	11.4	
	1 M CH_3OH 0.5 M H_2SO_4	0.5 M H_2SO_4		0.7	12.5	40	8.25	
1.3 mg/cm^2 Pd/MWCNT[b] 1.9 mg/cm^2 Pt/C	0.1 M KCOOH 0.5 M H_2SO_4	O_2 saturated in 0.5 M H_2SO_4	0.2	0.9	3.3	7.6	1.49	[13]
2 mg/cm^2 Pt/Ru alloy 2 mg/cm^2 Pt/C	2 M CH_3OH 1 M KOH	1 M KOH	0.1	0.65	25	120	1.56	[14]
					15	45	7.5	
6 mg/cm^2 PtRu 2 mg/cm^2 Pt_xS_y	5 M CH3OH 0.5 M H_2SO_4	0.5 M H_2SO_4	anode: 12.6 cathode: 14.2	0.93	4	35	4	[15]
1 mg/cm^2 PtRu/C 1 mg/cm^2 Pt/C	0.5 M CH_3OH 1 M KOH	1 M KOH	2.1	0.47	0.97	6.9	0.87	[16]
	1 M CH_3OH 1 M KOH	2 M H_2O_2 1 M KOH	0.9	0.68	3.8	18.8	3.4	
MWCNT[b] MWCNT[b]	1 M V^{2+} 4 M H_2SO_4	1 M VO_2^+ 4 M H_2SO_4	0.2	1.55	2010	2530	30.1	[17]
Hb-pencil stroked graphite electrode	1 M KCOOH	3.75 M H_2SO_4	Wattman paper	0.33	32	325	12	[18]
1 mg/cm^2 PtRu/C on Au/COP 1 mg/cm^2 Pt/C on carbon paper	4 M CH_3OH 2 M KOH	2 M KOH	0.08 Whatman fusion 5	0.55	4.4	22.5	0.44	[19]
	4 M CH_3OH 1 M KOH	1 M KOH		0.55	3.2	15.5	0.33	
0.2 mg/cm^2 Pd/C graphite	5 M KCOOH 1 M KOH	30% H_2O_2 0.5 M KCl	Whatman grade 3	0.63	0.45	1.5	0.45	[20]
0.3 mg/cm^2 glucose oxidase 6.3 mg/cm^2 laccase/MWCNT[b]	0.1 M glucose Phosphate buffer, pH=7.4	Phosphate buffer, pH=4.5	0.02-0.03 Whatman fusion 5	0.6	0.32	0.045	0.032	[21]

1.5 mg/cm^2 Pd/C on steel mesh Carbon on steel mesh	5 M KCOOH 0.5 M KCl	30% H_2O_2 0.5 M KCl	Whatman grade 1	1.1	2.53	5.5	0.51	[22]
1 mg/cm^2 Pt/C 1 mg/cm^2 Pt/C	H_2 KOH	O_2 KOH	CF10, GE Healthcare	1.0	103	230	25.8	[23]
Porous carbon paper Porous carbon paper	pBQ[d] OA[d] (solid state)	H_2BQS[d] KOH (solid state)	Ahlstrom	0.8	6.8	18.9	1.7	[24]
Porous carbon paper Porous carbon paper	5.4 mg pBQ[d] 22.5 mg OA[d] (solid state)	8.8 mg AA[d] 28 mg KOH (solid state)	Ahlstrom	1.1	7.6	18	1.9	[25]
0.1 mg/cm^2 Pd/C on graphite foil (0.45 cm^2) 0.1 mg/cm^{-2} Pd/C on graphite foil (0.45 cm^2)	4M KCOOH 1M KOH	1M KOH	0.03[c] VWR grade 417	0.86	5.33	15.0	2.38	this work
0.2 mg/cm^2 Pd/C on graphite foil (0.15 cm^2) 0.2 mg/cm^{-2} Pd/C on graphite foil (0.15 cm^2)				0.88	7.10	17.0	1.07	

[a]The microfluidic fuel cells using pumps are shown in black text (Ref 5-17), while those using paper via capillary action are shown in blue text (Ref 18-25), and the paper type is also listed in the table.

[b]MWCNT: Multi-walled carbon nanotube

[c]Assuming the flow rate of anolyte and catholyte are the same, the flow rate of on each side is 0.03 mL/min.

[d]pBQ: p-benzoquinone; OA: oxalic acid; H_2BQS: hydoquinonesulfonic acid potassium salt; AA: ascorbic acid

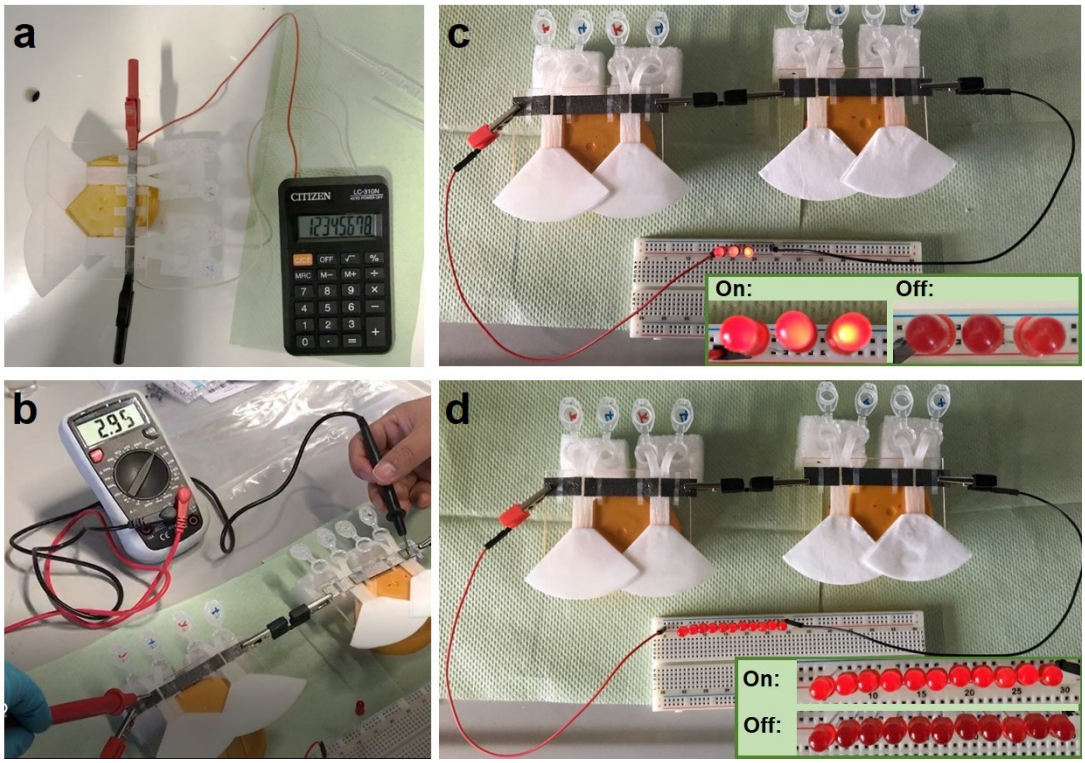

Figure S5.12 (a) Two-cell connected in series powers a calculator. (KOH concentration: 1 M; formate concentration: 2 M; EAA: 3×5 mm^2; Pd loading: 0.1 mg/cm^2; paper: VWR grade 417). (b) Measurement of the open circuit voltage of four cells in series by a voltmeter. (KOH concentration: 1 M; formate concentration: 4 M; EAA: 3×10 mm^2; Pd loading: 0.1 mg/cm^2; paper: VWR grade 417). Four cells in series power 3 LED lamps (c) and 11 LED lamps (d). (KOH concentration: 1 M; Formate concentration: 4 M; EAA: 3×10 mm^2; Pd loading: 0.1 mg/cm^2; paper: VWR grade 417)

References

[1] A. Böhm, F. Carstens, C. Trieb, S. Schabel, M. Biesalski, Microfluid. Nanofluid. 16 (2014) 789-799.

[2] A. Li, S.H. Chan, N.-T. Nguyen, J. Micromech. Microeng. 17 (2007) 1107.

[3] F. Chen, M.-H. Chang, M.-K. Lin, Electrochim. Acta 52 (2007) 2506-2514.

[4] Y.-J. Guo, H.-B. Xu, G. Fen, S.-L. Zheng, Y. Zhang, Trans. Nonferrous Met. Soc. China 20 (2010) s32-s36.

[5] R. Ferrigno, A. D. Stroock, T. D. Clark, M. Mayer, G. M. Whitesides, J. Am. Chem. Soc. 124 (2002) 12930-12931.

[6] E. R. Choban, L. J. Markoski, A. Wieckowski, P.J. Kenis, J. Power Sources 128 (2004) 54-60.

[7] J. L. Cohen, D. J. Volpe, D.A. Westly, A. Pechenik, H.D. Abruña, Langmuir 21 (2005) 3544-3550.

[8] R. S. Jayashree, L. Gancs, E. R. Choban, A. Primak, D. Natarajan, L. J. Markoski, P. J. Kenis, J. Am. Chem. Soc. 127 (2005) 16758-16759.

[9] E. Kjeang, J. McKechnie, D. Sinton, N. Djilali, J. Power Sources 168 (2007) 379-390.

[10] W. Sung, J.-W. Choi, J. Power Sources 172 (2007) 198-208.

[11] E. Kjeang, R. Michel, D. A. Harrington, N. Djilali, D. Sinton, J. Am. Chem. Soc. 130 (2008) 4000-4006.

[12] F. R. Brushett, R. S. Jayashree, W.-P. Zhou, P. J. Kenis, Electrochim. Acta 54 (2009) 7099-7105.

[13] D. Morales-Acosta, L. A. Godinez, L. Arriaga, J. Power Sources 195 (2010) 1862-1865.

[14] M. R. Thorson, F. R. Brushett, C. J. Timberg, P. J. Kenis, J. Power Sources 218 (2012) 28-33.

[15] A. S. Gago, Y. Gochi-Ponce, Y. J. Feng, J. P. Esquivel, N. Sabaté, J. Santander, N. Alonso-Vante, ChemSusChem 5 (2012) 1488-1494.

[16] A. K. Rathoure, H. Pramanik, Int. J. Hydrogen Energy 41 (2016) 15287-15294.

[17] M.-A. Goulet, O. A. Ibrahim, W. H. Kim, E. Kjeang, J. Power Sources 339 (2017) 80-85.

[18] R. K. Arun, S. Halder, N. Chanda, S. Chakraborty, Lab Chip 14 (2014) 1661-1664.

[19] J. Esquivel, F. Del Campo, J. G. de la Fuente, S. Rojas, N. Sabaté, Energ. Environ. Sci. 7 (2014) 1744-1749.

[20] T. S. Copenhaver, K. H. Purohit, K. Domalaon, L. Pham, B. J. Burgess, N. Manorothkul, V. Galvan, S. Sotez, F. A. Gomez, J. L. Haan, Electrophoresis 36 (2015) 1825-1829.

[21] M. J. González-Guerrero, F. J. del Campo, J. P. Esquivel, F. Giroud, S. D. Minteer, N. Sabaté, J. Power Sources 326 (2016) 410-416.

[22] V. Galvan, K. Domalaon, C. Tang, S. Sotez, A. Mendez, M. Jalali-Heravi, K. Purohit, L. Pham, J. Haan, F. A. Gomez, Electrophoresis 37 (2016) 504-510.

[23] S. Hashemi, M. Neuenschwander, P. Hadikhani, M. Modestino, D. Psaltis, J. Power Sources 348 (2017) 212-218.

[24] J. P. Esquivel, P. Alday, O. A. Ibrahim, B. Fernández, E. Kjeang, N. Sabaté, Adv. Energy Mater. 7 (2017) 1700275.

[25] O. A. Ibrahim, P. Alday, N. Sabaté, J. P. Esquivel, E. Kjeang, J. Electrochem. Soc. 164 (2017) A2448-A2456.

6 Paper-based microfluidic aluminum-air batteries: toward next-generation miniaturized power supply

Liu-Liu Shen [a], Gui-Rong Zhang [a,*], Markus Biesalski [b], and Bastian J.M. Etzold [a,*]

[a] Ernst-Berl-Institut für Technische und Makromolekulare Chemie, Department of Chemistry, Technische Universität Darmstadt, Alarich-Weiss-Straße 8, 64287 Darmstadt, Germany

[b] Laboratory of Macromolecular Chemistry and Paper Chemistry, Department of Chemistry, Technische Universität Darmstadt, Alarich-Weiss-Straße 8, 64287 Darmstadt, Germany

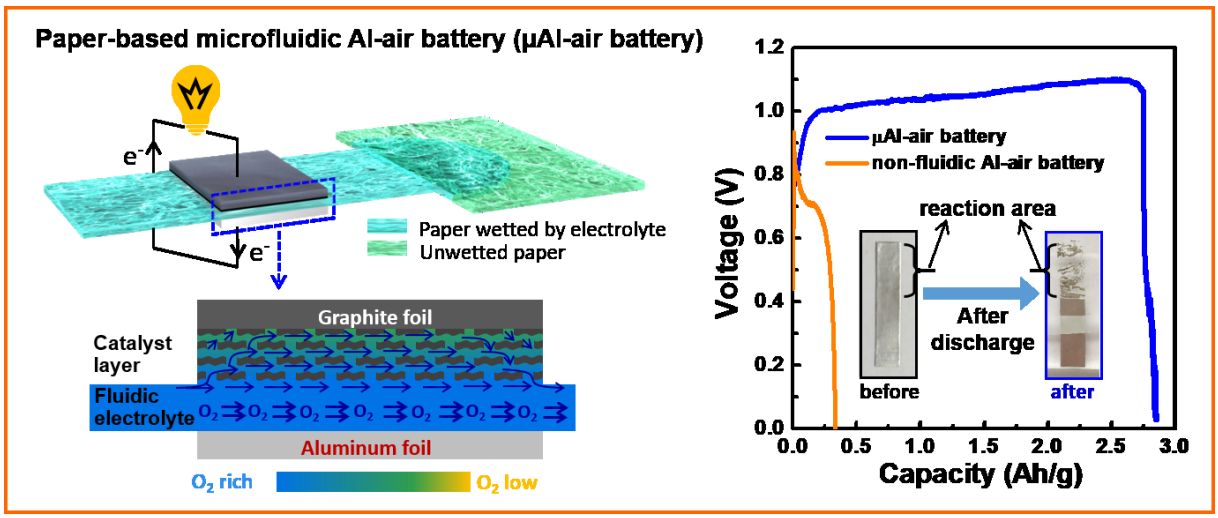

Redrafted from ***Lab on a Chip 19 (2019) 3438-3447.***

Abstract

Paper-based microfluidics (lab on paper) emerges as an innovative platform for building small-scale devices for sensing, diagnosis, and energy storage/conversions due to the power-free fluidic transport capability of paper via capillary action. Herein, we report for the first time that paper-based microfluidic concept can be employed to fabricate high-performing aluminum-air batteries, which entails the use of a thin sheet of fibrous capillary paper sandwiched between an aluminum foil anode and a catalyst coated graphite foil cathode without using any costly air electrode or external pump device for fluid transport. The unique microfluidic configuration can help overcome the major drawbacks of conventional aluminum-air batteries including battery self-discharge, product-induced electrode passivation, and expensive and complex air electrodes which have long been considered as grand obstacles to aluminum-air batteries penetrating the market. The paper-based microfluidic aluminum-air batteries are not only miniaturized in size, easy to fabricate and cost-effective, but they are also capable of high electrochemical performance. With a specific capacity of 2750 Ah/kg (@20 mA/cm^2) and an energy density of 2900 Wh/kg, they are 8.3 and 12.6 times higher than those of the non-fluidic counterpart and significantly outperform many other miniaturized energy sources, respectively. The superior performance of microfluidic aluminum-air batteries originates from the remarkable efficiency of paper capillarity in transporting electrolyte along with O_2 to electrodes.

6.1 Introduction

The rapid advance of information technology and future demands for internet of things (IoT) devices have stimulated explosive growth in the market for small, portable and disposable electronics, which are envisioned to provide versatile functions such as sensing, diagnostics, display, or medical therapy in our daily life [1-3]. This raises concerns about how to mitigate the power needs of the dramatically rising number of small-sized devices. Lithium-ion batteries (LIBs) have been the dominant technology. However, the low abundance of lithium and significant environmental impacts during lithium mining and battery manufacturing have raised serious doubt about their feasibility for large-scale sustainable applications. It is also anticipated that a huge number of batteries, most of which are still almost fully charged after a single use, might be disposed in an uncontrolled manner. This will lead to energy waste and serious environmental impact [3, 4]. Alternative energy sources are urgently required to meet

the power requirement of small electronic devices at minimal environmental cost. Aluminum-air (Al-air) batteries have great potential because of their numerous practical advantages, such as remarkably high theoretical specific energy density (8.1 kWh/kg), high theoretical voltage (2.7 V), abundance of raw materials (aluminum is the most abundant metal element in the earth's crust at 8.1 wt%), low-cost, environmentally friendly nature of aluminum, and safety for use in residential and commercial environments [5-10].

Despite the great potential of Al-air batteries to be employed as next-generation power supplies, several scientific and technical issues need to be tackled before their commercial-scale implementation: 1) Self-discharge: the parasitic corrosion reaction of aluminum and electrolyte causes self-discharge and shortens the battery shelf life; 2) Passivation of anode by discharge products: formation of gel-like aluminum hydroxide and/or hydrated alumina passivates the anode surface and prevents further discharging; 3) Expensive and complex air electrode: careful design of the air electrode, with an active catalyst, gas diffusion layer and current collector, is essential to promote oxygen diffusion/reduction [5-7, 11, 12] and prevent pore clogging by carbonate formation and deposition at air electrodes [13]. Due to its structural complexity, the air electrode usually represents the most expensive part in an Al-air battery.

A lot of research has been done on these problems. For example, intensive works are dedicated to modifying aluminum with other metals to form an alloy; using a non-aqueous electrolyte to alleviate the anode corrosion and passivation [14-22]; developing novel electrolytes, catalysts and air electrodes with sophisticated pore structures to enhance oxygen reduction reaction (ORR) activity and increase the oxygen mass transfer rate [23-37]. However, these advancements can lead to increased system costs, and complicated and costly procedures for battery component recycling. Al-air batteries with flowing electrolytes are an alternative way to mitigating the oxygen mass transfer challenge, but external pressure sources (e.g., pumps) are needed to maintain electrolyte flow. This would also add to system costs, making miniaturization of the flow battery system for small devices unrealistic.

In the current work, a paper microfluidic concept has been implemented for the first time in constructing Al-air batteries, and the fabricated paper-based microfluidic Al-air battery (denoted as μAl-air) can be employed as a miniaturized power supply for those small-sized disposable electronics. Moreover, those scientific and technical problems faced by

conventional Al-air batteries can be largely relieved or even eliminated on these miniaturized energy devices. As a matter of fact, paper materials have already been employed as a key component in making as low-cost, eco-friendly portable and flexible power sources, which take function as electrode separator, electrolyte/redox species reservoir, or electrodes (e.g., electric conductive paper) [38-44]. Different from these reports, here in the current work, paper is employed as microfluidic channel to continuously and spontaneously transport electrolyte solution with steady flow rate, largely benefiting from the capillary action on paper with cellulosic fibrous structure. The μAl-air batteries are composed of an aluminum foil anode, a catalyst loaded graphite foil cathode, and a sheet of porous paper, which serves as both separator and microfluidic channel for carrying electrolytes to electrode surfaces (**Figure 6.1a**). This unique paper-based microfluidic design is expected to bring about the following advantages to an Al-air battery: First, Al anode is stored separately from the electrolyte before use, which can completely prevent parasitic corrosion induced self-discharge and prolong battery shelf life. Second, continuous flow of the electrolyte can minimize the accumulation of non-reactive discharge products (e.g., $Al(OH)_3$) at anode/cathode surfaces, preventing electrodes from surface passivation. Third, the capillary driven flow within the porous paper channels enables sufficient mass transfer of O_2 to cathode and completely omits the use of expensive air electrodes and bypasses the pore clogging issue of air electrodes, which represents one of the major causes of battery failure. Compared with traditional (micro) flow batteries, no external equipment, e.g., pumps, is needed in the paper-based μAl-air battery to circulate the electrolyte. The latter is unique to paper-based capillary transport systems [45-48]. The resultant structure, together with cost-effective and eco-friendly battery components, makes μAl-air batteries feasible as the next-generation of power supply for portable and disposable electronic applications, particularly in single-use devices in diagnosing and sensing fields.

6.2 Experimental section

Material and chemicals. Palladium 10% on carbon (type 487, Alfa Aesar), potassium hydroxide (Alfa Aesar), ethanol (VWR), Nafion solution (5 wt%, Sigma-Aldrich), conductive silver printing ink (resistivity 5-6 μΩ cm, Sigma-Aldrich) were all analytical-grade reagents and used as received without any further purification. Aluminum foil (thickness: 0.05 mm) was purchased from Sigma-Aldrich. Graphite foil (thickness: 0.35 mm) was purchased from

Sigraflex. Filter paper (grade 417, thickness: 0.15 mm, mean pore diameter: 50 μm, mean porosity: 50%) was purchased from VWR. All solutions were prepared with ultra-pure water. Gas diffusion layer (GDL, 28BC) was purchased from Ionpower. An electric fan (A105) with a power rating of 10 mW was purchased from H-TEC Education GmbH.

Preparation of the battery prototype. Cathode electrode is Pd/C on graphite foil, with Pd/C as catalyst and graphite foil as current collector. Graphite foil was first cut into rectangular shape pieces with 25 mm in length, and then cleaned with ethanol and ultrapure water under ultrasonication. PMMA substrate (60×40 mm) was cleaned under the same protocols. A catalyst ink (20 mg/mL) was prepared by sonicating Pd/C in water. Typically, 8 μL of catalyst ink (Pd loading: 0.04 mg/cm^2) was carefully applied onto one end of the graphite foil by drop casting, covering a surface area of 40 mm^2 (**Figure S6.1a**). Catalyst coated electrodes were then left air dried at room temperature for 30 min prior to use. In order to prevent catalyst detaching from the graphite foil, a certain amount of Nation solution was dropped onto the catalyst layer and the dried at room temperature for another 30 min. The mass ratio of Pd to Nation is fixed at 100:1. Aluminum foil was cut into rectangular shape pieces with 25 mm in length and used as anode directly, as shown in **Figure S6.1a**. The electrodes are fixed on the PMMA substrate by tape for easy operation, as detailed in **Figure S6.1b**. The anode and cathode electrodes were places face-to-face and separated by a piece of filter paper (VWR grade 417, 80×10 mm^2). Note, we used this particular paper, as it consists of cotton linters fibers which are composed of almost pure alpha cellulose with very little lignin and further polysaccharides, respectively. The width of the geometric electrode active area (the overlapping area of the electrode and electrolyte) was 8 mm. A rectangular shaped absorbent pad (40×30 mm^2) was placed at the end of the paper strip, and the other end of the paper strip was immersed in electrolyte during battery discharge (**Figure S6.1c**).

Flow rate measurements. Flow rate of electrolyte (1.5 M KOH) within paper channel (VWR grade 417, 10 mm in width) was measured by monitoring the mass gain of the absorbent pads (VWR grade 417, 40×30 mm^2) over time using an analytical balance. A digital webcam (Logitech C920 PRO HD) was used to record the readings of the balance. As shown in **Figure S6.2a**, one end of the paper channel was immersed in the reservoir out of the balance, and the absorbent pad was placed on the other end of the paper channel on the balance. The reservoir was filled with 1.5 M KOH solution (1.056 g/mL at 20 ℃). The solution density

was obtained by weighting 1.000 mL solution. The balance was tared immediately the liquid front reached the absorbent pad. A steady weight increase can be observed until the absorbent pad was fully saturated by the electrolyte. The volume (mL) of the electrolyte in absorbent pad was converted from the mass (g) of the electrolyte, and then plotted against time (min), and linear regression was used to determine the volumetric flow rate (**Figure S6.2b**).

Fabrication of the pouch battery. The paper-based μAl-air pouch battery is shown in **Figure S6.3a** and **Figure 6.6**. The anode and cathode electrode, together with the filter paper strip and absorbent pad, were attached to a piece of laminating pouch, and their relative positions were the same as the prototypical battery on a PMMA substrate mentioned previously. The punch battery was sealed by using an office laminator (Fellowes Lunar A4). Each battery underwent the laminating press twice, once from each direction: 1) along the paper channel (from absorbent pad to the electrodes), 2) across the paper channel (from cathode electrode to anode electrode). A sponge (around 1 cm^3 in volume) saturated with electrolyte was placed at the end of the paper channel to serve as an electrolyte reservoir. When two batteries were connected in series (**Figure S6.3b**), they were placed at a proper angle; the end of the paper channel overlaps with each other, so that one piece of sponge is able to trigger two cells at the same time. Conductive silver printing ink was used to connected batteries to reduce the ohmic resistance.

Electrochemical measurements. Electrochemical measurements were carried out on a PMC-1000 multichannel potentiostat (AMETEK) controlled by Versastudio software at room temperature. The electrochemical measurements were carried out shortly after the electrolyte flowed along the paper channel through the electrodes and reached the absorbent pads. The cell resistance between anode and cathode electrodes was determined by conducting the AC impedance analysis (100 kHz, 5 mV), with a cell resistance of under 10 Ω implying a good connection. The open circuit voltage (OCV) and power of the battery were measured by LSV from OCV to 10 mV with a step height of 20 mV at 2 s intervals. Galvanostatic discharge of batteries was performed using chronopotentiometry technique. For comparison, the projected geometric electrode area (overlapping area between the Al foil and catalyst coated cathode at the reaction zone) was used to calculate current density and power density during normalization. For each condition, the measurements were conducted at least four times, using different batteries to generate the error bars (defined as the relative standard deviation).

Structural analysis. The thickness of the aluminum foil, graphite foil and paper materials were measured using a high precision dial thickness gauge with 0.001 mm reading (F-1101/30, Käfer Messuhren GmbH). The morphology and elemental mapping of battery cross-section and electrodes were probed using a Scanning Electron Microscopy (Philips XL30 FEG) equipped with an EDAX X-ray detector (CDU Leap XL-30) operated at an accelerating voltage of 30 kV.

6.3 Results and discussion

6.3.1 Structure and design of paper-based µAl-air batteries.

A three-layer sandwich structure consisting of cathode, separator and anode is employed to construct the reaction zone of µAl-air batteries, as shown in **Figure 6.1a** and **Figure S6.1**, respectively. The microfluidic paper channel (separator) is sandwiched between Al foil (anode) and Pd/C coated graphite foil (cathode), and the reaction zone lies in between the electrolyte reservoir and absorbent pad. Instead of using a gas diffusion air electrode, poreless graphite foil is used at the cathode as it acts as both current collector and substrate for coating Pd/C to catalyze the ORR process. The microscopic structure of the paper-based µAl-air battery was investigated using cross-sectional scanning electron microscopy (SEM) and energy dispersive X-ray (EDX) elemental mapping analyses (**Figure 6.1b-e**), with which the layered structure can be easily distinguished. The signals from carbon and aluminum roughly follow the shape of the graphite foil and aluminum foil, respectively, while the catalyst layer features a strong signal from Pd. The thicknesses of each layer can also be determined: 50 µm - Al anode, 165 µm - paper channel, 230 µm - catalyst layer (Pd loading 0.04 mg/cm^2), and 350 µm - graphite foil.

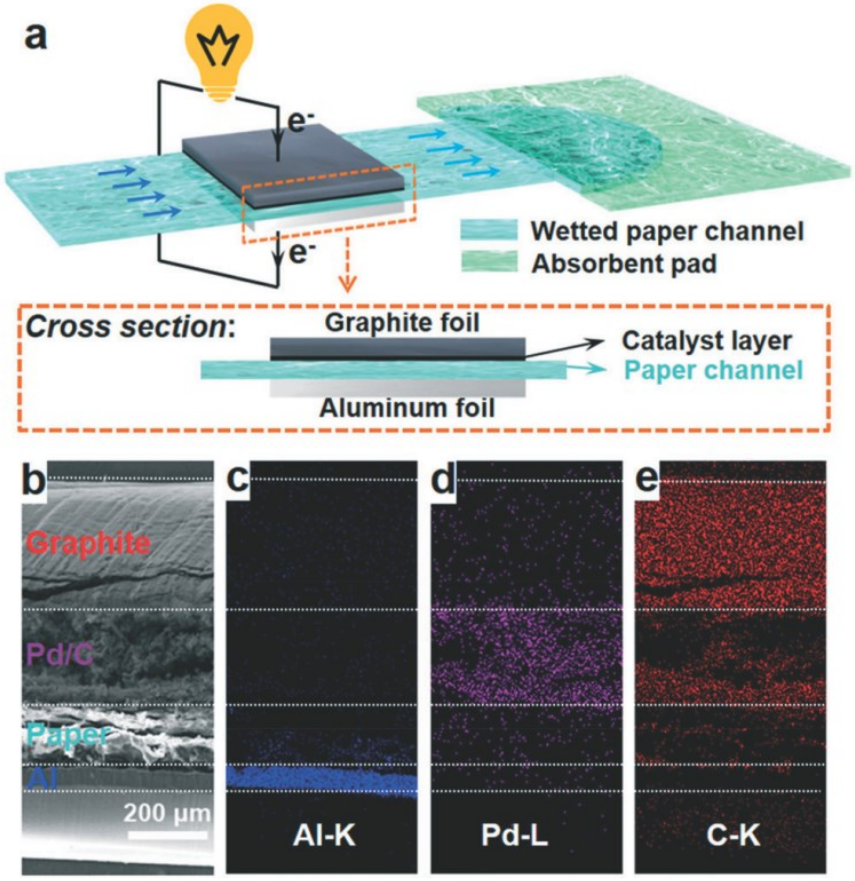

Figure 6.1 (a) Schematic illustration of a paper-based μAl-air battery; (b) Cross sectional SEM image; and (c-e) EDS elemental mapping images of a paper-based μAl-air battery.

Successful implementation of the paper microfluidic Al-air battery concept relies heavily on the feasibility of sustainable capillary flow within the paper channel. In a paper-based μAl-air battery, the electrolyte flows along the paper channel in a laminar way, driven by the capillary force; no external auxiliaries (e.g., pumps) are used to maintain the laminar flow. From a macroscopic point of view, the single-phase flow of a Newtonian liquid within a porous medium (e.g., paper) is governed by Darcy's law:

$$v = \frac{k}{\eta}\frac{\Delta P}{\Delta x} \tag{6.1}$$

where v is the flow velocity (m/s), k is the permeability (m^2), η is the viscosity (Pa·s), $\Delta P/\Delta x$ represents the pressure change per unit length (Pa/m). In the case of imbibition-driven flow in paper, the pressure is the capillarity suction given by the Young-Laplace equation:

$$\Delta P = \frac{2\sigma cos\theta}{r} \tag{6.2}$$

where σ is the liquid-air surface tension (N/m), θ is the liquid-fiber contact angle, r is the average pore radius of the paper (m). With the increase of distance moved by the fluid on paper, the $\Delta P/\Delta x$ reduces as a function of time. Substituting the **Equation 6.2** into **Equation 6.1** gives:

$$x(t) = 2\sqrt{\frac{k\sigma t cos\theta}{\eta r}} = \sqrt{Dt} \quad (\mathbf{6.3})$$

where x is the distance moved by the fluid front (m) under capillary pressure, t is the time (s), D is a simplified diffusion coefficient [49]. This is the well-known Lucas-Washburn equation, which points out that flow velocity of liquid in a rectangular paper strip diminishes with time increasing [50]. Nonetheless, as demonstrated in other paper-based microfluidic devices, using an absorbent pad at the end of the paper channel will make the liquid imbibition dynamics deviate from classic Lucas-Washburn behavior, and a quasi-stationary flow over time can actually be sustained [51, 52]. In the current work, the flow rate of electrolyte within the paper channel was experimentally determined by following a previously developed protocol [53]. As shown in **Figure S6.2**, the volume of an aqueous KOH solution keeps increasing linearly over time; regression analysis shows that the flow rate of the electrolyte is around 24 μL/min. This result verifies that the microfluidic design can enable quasi-stationary flow within a paper channel, which provides the foundation for steady discharge in μAl-air batteries.

6.3.2 Electrochemical performance of paper-based μAl-air batteries

The possible influences of two critical chemical components, the Pd/C catalyst and the KOH electrolyte, were studied and optimized before analyzing the electrochemical performance of the paper-based μAl-air battery (**Figure 6.2**). Pd/C was employed as the cathode catalyst because of its fairly high catalytic activity toward ORR [54, 55]. The Pd loading on the cathode was varied from 0.025 to 0.075 mg/cm^2 to investigate its influence on battery performance. As shown in **Figure 6.2a**, the peak power density increases linearly with the Pd loading, from 0.025 to 0.04 mg/cm^2, and then reaches a plateau with increasing Pd loading up to 0.075 mg/cm^2, which is probably due to low catalyst utilization associated with the thick catalyst layer. Therefore, a Pd loading of 0.04 mg/cm^2 was chosen in the following investigations. Experiments were also performed to investigate the influence of electrolyte

concentration (**Figure 6.2b**). The KOH concentration was varied in the range of 0.2 to 2.5 M. The peak power density increases by almost 3 times when the KOH concentration increases from 0.2 to 1.5 M, while a deviation from this trend is observed by further increasing the KOH concentration up to 2.0 and 2.5 M. This unique dependence behavior is a consequence of the interplay between facilitated Al oxidation reaction at the anode, and disfavored ORR at the cathode, with more concentrated KOH electrolyte [56-58]. The battery performance becomes unstable and power density starts declining when the KOH concentration reaches 2.0 M (**Figure S6.4**), which may originate from degradation of the cathode catalyst and/or cellulose paper in the presence of a strong alkaline medium [59]. In view of these results, a KOH concentration of 1.5 M is adopted as a tradeoff between high peak power density and good battery operation stability.

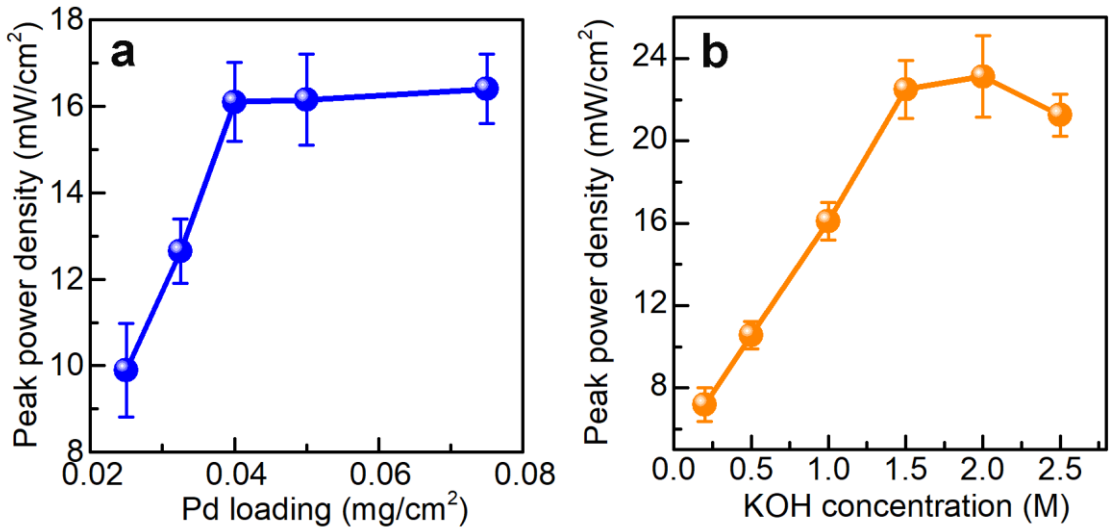

Figure 6.2 (a) Influence of the Pd loading on peak power density. KOH concentration: 1.0 M; the geometric electrode active area: 8×5 mm^2. (b) Influence of the KOH concentration on the peak power density. Pd loading: 0.04 mg/cm^2; the geometric electrode active area: 8×5 mm^2.

The electrochemical performance of the paper-based μAl-air batteries was then characterized by recording their polarization (V-I) and power density curves (**Figure 6.3**). At the same time, a non-fluidic counterpart Al-air battery with a similar layout but using electrolyte-wetted paper between anode and cathode (**Figure S6.5**) was also constructed and tested as a reference. The linear sweep voltammetry (LSV) from open circuit voltage (OCV) to 10 mV was recorded 10 times. **Figure 6.3a** shows the polarization (V-I) and power density curves recorded on a paper-based μAl-air battery under continuous LSV. Both the maximum current

density and peak power density of the μAl-air battery first increase and then level off after the 3rd voltammetric scan. The OCV of the battery approaches ca. 1.55 V, and the maximum current density reaches 66.5 mA/cm^2 (absolute current: 26.6 mA). The battery can also deliver a peak power density of 22.5 mW/cm^2 (absolute power: 9.0 mW), which is significantly superior to many other miniaturized power supplies (compared in **Figure 6.3d** and **Table S6.1**). In contrast to the μAl-air battery, the performance of the non-fluidic counterpart drops quickly with the scan number (**Figure 6.3b**). Its peak power density decreases by 40% and 75% after the 3rd and the 10th voltammetric scans, respectively, indicating that the non-fluidic Al-air battery suffers severe degradation during the polarization tests.

Continuous battery operation is studied by recording the Galvanostatic discharge curves at various current densities, ranging from 5 to 20 mA/cm^2 (**Figure 6.3c** and **Figure S6.6**). The μAl-air battery can exhibit a relatively steady discharge voltage, and all of the Al anodes were almost fully consumed regardless of the discharge current, as shown in the inset of **Figure 6.3c** and **Figure S6.6a**. At a discharge current density of 20 mA/cm^2, the specific capacity (based on the total mass of Al in the anode) is estimated to be 2750 mAh/g (corresponding to a coulombic efficiency of 92%), implying that the parasitic self-corrosion of Al is largely suppressed in the μAl-air battery. Most recently, Leung et al. reported the fabrications of paper-based Al-air battery in which a piece of paper was sandwiched between an air electrode (consisting of ORR catalyst, Ag mesh current collector and a gas diffusion layer) and an Al anode, and they also found that porous and tortuous microstructure of paper can greatly impede the diffusive transport of OH^-, consequently suppressing Al corrosion despite a non-fluidic configuration is employed during the battery discharge [60, 61].

The specific energy density (based on the total mass of Al foil) is calculated to be 2900 Wh/kg, which represents one of the highest values among miniaturized/flexible Al-air batteries. A relatively lower discharge current density is always accompanied by a lower specific capacity, which may stem from the parasitic self-corrosion of Al ($Al + 3H_2O + OH^- \rightarrow 3/2H_2 + Al(OH)_4^-$) [5, 62]. As shown in **Figure S6.7**, it takes 57 min for a piece of Al foil (8×5 mm^2) to be fully dissolved in 1.5 M KOH solution. Lower discharge current along with longer discharge time could have led to severer parasitic Al corrosion, which results in lower overall specific capacity of the battery [5, 62]. A different picture emerges for the non-fluidic Al-air battery: voltage drops quickly regardless of the discharge current densities (**Figure**

S6.6b); this result is in line with the rapid degradation of the non-fluidic Al-air battery during polarization tests (**Figure 6.3b**). The Al anodes stay intact after discharging, although the surface of the Al foil becomes coarse, and some white deposit covers the Al foil surface (**Figure 6.3c** and **Figure S6.6b**). When the battery is discharging at 20 mA/cm^2, the specific capacity and energy density of the non-fluidic battery are calculated as 330 mAh/g and 230 Wh/kg, respectively, which is 8.3 and 12.6 times lower than the values obtained using the μAl-air battery. Attempt were also made to construct a non-fluidic Al-air battery using a gas diffusion layer air electrode at the cathode, which is widely adapted in conventional Al-air batteries. The performance is shown in **Figure S6.8**: the peak power density declines significantly with the voltammetric scan numbers, which is similar to the non-fluidic Al-air battery without air electrode. Both the peak power density (20.5 mW/cm^2, read at the 1st V-I scan) and specific capacity (500 mAh/g) are superior to those of the non-fluidic counterpart without air electrode, which is not surprising since the mass transfer of O_2 is facilitated using the air electrode, while at the same time the performance is still much worse than that of the μAl-air battery, demonstrating the great advantage of the microfluidic configuration in building high-performing Al-air batteries.

The performance of the paper-based μAl-air battery was also tested using neutral electrolyte (2 M NaCl; **Figure S6.9**). The μAl-air battery can exhibit an OCV of 0.70 V, and a maximum power density of 11.3 mW/cm^2. It can also be observed that the battery can discharge steadily at 20 mA/cm^2 until most of the anode aluminum foil is consumed, and the battery exhibits a specific capacity of 2200 mAh/g, which corresponds to 80% that of the battery using KOH electrolyte. These results indicate that the possible anode passivation by insoluble reaction product (e.g., $Al(OH)_3$) is less likely taking place on these paper-based μAl-air batteries regardless of the nature of electrolyte. It is hypothesized that insoluble products might be flushed away by the flow of electrolyte, which helps minimize the accumulation of those insoluble products and prevent electrode surface from passivation. Moreover, as shown in **Figure 6.3d** and **Table S6.1**, paper-based μAl-air batteries, whether using an alkaline or neutral electrolyte, exhibit superior power and energy densities to recently reported miniaturized metal-air batteries, and are even comparable to some of the primary Al-air batteries. The success in using NaCl electrolyte also raises the possibility of activating μAl-air batteries by directly using naturally abundant seawater, which sheds new light on developing fully sustainable energy storage/conversion devices in the future.

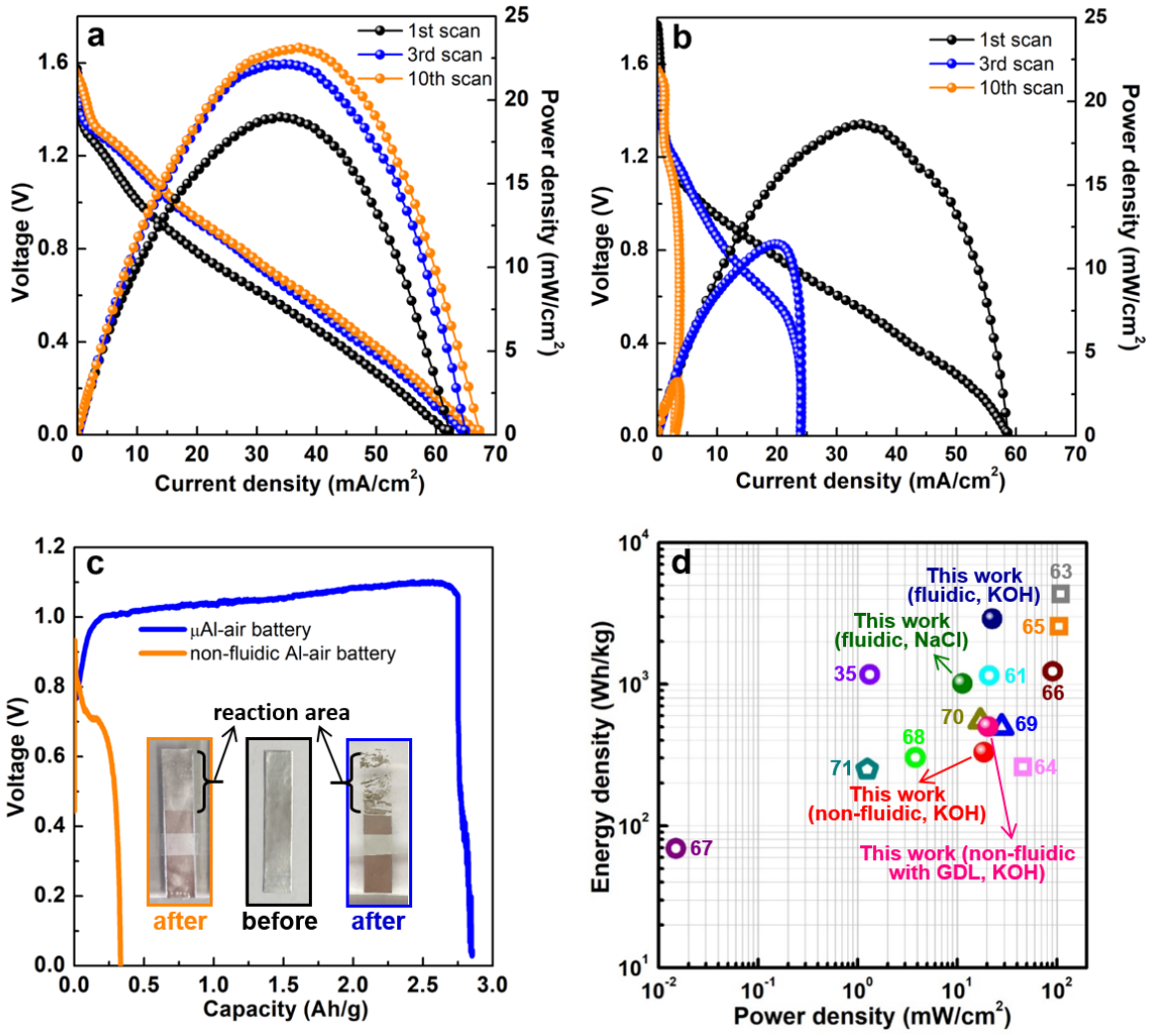

Figure 6.3 Polarization (V-I) and power density curves recorded at different scan numbers measured by continuous LSV: (a) paper-based μAl-air battery; and (b) paper-based Al-air battery with stagnant (non-fluidic) configuration; (c) Discharge curves at current density of 20 mA/cm^2. The insets in (c) are the optical images of the anode aluminum foil before (middle) and after discharge (left: non-fluidic Al-air battery; right: μAl-air battery); (d) Comparison of power density vs. energy density of μAl-air batteries with other energy storage devices. Square: primary Al-air battery; circle: miniaturized Al-air battery; triangle: miniaturized Zn-air battery; pentagon: miniaturized eutectic gallium-indium-air battery [35, 61, 63-71].

Rechargeability of the μAl-air battery was also investigated. Although Al-air batteries with aqueous electrolyte are in principle not electrically rechargeable, the mature Al refining/recycling technology and market make it feasible to "mechanically" recharge Al-air batteries by simply replacing entire Al anodes. The μAl-air battery can exhibit excellent cycle

performance during a mechanical recharging process (**Figure S6.10**), which is done by replacing the Al foil after a preceding full discharge operation at 20 mA/cm^2.The discharging curves are in a comparable range after 3 cycles, implying that the cathode electrode is robust and can be used repeatedly in the μAl-air battery, which would be desirable for practical applications.

6.3.3 Insight into the advantage of paper-based μAl-air batteries

Despite their simple structure, paper-based μAl-air batteries exhibit superior performance in both power density and energy density, largely due to the unique microfluidic configuration. The most intriguing question is about the advantage of microfluidic design. Before this question can be answered, the rapid battery drain of non-fluidic Al-air batteries must be assessed.

As shown in **Figure 6.3c**, the non-fluidic Al-air battery can barely sustain steady voltage during discharge and rapidly shuts down due to severe degradation. To probe the degradation mechanism of non-fluidic Al-air batteries, attempts were made to recover the degraded non-fluidic Al-air battery, using either a new anode or cathode, along with newly prepared electrolyte. The discharge capacity of the non-fluidic Al-air battery can only be recovered when a new cathode is used (**Figure S6.11**), indicating that the cathode is mainly responsible for the degradation of non-fluidic Al-air batteries. In a conventional proton exchange membrane (PEM) fuel cell, complete flooding of the cathode by an aqueous electrolyte would result in a significant loss of cell performance due to the limited diffusion coefficient of O_2 in aqueous phase and associated restricted mass transfer of O_2 to ORR catalysts [72-75]. To find out whether degradation of the non-fluidic Al-air battery is caused by analogous cathode flooding, the cathode was dried out for 2 h, then re-used in the non-fluidic Al-air battery for the next discharge. Battery performance, in terms of discharge voltage and capacity, can be fully regained using the recovered cathode (**Figure S6.11c**). This confirms that the fully flooded cathode is the main cause of battery degradation.

Based on this, there is a possible rationale for the dramatic difference in performance between the μAl-air battery and its non-fluidic counterpart. In this work, oxygen molecules for ORR mainly come from naturally dissolved O_2 from air. In a non-fluidic battery, the channels and pores in the catalyst layer are fully flooded by the electrolyte. The continuous consumption of

oxygen at the cathode and slow diffusion of O_2 from bulk electrolyte to catalyst pores results in a build-up of the depletion layer for the dissolved O_2 near the catalyst surface; the gradually decreasing O_2 concentration leads to a decline in power density (**Figure 6.3b**) and eventually battery shut down (**Figure 6.3c**) when the O_2 within the catalyst layer is depleted. In contrast, the power density of a μAl-air battery slightly increases from the 1st to the 3rd LSV, which is probably related to the electrolyte penetrating into the catalyst layer. After this, fairly stable power output can be obtained (**Figure 6.3a**). As shown in the Galvanostatic discharge measurements (**Figure 6.3c** and **Figure S6.10**), the μAl-air battery can discharge steadily until the Al anode is completely consumed. After mechanical recharge by replacing the Al foil, the μAl-air battery has almost unchanged capacity, indicating that no limitation from O_2 transportation has come into effect during the discharge process.

To gain further insight into the superiority of the microfluidic configuration in facilitating the mass transfer of O_2 to the cathode, an additional experiment was performed by placing a piece of porous paper onto the microfluidic paper channel (**Figure 6.4a**). The additional porous paper was used to mimic the catalyst layer in direct contact with the microfluidic paper channel. Then one end of the paper channel was alternately dipped into a dye solution and a clear water solution. The time lapse images of solution flow patterns within the overlay paper were recorded (**Figure 6.4a**). The flow pattern within the overlay paper always follows that of the paper channel underneath when switching the inlet solution from dye to water or vice versa. It seems that a portion of the solution diverts into the overlay paper. The diverted solution flows through the overlay paper and then converge into the main stream in the underneath paper channel. These results imply that the liquid phase within the pores of the overlay paper is not stagnant, and the pores keep being replenished by the new solution via convection. By applying this knowledge to the μAl-air battery, O_2-rich fresh electrolyte can be "convectively" transported to the cathode catalyst layer in a continuous manner, which could prevent the build-up of the O_2 depletion layer within the cathode (**Figure 6.4b**). This is not the case in a non-fluidic Al-air battery as mass transfer of O_2 can only be achieved by slow diffusion in an aqueous solution, which would lead to rapid degradation of non-fluidic Al-air battery due to fast depletion of O_2 at near surfaces of the cathode (**Figure 6.4c**). Even though using an air electrode in a non-fluidic Al-air battery can postpone battery shutdown by directly feeding air to the cathode, its overall capacity is still limited by the cathode, as reflected by the declining discharge curve accompanied by a well-reserved Al anode after

discharge (**Figure S6.8b**). The much lower overall capacity compared to the µAl-air battery again demonstrates the great structural advantage of the microfluidic configuration in facilitating mass transfer of O_2.

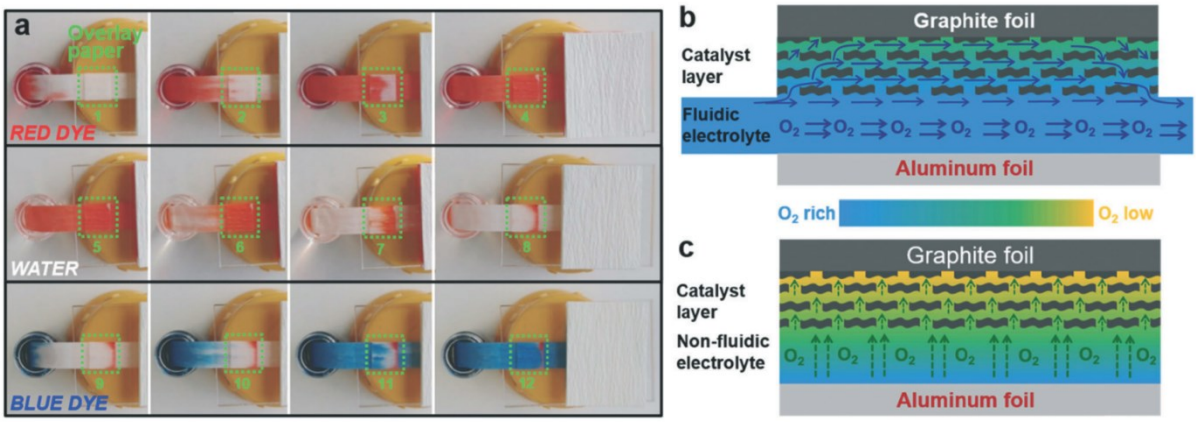

Figure 6.4 (a) Time-lapse photos showing flow patterns of solutions within the overlay paper, where the green squares mark the overlay paper. Schematic illustrations of O_2-rich/low electrolyte distribution in (b) µAl-air battery, and (c) non-fluidic Al-air battery in cross-section.

6.3.4 Practical applications

To meet the power requirements of various electronic devices, the power scalability of paper-based µAl-air batteries was first investigated by either enlarging the electrodes (geometric electrode active area) or connecting several batteries in series. The peak power of the µAl-air batteries can be increased by 37.5% and 85.2% when the electrode width is enlarged from 5 to 10 and 15 mm, respectively (**Figure 6.5a** and **Figure S6.12**). The areal power density (power normalized to the geometric electrode active area) is reduced on larger electrodes (**Figure 6.5a**), which probably originates from the severer depletion of O_2 at the electrode along the direction of flow, as has been recently reported [53]. Nevertheless, both OCV (3.0 V) and power density (17.9 mW) are nearly doubled when two batteries are connected in series (**Figure 6.5b**), indicating good voltage and power scalability of µAl-air batteries in series configuration.

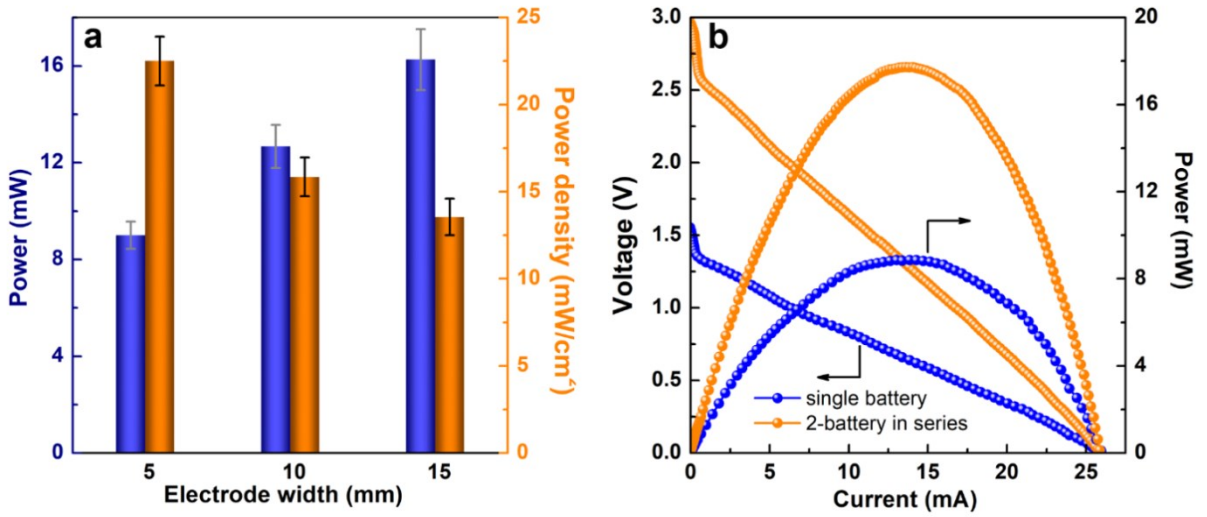

Figure 6.5 (a) Comparison of power/power density in paper-based μAl-air batteries with three electrode sizes (geometric electrode active area: 8×5, 8×10, 8×15 mm^2). (b) Polarization (V-I) and power density curves of a single battery and two paper-based μAl-air batteries connected in a series.

The initial lab scale testing setup (**Figure S6.1**) of the paper-based μAl-air batteries was expanded to a pouch cell configuration (**Figure 6.6a-b** and **Figure S6.3**) which is more user-friendly. The pouch batteries can be activated by simply contacting the paper with an electrolyte storage device (in this case a piece of sponge pre-wetted with 1.5 M KOH electrolyte), as shown in **Figure S6.3**. Polarization curves were then recorded by performing LSV measurements on the pouch batteries. The voltage-current characteristic is identical to the prototypical μAl-air battery (**Figure S6.3c**). Therefore, the pouching process has little impact on the performance of the paper-based μAl-air battery. The pouch batteries were then used to power some small electronic devices. A single battery (geometric electrode active area: 8×5 mm^2) was able to fully power a hand-held calculator with a LCD display (**Figure 6.6c**). A single battery (geometric electrode active area: 8×15 mm^2) is capable to keep a mini-fan running for over 70 min, as shown in **Figure 6.6d** and **Figure S6.13**. Attempts were also made to use two connected batteries to power a LED lamp (**Figure 6.6e**); more LED lamps can be on at the same time due to the high overall power output (**Figure 6.6f**). These results successfully demonstrate the great potential of μAl-air batteries to meet the power demand of small portable and disposable electronic devices. Further optimization of the battery geometry and miniaturization of the battery is now required, which could be achieved by integrating solid KOH or NaCl into the inlet of the paper channel. The μAl-air battery can then be

conveniently activated by adding water, which will bring the µAl-air battery closer to being an ideal power supply option for small devices. Moreover, cellulose fibers with high mechanical properties and well-defined porous structures, such as TEMPO-oxidized cellulose nanofibers, hold great potential to further boost the performance of paper-based microfluidic batteries [59, 76, 77].

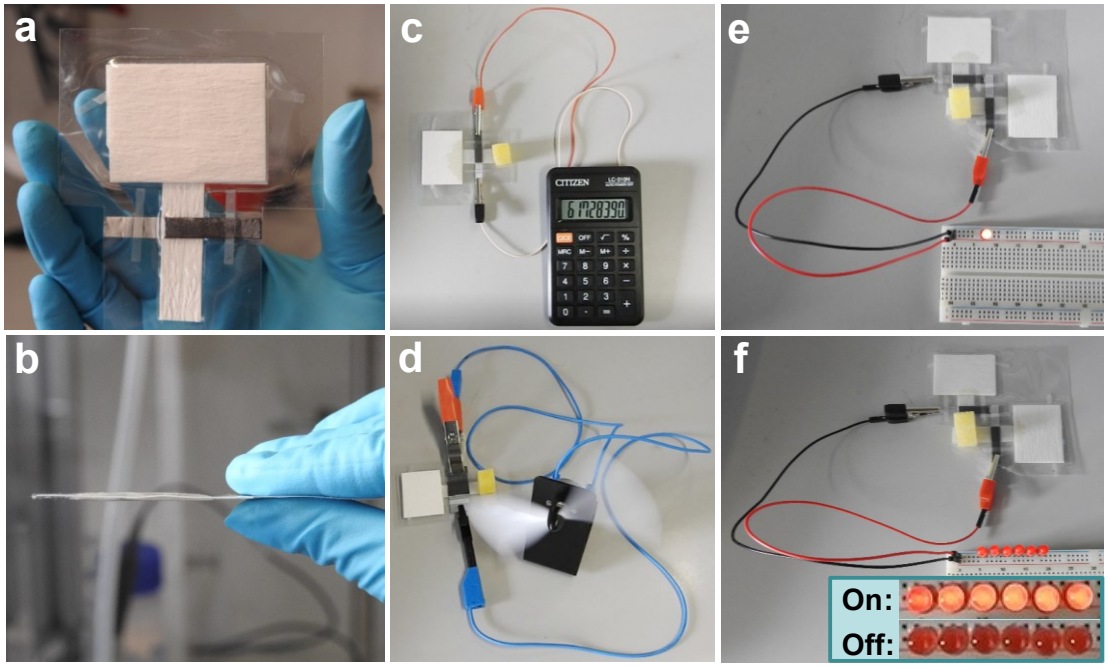

Figure 6.6 A paper-based µAl-air pouch battery from (a) top and (b) side view. (c) A single battery (geometric electrode active area: 8×5 mm^2) powering a calculator. (d) A single battery (geometric electrode active area: 8×15 mm^2) powering a mini-fan. Two series-connected µAl-air pouch batteries (geometric electrode active area: 8×5 mm^2), powering (e) one and (f) six LED lamp(s).

6.4 Conclusion

In addition to developing novel electrocatalysts and structural engineering of complex air electrodes, adoption of a microfluidic configuration turns out to be a highly efficient and inexpensive way to construct high-performing Al-air batteries. In comparison to conventional Al-air batteries, where the electrolyte is pre-loaded, in a µAl-air battery a porous paper channel enables spontaneous capillary flow of electrolyte, which can efficiently shuttle O_2 to the cathode, overcoming many shortcomings of conventional Al-air batteries, e.g., self-discharge, short shelf life, and spontaneous electrode passivation by reaction products. The

microfluidic paper-based design eliminates expensive air electrode from the Al-air battery, which helps minimize overall system cost and battery encapsulation effort since the bothersome open cell structure of air electrodes can be omitted, and at the same time bypasses the pore clogging issues. The μAl-air battery exhibits impressive electrochemical performance in specific capacity (2750 Ah/kg) and energy density (2900 Wh/kg), both of which are significantly superior to Al-air batteries with non-fluidic configuration, irrespective of whether an air electrode was used. The excellent performance of μAl-air batteries is also reflected by their capacity to power electronic devices with different power requirements. We believe that the paper-based microfluidic concept demonstrated here has the potential to significantly advance the design of metal-air battery systems, creating next-generation high-efficiency, low-cost and eco-friendly energy sources, and can potentially have strong implications for the construction of other high-performing energy storage/conversion systems.

References

[1] S. Chou, W. Yang, K. Chua, J. Li, K. Zhang, Appl. Energ. 88 (2011) 1-16.

[2] M. Safdar, J. Jänis, S. Sanchez, Lab Chip 16 (2016) 2754-2758.

[3] J. P. Esquivel, F. Del Campo, J.G. de la Fuente, S. Rojas, N. Sabate, Energ. Environ. Sci. 7 (2014) 1744-1749.

[4] O. A. Ibrahim, P. Alday, N. Sabaté, J. P. Esquivel, E. Kjeang, J. Electrochem. Soc. 164 (2017) A2448-A2456.

[5] Y. Liu, Q. Sun, W. Li, K. R. Adair, J. Li, X. Sun, Green Energ. Environ. 2 (2017) 246-277.

[6] L. Fan, H. Lu, J. Leng, Electrochim. Acta 165 (2015) 22-28.

[7] Q. Li, N. J. Bjerrum, J. Power Sources 110 (2002) 1-10.

[8] S. Yang, H. Knickle, J. Power Sources 112 (2002) 162-173.

[9] N. Jayaprakash, S. K. Das, L. A. Archer, Chem. Commun. 47 (2011) 12610-12612.

[10] D. J. Kim, D.-J. Yoo, M. T. Otley, A. Prokofjevs, C. Pezzato, M. Owczarek, S. J. Lee, J. W. Choi, J. F. Stoddart, Nat. Energy (2018) 1.

[11] F. Cheng, J. Chen, Chem. Soc. Rev. 41 (2012) 2172-2192.

[12] M. Mokhtar, M. Z. M. Talib, E. H. Majlan, S. M. Tasirin, W. M. F. W. Ramli, W. R. W. Daud, J. Sahari, J. Ind. Eng. Chem. 32 (2015) 1-20.

[13] Z. P. Cano, D. Banham, S. Ye, A. Hintennach, J. Lu, M. Fowler, Z. Chen, Nat. Energy 3 (2018) 279.

[14] H. El Shayeb, F. A. El Wahab, S .Z. El Abedin, Corros. Sci. 43 (2001) 655-669.

[15] M. Nestoridi, D. Pletcher, J. A. Wharton, R. J. Wood, J. Power Sources 193 (2009) 895-898.

[16] I. Smoljko, S. Gudić, N. Kuzmanić, M. Kliškić, J. Appl. Electrochem. 42 (2012) 969-977.

[17] D. Egan, C. P. De León, R. Wood, R. Jones, K. Stokes, F. Walsh, J. Power Sources 236 (2013) 293-310.

[18] J. Ma, J. Wen, J. Gao, Q. Li, J. Electrochem. Soc. 161 (2014) A376-A380.

[19] D. Gelman, B. Shvartsev, Y. Ein-Eli, J. Mater. Chem. A 2 (2014) 20237-20242.

[20] M. Kar, T. J. Simons, M. Forsyth, D.R. MacFarlane, Phys. Chem. Chem. Phys. 16 (2014) 18658-18674.

[21] R. Revel, T. Audichon, S. Gonzalez, J. Power Sources 272 (2014) 415-421.

[22] H. Wang, S. Gu, Y. Bai, S. Chen, F. Wu, C. Wu, ACS Appl. Mater. Interfaces 8 (2016) 27444-27448.

[23] G.-R. Zhang, S. Wöllner, Appl. Catal. B-Environ. 222 (2018) 26-34.

[24] L.-L. Shen, G.-R. Zhang, S. Miao, J. Liu, B.-Q. Xu, ACS Catal. 6 (2016) 1680-1690.

[25] H. Pang, Y. Wang, M. Zhao, Q. Zhao, Q. Li, Nanoscale (2018).

[26] X. Li, Y. Fang, X. Lin, M. Tian, X. An, Y. Fu, R. Li, J. Jin, J. Ma, J. Mater. Chem. A 3 (2015) 17392-17402.

[27] G.-L. Chai, K. Qiu, M. Qiao, M.-M. Titirici, C. Shang, Z. Guo, Energ. Environ. Sci. 10 (2017) 1186-1195.

[28] S. Liu, Z. Wang, S. Zhou, F. Yu, M. Yu, C. Y. Chiang, W. Zhou, J. Zhao, J. Qiu, Adv. Mater. 29 (2017) 1700874.

[29] H. Peng, F. Liu, X. Liu, S. Liao, C. You, X. Tian, H. Nan, F. Luo, H. Song, Z. Fu, P. Huang, ACS Catal. 4 (2014) 3797-3805.

[30] X.-H. Yan, B.-Q. Xu, J. Mater. Chem. A 2 (2014) 8617-8622.

[31] T. Y. Ma, J. Ran, S. Dai, M. Jaroniec, S. Z. Qiao, Angew. Chem. Int. Ed. 54 (2015) 4646-4650.

[32] J. Zhang, Z. Zhao, Z. Xia, L. Dai, Nat. Nanotechnol. 10 (2015) 444.

[33] S. Li, C. Cheng, H. W. Liang, X. Feng, A. Thomas, Adv. Mater. 29 (2017) 1700707.

[34] C. Tang, B. Wang, H. F. Wang, Q. Zhang, Adv. Mater. 29 (2017) 1703185.

[35] Y. Xu, Y. Zhao, J. Ren, Y. Zhang, H. Peng, Angew. Chem. 128 (2016) 8111-8114.

[36] J. Li, Z. Zhou, K. Liu, F. Li, Z. Peng, Y. Tang, H. Wang, J. Power Sources 343 (2017) 30-38.

[37] M. Zhang, Q. Dai, H. Zheng, M. Chen, L. Dai, Adv. Mater. 30 (2018) 1705431.

[38] K. B. Lee, J. Micromech. Microeng. 15 (2005) S210-S214.

[39] K. B. Lee, J. Micromech. Microeng. 16 (2006) 2312-2317.

[40] G. Nyström, A. Razaq, M. Strømme, L. Nyholm, A. Mihranyan, Nano Lett. 9 (2009) 3635-3639.

[41] H. Liu, R. M. Crooks, Anal. Chem. 84 (2012) 2528-2532.

[42] N. K. Thom, K. Yeung, M. B. Pillion, S. T. Phillips, Lab Chip 12 (2012) 1768-1770.

[43] Y. Koo, J. Sankar, Y. Yun, Biomicrofluidics 8 (2014) 054104.

[44] M. Mohammadifar, S. Choi, Adv. Mater. Technol. 2 (2017) 1700127.

[45] A. Böhm, F. Carstens, C. Trieb, S. Schabel, M. Biesalski, Microfluid. Nanofluid. 16 (2014) 789-799.

[46] F. Sharifi, S. Ghobadian, F. R. Cavalcanti, N. Hashemi, Renew. Sust. Energ. Rev. 52 (2015) 1453-1472.

[47] A. Böhm, M. Biesalski, MRS Bull. 42 (2017) 356-364.

[48] M. M. Gong, D. Sinton, Chem. Rev. 117 (2017) 8447-8480.

[49] M. Liu, J. Wu, Y. Gan, D. A. Hanaor, C. Chen, Langmuir 32 (2016) 9899-9904.

[50] E. W. Washburn, Phys. Rev. 17 (1921) 273.

[51] S. Mendez, E. M. Fenton, G. R. Gallegos, D. N. Petsev, S. S. Sibbett, H. A. Stone, Y. Zhang, G. P. López, Langmuir 26 (2009) 1380-1385.

[52] L.-L. Shen, G.-R. Zhang, W. Li, M. Biesalski, B. J. Etzold, ACS Omega 2 (2017) 4593-4603.

[53] L.-L. Shen, G.-R. Zhang, T. Venter, M. Biesalski, B. J. Etzold, Electrochim. Acta 298 (2019) 389-399.

[54] F. Lima, J. Zhang, M. Shao, K. Sasaki, M. Vukmirovic, E. Ticianelli, R. Adzic, J. Phys. Chem. C 111 (2007) 404-410.

[55] M. H. Seo, S. M. Choi, H. J. Kim, W. B. Kim, Electrochem. Commun. 13 (2011) 182-185.

[56] D. Chu, R. F. Savinell, Electrochim. Acta 36 (1991) 1631-1638.

[57] R. Davis, G. Horvath, C. Tobias, Electrochim. Acta 12 (1967) 287-297.

[58] H. Li, H. Liu, Z. Jong, W. Qu, D. Geng, X. Sun, H. Wang, Int. J. Hydrogen Energy 36 (2011) 2258-2265.

[59] N. Mittal, F. Ansari, K. Gowda. V, C. Brouzet, P. Chen, P. T. Larsson, S. V. Roth, F. Lundell, L. Wagberg, N. A. Kotov, ACS nano 12 (2018) 6378-6388.

[60] Y. Wang, H. Kwok, W. Pan, H. Zhang, D. Y. Leung, J. Power Sources 414 (2019) 278-282.

[61] Y. Wang, H. Y. Kwok, W. Pan, H. Zhang, X. Lu, D. Y. Leung, Appl. Energ. 251 (2019) 113342.

[62] H. Wang, D. Y. Leung, M. K. Leung, M. Ni, Energy Fuels 24 (2010) 3748-3753.

[63] Q. Hong, H. Lu, Sci. Rep. 7 (2017) 3378.

[64] L. Xu, H. Fan, L. Huang, J. Xia, S. Li, M. Li, H. Ding, K. Huang, Electrochim. Acta 239 (2017) 1-9.

[65] J. Ryu, H. Jang, J. Park, Y. Yoo, M. Park, J. Cho, Nat. Commun. 9 (2018) 3715.

[66] Z. Zhang, C. Zuo, Z. Liu, Y. Yu, Y. Zuo, Y. Song, J. Power Sources 251 (2014) 470-475.

[67] S. Choi, D. Lee, G. Kim, Y. Y. Lee, B. Kim, J. Moon, W. Shim, Adv. Funct. Mater. 27 (2017).

[68] Y. Liu, Q. Sun, X. Yang, J. Liang, B. Wang, A. Koo, R. Li, J. Li, X. Sun, ACS Appl. Mater. Interfaces 10 (2018) 19730-19738.

[69] J. Fu, D. U. Lee, F. M. Hassan, L. Yang, Z. Bai, M.G. Park, Z. Chen, Adv. Mater. 27 (2015) 5617-5622.

[70] X. Chen, B. Liu, C. Zhong, Z. Liu, J. Liu, L. Ma, Y. Deng, X. Han, T. Wu, W. Hu, Adv. Energy Mater. 7 (2017) 1700779.

[71] G. Liu, J. Y. Kim, M. Wang, J. Y. Woo, L. Wang, D. Zou, J. K. Lee, Adv. Energy Mater. (2018) 1703652.

[72] Y. Li, H. Dai, Chem. Soc. Rev. 43 (2014) 5257-5275.

[73] G.-R. Zhang, M. Munoz, B. J. Etzold, ACS Appl. Mater. Interfaces 7 (2015) 3562-3570.

[74] G.-R. Zhang, M. Munoz, B. J. Etzold, Angew. Chem., Int. Ed. 55 (2016) 2257-2261.

[75] H. Li, Y. Tang, Z. Wang, Z. Shi, S. Wu, D. Song, J. Zhang, K. Fatih, J. Zhang, H. Wang, J. Power Sources 178 (2008) 103-117.

[76] C. J. Brett, N. Mittal, W. Ohm, M. Gensch, L. P. Kreuzer, V. Körstgens, M. Månsson, H. Frielinghaus, P. Müller-Buschbaum, L. D. Söderberg, Macromolecules 52 (2019) 4721-4728.

[77] A. Isogai, T. Saito, H. Fukuzumi, Nanoscale 3 (2011) 71-85.

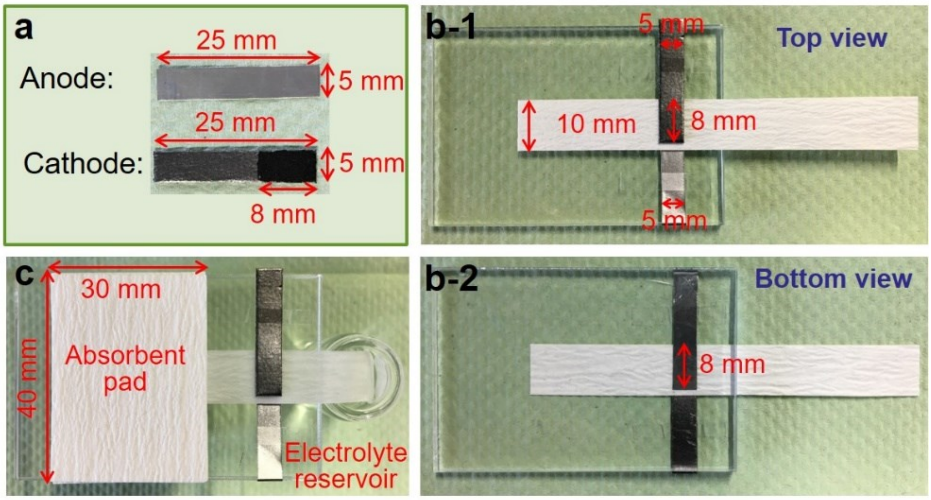

Figure S6.1 (a) Dimensions of the anode and cathode electrodes. (b) Display of the prototypical paper-based μAl-air battery from top and bottom view. (c) A prototypical paper-based μAl-air battery during discharge.

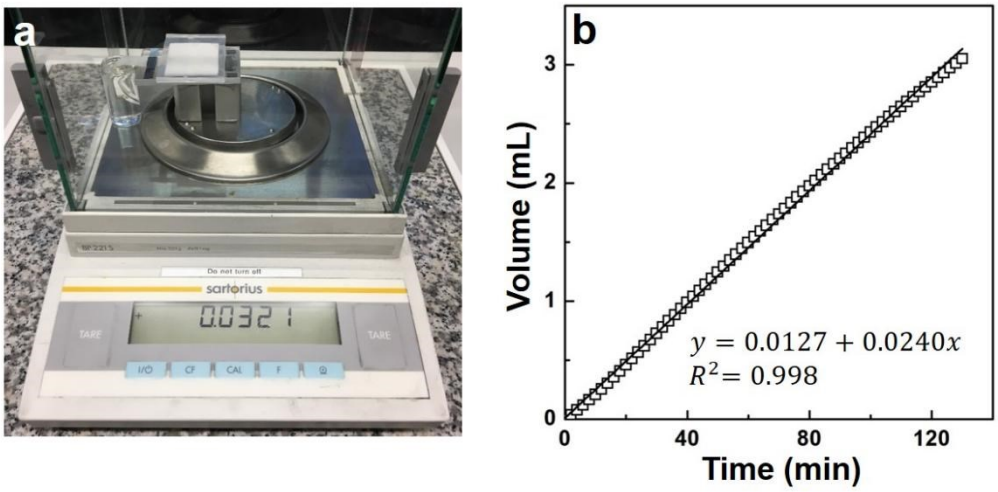

Figure S6.2 (a) Flow rate measurement of the electrolyte (1.5 M KOH solution) on paper channel (VWR grade 417). (b) The volume of the electrolyte accumulated on absorbent pads was plotted against elapsed time. The flow rate calculated by linear regression is marked.

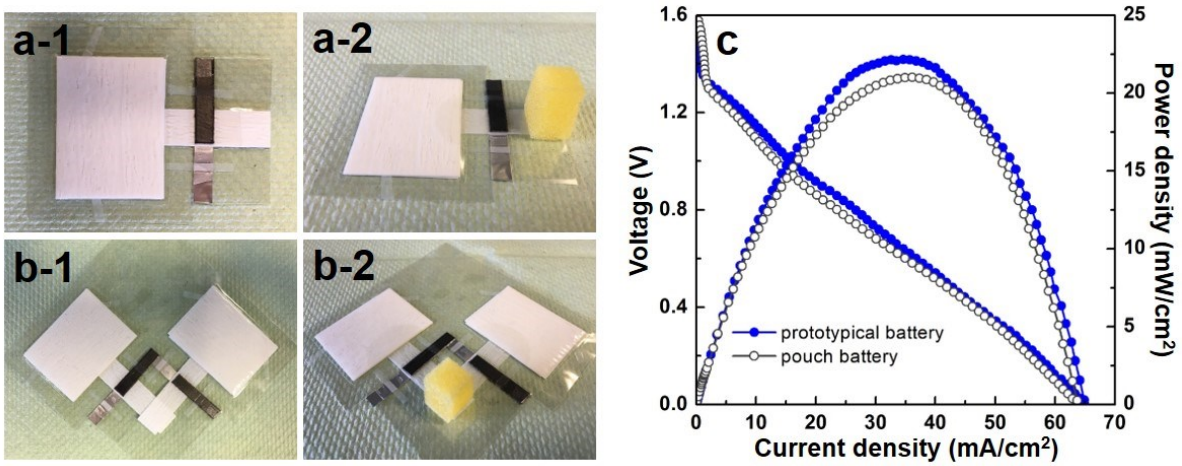

Figure S6.3 A paper-based μAl-air pouch battery before (a-1) and during discharging (a-2). Two paper-based μAl-air pouch batteries connected in series before (b-1) and during discharging (b-2). (c) Polarization (*V*-*I*) and power density curve of a single paper-based μAl-air battery in pouch configuration.

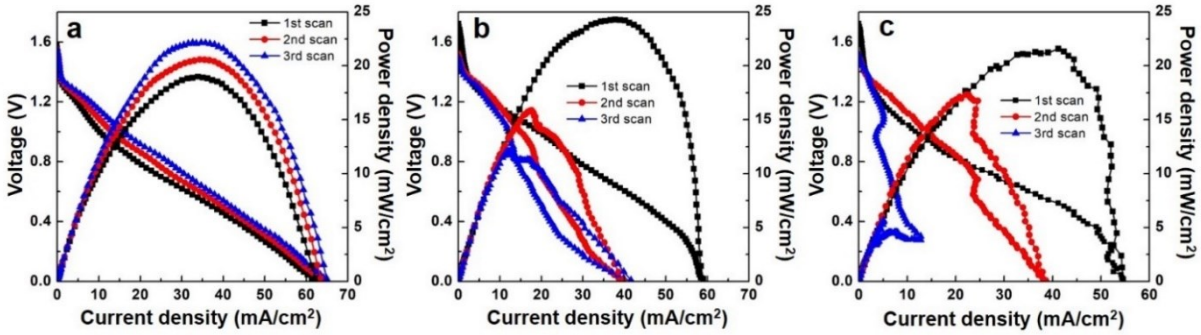

Figure S6.4 Polarization (*V*-*I*) and power density curves of paper-based μAl-air battery with 1.5 M (a), 2.0 M (b) and 2.5 M (c) KOH solution by continuous staircase linear scan voltammetry.

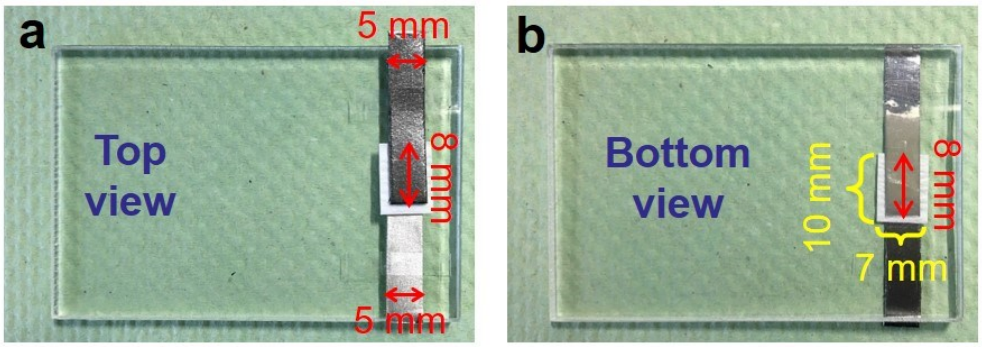

Figure S6.5 Display of the prototypical paper-based non-fluidic Al-air battery from top (a) and bottom (b) view. Reaction area for both anode and cathode electrodes are 8×5 mm^2. The size of paper is 10×7 mm^2.

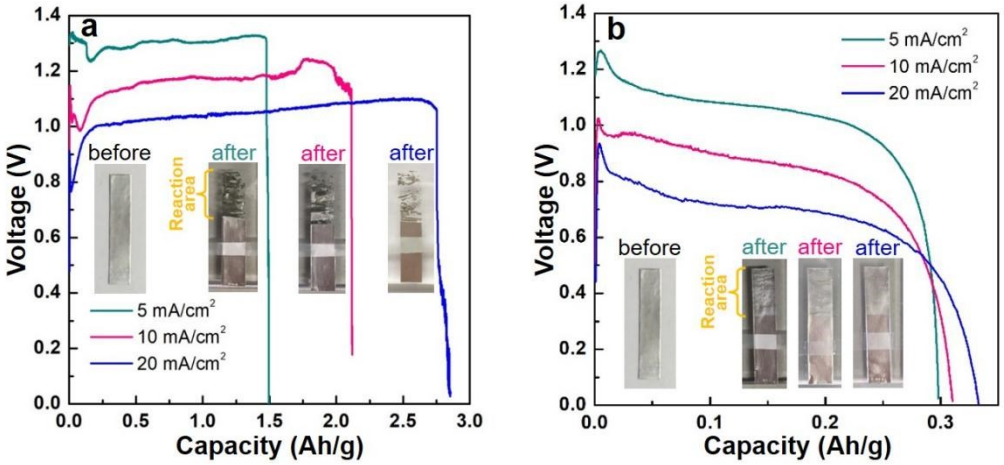

Figure S6.6 Discharge curves of paper-based μAl-air battery (a) and non-fluidic Al-air battery (b) under different current density (5, 10, 20 mA/cm^2). The insets are the optical photos of the anode aluminum foil after discharge.

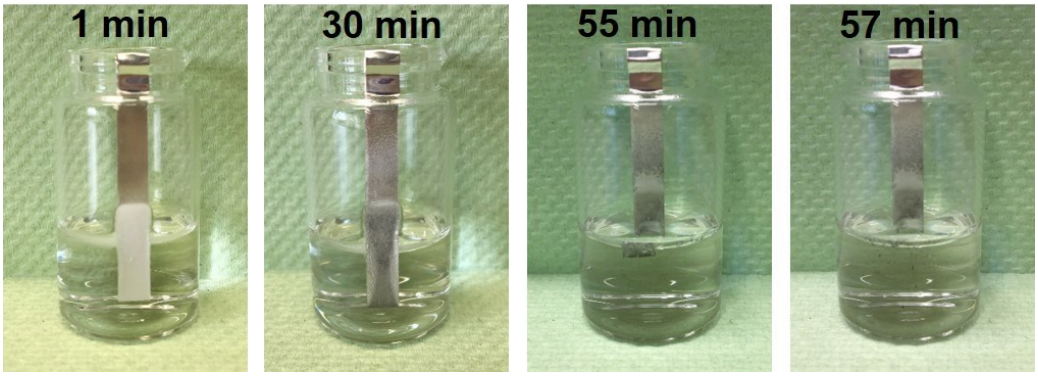

Figure S6.7 Aluminum foil (size 8×5 mm^2) immersed in 1.5 M KOH solution.

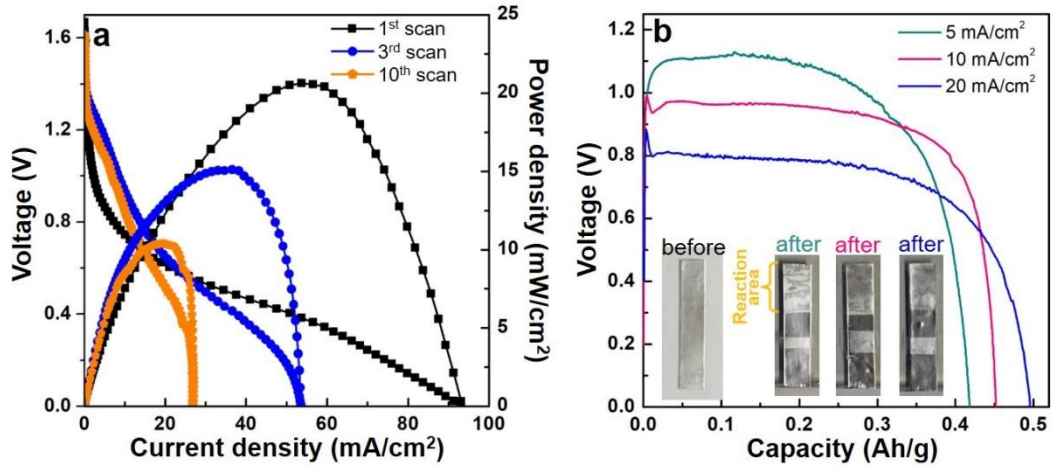

Figure S6.8 Performance of non-fluidic Al-air battery using gas diffusion layer air electrode at the cathode. (a) Polarization (*V*-*I*) and power density curves recorded at different scan numbers. (b) Discharge curves of paper-based and non-fluidic Al-air battery using gas diffusion layer air electrode under different current density (5, 10, 20 mA/cm^2). The insets are the optical photos of the anode aluminum foil after discharge.

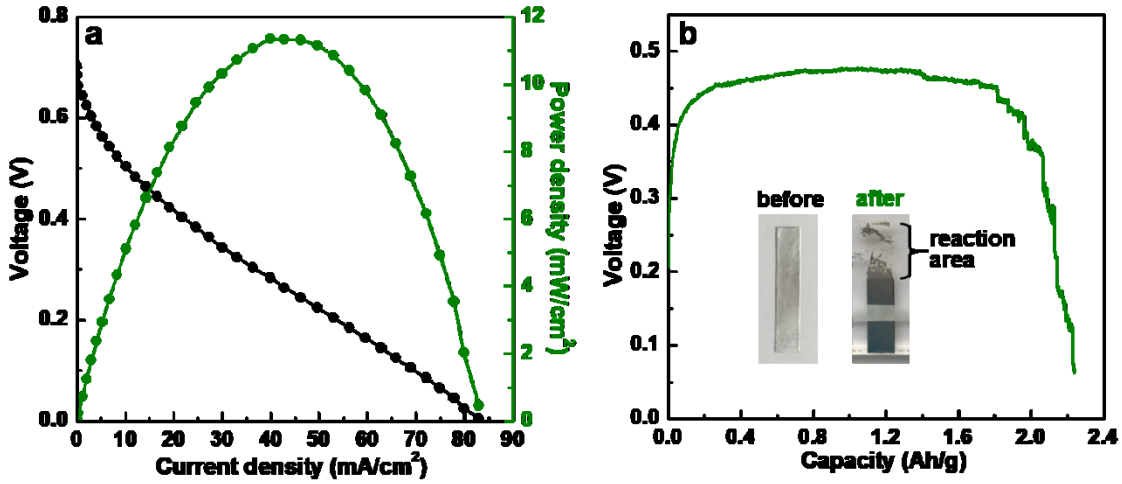

Figure S6.9 Polarization (*V*-*I*) and power density curve (a) and discharge curve (b) of the paper-based μAl-air battery by using 2 M NaCl as electrolyte. The insets are the optical photos of the anode aluminum foil after discharge.

Table S6.1 Comparisons of the metal-air batteries

Anode	Cathode	Electrolyte	OCV[a] (V)	Maximum Power density (mW/cm^2)	Discharge V (V) @ I (mA/cm^2)[b]	Specific capacity (Ah/g)	Energy density (Wh/kg)	Features	Ref[i]
Al foil	MnO_2 in carbon	EMIm(HF)$_{2.3}$F[c]			1.1@1.5	2.1[f]	2300[f]	Primary Al-air battery with non-aqueous electrolyte	[1]
Al	N, S doped porous carbon	6 M KOH	1.64	46	0.9@20	0.288	260	Primary Al-air battery	[2]
Al	$La_{0.7}(Sr_{0.15}Pd_{0.15})MnO_3$	4 M KOH	1.8	265.6	-	-	-	Primary Al-air battery	[3]
Al	carbon fiber paper supported Ag	4 M NaOH	1.85	109.5	1.56@30	2.78 [f]	4340 [f]	Primary Al-air battery	[4]
Carbon treated Al	MnO_2 pasted on Ni mesh	2 M NaCl	-	-	0.4@10	1.2	480	Primary Al-air battery	[5]
Al mesh	La_2O_3, SrO, MnO_2 and carbon on Ni foam	KOH gel	-	91.13	1.2@18	1.166 [f]	1230 [f]	All-solid-state battery	[6]
Ultrafine-grained Al	Ag powder on Ni mesh	2 M NaCl	-	-	0.388@10	2.72 [f]	960 [f]	Primary Al-air battery	[7]
		4 M KOH	-	-	1.45@10	2.48 [f]	3600 [f]		
Al alloy 6061	silver manganate nanoplates loaded air electrode	6 M KOH	1.4	105	0.91@100	2.84 [f]	2550 [f]	Primary Al-air flow battery (electrolyte flow rate 100 mL/min) controlled by a pump	[8]
					1.10@50	2.64 [f]	2540 [f]		
Al wire	MWCNT coated paper	BPS[c]	0.7	0.38[d]	-	-	-	Cable-shaped flexible battery	[9]
Al spring	Ag coated CNTc sheet	Hydrogel PVA[c] KOH	1.7	1.33	1.25@0.5	0.935[f]	1168[f]	All-solid-state, fiber-shape, stretchable battery	[10]
Al foil	Carbon on steel mesh	1.5 M KOH	1.27	0.6				Disposable, small-size, paper-based battery	[11]
Al foil	Carbon black	12 wt% NaCl	0.7	0.015	0.54@0.005	0.496[f]	270[f]	Shape-reconfigurable battery	[12]
						0.128[g]	69[g]		
Al foil	Mn_3O_4/C on carbon paper	SiO_2-modified chitosan hydrogel	1.43	3.8	1.05@1	0.289[f]	303[f]	Al-air coin battery with SiO_2-modified chitosan hydrogel membrane	[13]
Al foil	Carbon paper	5 M NaOH	1.6	21	0.9@10	1.273[g]	1150[g]	Paper-based Al-air battery with suppressed Al corrosion	[14]
Al foil	MnO_2/CNT[c] on carbon paper	4 M NaCl	1.5	-	0.6@1	2.462[g]	1480[g]	Paper-based flexible battery	[15]
Al ink	MnO_2/CNT[c] on paper	4 M NaCl	0.8	-	0.6-0.2@1	0.814[g]	-	Paper-based paintable battery	
Zn film	LaNiO3/NCNT[c]	PVA[c] gelled KOH	1.3	28	1.2@1	0.45[g]	581[g]	Flexible, polymer-electrolyte, rechargeable battery	[16]
Spiral Zn plate	Fe/N/C on air electrode	alkline gel polymer	1.14	-	0.8@0.1	4.5 Ah/L[h]	3.6 Wh/L[h]	All-solid-state cable-type flexible battery	[17]
Zn spring	RuO_2 on CNT[c]	Hydrogel polymer	1.29	-	1@1[e]	6 Ah/L[h]	5.7 Wh/L[h]	Rechargeable, flexible, stretchable, fiber-shape battery	[18]

Zn foil	NCNF[a] film cathode	Alkaline PVA[c] gel	-	-	1.0@2	0.378[f]	378[f]	Flexible battery with good mechanical and cycling stability	[19]
Zn foil	Co/N/O tri-doped graphene mesh	Alkaline PVA[c] gel	1.45	28	1.19@1.0	-	-	Rechargeable, bendable, flexible, solid battery	[20]
Zn film	Ultrathin Co_3O_4 on carbon cloth	PVA[c] gel KOH	1.3	17	1.05@2	0.542[f]	546[f]	Flexible thin Zn-air battery	[21]
Zn plate	$CuCo_2S_4$ nanosheets	PVA[c] gel KOH	1.2	-	1.28@1.0	0.331[f]	424[f]	Flexible all solid Zn-air battery	[22]
EGILM[a]	Carbon fiber@Pt	PAA[c] gel KOH	1.85	1.25	1.2@0.5	0.21[f]	250[f]	Cable-shaped, soft, elastic, flexible liquid metal-air battery	[23]
Al foil	Pd/C on graphite foil	1.5 M KOH	1.55	22.5	1.05@20	4.1 Ah/L[h]	4.3 Ah/L[h]	Small, thin, low-cost paper-based μAl-air battery with high power and energy density (electrolyte flow rate 24 μL/min)	This work
					1.05@20	2.75[g]	2900[g]		
					1.17@10	2.11[g]	2470[g]		
					1.30@5	1.47[g]	1910[g]		
		2 M NaCl	0.70	11.3	0.46@20	2.20[g]	1010[g]		

[a] Open circuit voltage

[b] Discharge voltage (V) at discharge current (mA/cm^2)

[c] $EMIm(HF)_{2.3}F$: 1-ethyl-3-methylimidazolium oligo-fluoro-hydrogenate; BPS: phosphate-buffered saline; CNT: carbon nanotubes; NCNT: nitrogen-doped carbon nanotubes; PAA: poly acrylic acid; NCNF: nanoporous carbon nanofiber films; PVA: polyvinyl alcohol; EGILM: Eutectic gallium-indium liquid metal.

[d] 0.38 mW/cm.

[e] 1 V at 1 A/g.

[f] The capacity and energy density was calculated based on the consumed Al mass.

[g] The capacity and energy density was calculated based on the whole Al mass.

[h] The capacity and energy density was calculated based on the whole volume of the device.

[i] The primary batteries are shown in black text (Ref 1-8). The miniaturized batteries are shown in blue text (Ref 9-23).

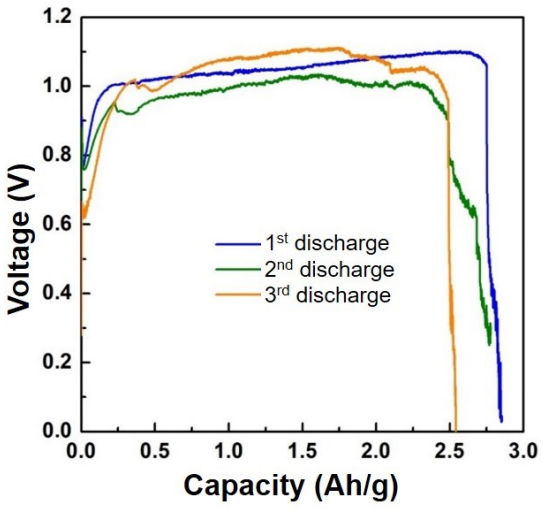

Figure S6.10 Mechanically recharging tests. Discharge curves of three paper-based μAl-air battery by using the same cathode electrode.

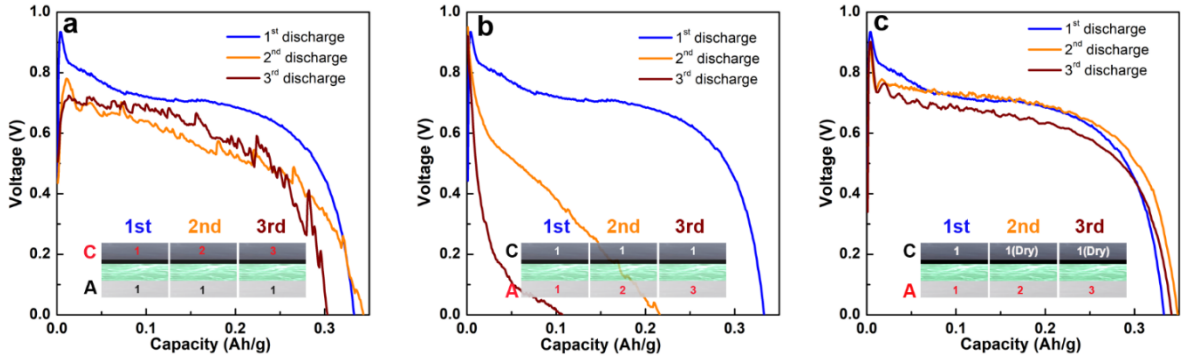

Figure S6.11 (a) Discharge curves of three paper-based non-fluidic Al-air battery by using the same anode electrode, but new cathode electrode as well as paper and electrolyte. (b, c) Discharge curves of three paper-based non-fluidic Al-air battery by using the same cathode electrode, but new anode electrode as well as paper and electrolyte; (b) the cathode was used without drying; (c) the cathode was dried in vacuum for 2 h after each discharge, and then reassembled into a non-fluidic Al-air battery for the next discharge.

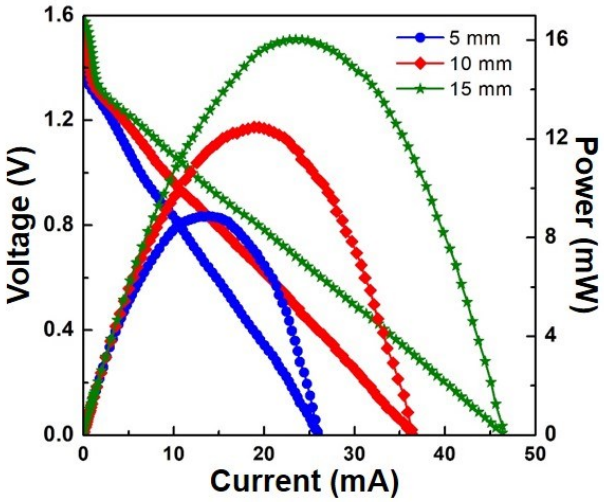

Figure S6.12 Polarization (*V*-*I*) and power density curves of paper-based μAl-air batteries with different electrode sizes.

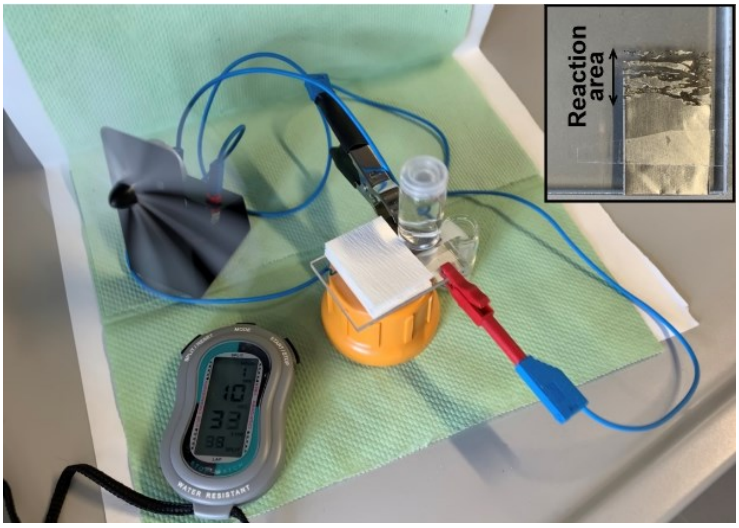

Figure S6.13 Running time measurement of a mini-fan (power rating 10 mW) powered by a paper-based μAl-air battery (geometric electrode active area: 8×15 mm^2). The inset shows that after 70 min discharge the Al anode is almost fully consumed.

References

[1] D. Gelman, B. Shvartsev, Y. Ein-Eli, J. Mater. Chem. A 2 (2014) 20237-20242.

[2] L. Xu, H. Fan, L. Huang, J. Xia, S. Li, M. Li, H. Ding, K. Huang, Electrochim. Acta 239 (2017) 1-9.

[3] Y. Xue, S. Sun, Q. Wang, H. Miao, S. Li, Z. Liu, Electrochim. Acta 230 (2017) 418-427.

[4] Q. Hong, H. Lu, Sci. Rep. 7 (2017) 3378.

[5] M. Pino, D. Herranz, J. Chacon, E. Fatás, P. Ocón, J. Power Sources 326 (2016) 296-302.

[6] Z. Zhang, C. Zuo, Z. Liu, Y. Yu, Y. Zuo, Y. Song, J. Power Sources 251 (2014) 470-475.

[7] L. Fan, H. Lu, J. Leng, Electrochim. Acta 165 (2015) 22-28.

[8] J. Ryu, H. Jang, J. Park, Y. Yoo, M. Park, J. Cho, Nat. Commun. 9 (2018) 3715.

[9] G. Fotouhi, C. Ogier, J.-H. Kim, S. Kim, G. Cao, A.Q. Shen, J. Kramlich, J.-H. Chung, J. Micromech. Microeng. 26 (2016) 055011.

[10] Y. Xu, Y. Zhao, J. Ren, Y. Zhang, H. Peng, Angew. Chem. 128 (2016) 8111-8114.

[11] A. Avoundjian, V. Galvan, F.A. Gomez, Micromachines 8 (2017) 222.

[12] S. Choi, D. Lee, G. Kim, Y.Y. Lee, B. Kim, J. Moon, W. Shim, Adv. Funct. Mater. 27 (2017).

[13] Y. Liu, Q. Sun, X. Yang, J. Liang, B. Wang, A. Koo, R. Li, J. Li, X. Sun, ACS Appl. Mater. Interfaces 10 (2018) 19730-19738.

[14] Y. Wang, H.Y. Kwok, W. Pan, H. Zhang, X. Lu, D.Y. Leung, Appl. Energ. 251 (2019) 113342.

[15] Y. Wang, H. Kwok, W. Pan, H. Zhang, D.Y. Leung, J. Power Sources 414 (2019) 278-282.

[16] J. Fu, D.U. Lee, F.M. Hassan, L. Yang, Z. Bai, M.G. Park, Z. Chen, Adv. Mater. 27 (2015) 5617-5622.

[17] J. Park, M. Park, G. Nam, J.s. Lee, J. Cho, Advanced Materials 27 (2015) 1396-1401.

[18] Y. Xu, Y. Zhang, Z. Guo, J. Ren, Y. Wang, H. Peng, Angew. Chem. Int. Ed. 54 (2015) 15390-15394.

[19] Q. Liu, Y. Wang, L. Dai, J. Yao, Advanced Materials 28 (2016) 3000-3006.

[20] C. Tang, B. Wang, H.F. Wang, Q. Zhang, Adv. Mater. 29 (2017) 1703185.

[21] X. Chen, B. Liu, C. Zhong, Z. Liu, J. Liu, L. Ma, Y. Deng, X. Han, T. Wu, W. Hu, Adv. Energy Mater. 7 (2017) 1700779.

[22] Y. Li, J. Yin, L. An, M. Lu, K. Sun, Y.-Q. Zhao, F. Cheng, P. Xi, Nanoscale 10 (2018) 6581-6588.

[23] G. Liu, J.Y. Kim, M. Wang, J.Y. Woo, L. Wang, D. Zou, J.K. Lee, Adv. Energy Mater. (2018) 1703652.

7 Summary, challenges and outlook

In this thesis, we attempted to use paper-based microfluidics as a general framework to design and fabricate miniaturized electrochemical devices for in-field environmental analysis and portable power sources. As our main contributions we perceive:

- A miniaturized microfluidic electrochemical carbon-based sensor (μCS) for heavy metal detection was assembled on paper using pristine graphite foil as electrodes. The μCS is easy to fabricate, low cost, robust and highly sensitive without introducing any modifier (e.g., mercury and bismuth) during the sensing process, which would benefit from the paper-based microfluidic configuration combined with the novel 3D electrode layout. This simple and portable μCS is capable to detect heavy metal ions (Cd^{2+} and Pd^{2+}) in aqueous solution with wide linear range and low limit of detections. The μCS also exhibits stable and reproducible sensing performance up to 10 repetitive measurements. Attempts were also made to test the sensing performance of the μCS under more complex conditions, e.g., in commercial mineral water. The results show that mineral ions in the commercial mineral water imposes little impact on the sensing performance of the μCS, demonstrating the great potential of the μCS to be used in real application.

- A low-cost membrane-less paper-based microfluidic fuel cell was fabricated. Several key factors, including electrode position, concentration of supporting electrolyte, concentration of fuel/oxidant, catalyst loading and size of the electrode have been systematically studied to develop high-performing paper-based microfluidic fuel cells. The main influence on the cell performance is the depletion of reactant along the electrode and mass transfer limitation through the catalyst layer when low concentration of reactants and high loading of catalyst are used, respectively. Moreover, it is the first time to unravel the influence of paper channel properties (e.g., pore size) on fuel cell performance by investigating the microfluidic behavior on Y shaped paper channels with different pore size. Paper channel with larger pore size is able to deliver reactants with higher flow rates, which reduces the reactant depletion and suppresses the fuel crossover by diffusion, and results in higher power output as well as open circuit voltage. We believe that these findings may have implications for understanding electrolyte flow behavior on paper, building better microfluidic paper-based fuel cells, and could be expanded to other paper-based microfluidic devices.

- A simple, inexpensive and high-performing paper-based microfluidic aluminum-air battery was fabricated. The electrolyte is stored separately from the electrodes before battery discharge, thus preventing self-discharge and prolonging the battery self-life. The Al-air battery can discharge by introducing electrolyte into the paper channel, which is capable to continuous transfer oxygen containing electrolyte to the electrodes, where redox reactions take place. On one side, the flow electrolyte largely prevents the anode surface passivation by reducing the accumulation of non-reactive discharge products. On the other, the paper-based microfluidic design eliminates the use of expensive and complex air electrode by efficiently shuttling oxygen from ambient air to the cathode catalyst, which makes it possible to reduce the whole device cost and minimize the device size. In addition, the pore clogging issues caused by carbonate formation can be overcome in the paper-based microfluidic Al-air battery, since the open cell structure for oxygen transfer to the air cathode can be omitted, and the battery can be assembled by simple lamination technique.

The development paper-based microfluidics and insight into its mechanism have opened up new opportunities for fabrication of low-cost, flexible, portable, environmental-friendly, self-pumping microfluidic electrochemical devices. However, research on paper-based microfluidic electronics is still in the early stage for commercialization. A lot of efforts still have to be done to transform the lab-scale paper-based microfluidic electrochemical device into a commercial product:

- For the paper-based microfluidic electrochemical sensing devices, sample preparation such as dilution and pH controlling of the analyte is usually required in the sensing process, which is complex for users without expertise. The paper-based microfluidic electrochemical sensors are usually operated with a potentiostat, which are not commonly available in people's daily life, and result interpretation by reading current or potential is unfamiliar to general people without professional knowledge. To meet the requirement for real application, the electrochemical sensing device should integrate the sample preparation, electrodes for sensing, power sources, electro measurement method and an understandable data reader.

- For the paper-based microfluidic power sources, strong acid or alkaline electrolyte is usually need for battery/cell discharge, which is considered to be unsafe and inconvenient for users. The ideal protocol is to store the redox species and electrolyte inside the device and activate the battery or fuel cell by directly adding water or neutral solution available in daily

life, such as NaCl solution. Other limitations come from the catalysts and electrodes, especially for the cathode part. The slow oxygen reduction reaction taking place at the three-phase interfaces demands the design of gas diffusion electrode, as well as high performing platinum-based catalyst, both of which are regarded as the most costly part in the battery/cell system. Fortunately, many research groups are working on developing non-precious metal catalyst. In this thesis, paper-based microfluidic system proves to be an alternative to air gas diffusion electrode toward continuous mass transfer of oxygen.

- Although paper has been used as an effective, low-cost and flexible microfluidic carrier in fabrication of various microfluidic devices, the achievements in this field have strong application bent yet lack of deep theoretical investigation. In the most existing paper-based microfluidic devices, paper is simply employed as a fluid channel, electrode separator or electrolyte/analyte reservoir. Whereas few work dedicates to understanding the relationship between paper properties (e.g., physical architecture and chemical composition) and the electrochemical performance. Therefore, in the future, insight into the properties of paper and the microfluidic behavior on paper, as well as fabrication of novel functional paper material might be the key to develop high-performing paper-based microfluidic electrochemical device toward commercial application.

Even though the paper-based microfluidic electronics still face various problems to be become commercialized, we believe that it only a matter of time to solve the above mentioned issues. In the age of big data, the Internet of Things (IoT) uses large number of miniaturized sensors to collect data and then transfer over the internet to a central cloud-based computing resource for further analysis. In many fields, such as food industry, environmental monitoring, agriculture and health care, the IoT sensors are moving toward to flexible, renewable, biodegradable as well as low-cost materials—paper. In addition, it is also crucial to develop paper-based power sources that can be coupled with the paper-based IoT sensors for long time running. In the future, 3D printing, electrospinning techniques may play an important role in manufacturing paper-based microfluidic electronics in large scale, and computational techniques may facilitate the development of paper-based microfluidic electronics by simulating the microfluidic behavior and predicting its effect on the device performance. In summary, we are heading toward a new generation of microfluidic electronics base on paper. Along with the continuous deepening of research, the paper-based microfluidic

electrochemical devices will finally be employed in practical applications, and bring convenience and benefit to people's lives.

Publications

Publications during Ph.D. study:

[1] **L.-L Shen**, G.-R. Zhang, B. J. M. Etzold. Paper-based microfluidics for electrochemical applications. *ChemElectroChem* DOI: 10.1002/celc.201901495.

[2] **L.-L Shen**, G.-R. Zhang, M. Biesalski, B. J. M. Etzold. Paper-based microfluidic aluminum-air batteries: toward next-generation miniaturized power supply. *Lab on a Chip* 19 (2019) 3438-3447.

[3] **L.-L Shen**, G.-R. Zhang, T. Venter, M. Biesalski, B. J. M. Etzold. Towards best practices for improving paper-based microfluidic fuel cells. *Electrochimica Acta* 298 (2019) 389-399.

[4] **L.-L Shen**, G.-R. Zhang, W. Li, M. Biesalski, B. J. M. Etzold. Modifier-free microfluidic electrochemical sensor for heavy-metal detection. *ACS Omega* 2 (2017) 4593-4603.

Publications during M.S. and B.S. study:

[1] **L.-L Shen**, G.-R. Zhang, S. Miao, J. Liu, B. B.-Q. Xu, Core-shell nanostructured Au@Ni$_m$Pt$_2$ electrocatalysts with enhance activity and durability for oxygen reduction reaction. *ACS Catalysis* 6 (2016) 1680-1690.

[2] X.-M. Kong, **L.-L Shen**. Selectivity control of ethanol gas-phase oxidation over nanoporous gold. *Catalysis Communications* 24 (2012) 34-37.

[3] L. Wang, **L.-L Shen**, X. Xu, L. Xu, Y. Qian. Facile synthesis of uniform *h*-BN nanocrystals and their application as a catalyst support toward the selective oxidation of benzyl alcohol. *RSC Advances* 2 (2012) 10689-10693.

Acknowledgments

Firstly, I would like to address my sincere gratitude to my supervisor, Prof. Dr.-Ing. Bastian J. M. Etzold, for his insightful advice, patient guidance and everlasting encouragement during my work in Technique University Darmstadt. His broad knowledge and enthusiastic attitude toward scientific research will always inspire me to keep on exploring and seeking for truth.

I would also like to express my deepest thanks to Dr. Gui-Rong Zhang for his generous technical assistance during the experiment, insightful view during the discussion, and enduring support with the thesis writing.

I wish to thank Prof. Dr. Markus Biesalski for his valuable suggestions and kind help as well as the long time scientific collaboration.

I further wish to thank all the past and present staff in the Etzold's group for their warm help in both my study and my daily life.

I sincerely thank my family and friends for their eternal support and encouragement during my stay in Germany.

Last but not least, I am very grateful for the scholarship support from the China Scholarship Council.

Curriculum Vita

Personal Information

Name: Liu-Liu Shen

Place of birth: Shijiazhuang, Hebei, China

Nationality: Chinese

E-mail: shenliuliu1@gmail.com

Education Background

- 12/2015 – present, Ph.D. student, Department of Chemistry, Technische Universität Darmstadt, Germany
  Thesis: Paper-based microfluidics for electrochemical applications
  Advisor: Prof. Dr. Bastian. J. M. Etzold

- 09/2012 – 07/2015, M. S. Department of Chemistry, Tsinghua University, China
  Thesis: Design and synthesis of platinum-based nanostructures and their electrocatalytic properties
  Advisor: Prof. Bo-Qing Xu

- 09/2008 – 06/2012, B. S. Department of Chemistry and Chemical Engineering, Shandong University, China
  Thesis: Synthesis of nanoporous gold-based catalysts for gas-phase oxidation of alcohols
  Advisor: Prof. Xiaohong Xu